Exploring Metal Nitride Synthesis

From Precursors to Structural Insights

Inauguraldissertation

zur

Erlangung der Würde eines Doktors der Philosophie

vorgelegt der

Philosophisch-Naturwissenschaftlichen Fakultät

der Universität Basel

von

Mahsa Parvizian

2024

Genehmigt von der Philosophisch-Naturwissenschaftlichen Fakultät

auf Antrag von

Erstbetreuer	Prof. Dr. Jonathan De Roo
Zweitbetreuer	Prof. Dr. Thomas R. Ward
Externer Experte	Prof. Dr. Maksym Yarema

Basel, den 14.11.2023

Dekan Philosophisch-Naturwissenschaftliche Fakultät

Prof. Dr. Marcel Mayor

To my better half,

who has walked every step of this journey with me.

Acknowledgment

I would like to express my heartfelt thanks to Professor Jonathan De Roo for giving me the opportunity to embark on this transformative journey of pursuing my PhD. This remarkable experience has not only enriched my scientific knowledge but has also profoundly shaped me as an individual. Our discussions have been invaluable, and I am genuinely grateful for the wisdom and insights I've gained from them. I am equally appreciative of Professor Ward for his support as my second supervisor and Professor Yarema for graciously accepting the role of my external advisor.

Undertaking a high-risk, high-reward project often led to days when everything seemed unclear. I couldn't have reached this point without the incredible support of the members of the De Roo group. I would like to begin by expressing my gratitude to Dietger and Loren for guiding me at the beginning of this journey. A big shoutout to Ale, for being the absolute best in our journey together. Rohan, one day I promise to give your Instagram posts the recognition they deserve. Nico, if you're reading this, congratulations on your new desk! Carlotta, thank you for being the reliable anchor that everyone could turn to. Ajmal, if one day chemistry loses its appeal, you'd make an outstanding travel influencer. Jibin and Jikson, your lifesaving heroics during our group trip are eternally appreciated. Liza, you're welcome for my role in saving your life during the same adventurous trip – what an unforgettable experience! Evelina, my fume hood neighbor, I only wish you had joined our journey sooner. Evert, thank you for enlightening me about the world of wine, even though I don't drink. Eline, your Secret Santa surprises were the absolute best. Chris, thanks for being my partner in nitride-crime. Ramòn, our coffee breaks were a source of both caffeine and camaraderie. I'm grateful to the students I had the chance to meet at the De Roo lab — Philippe, Antonia, Jin, Alina, Anna, Nadya, and Mohit. Thank you for your curiosity and fruitful discussions.

To all the members of the Seebeck group, your kindness throughout my journey has left a lasting impression. To all the chemistry football team and PCC board members, thank you for the enjoyable and memorable events we've shared. Alex, your consistent assistance in fixing the XRD has been a tremendous help, and Isa, your adventurous biking trips have always been a source of inspiration. My genuine thanks to each one of you, including those I may have unintentionally left out, for making this journey truly unforgettable, both professionally and personally. I would like to sincerely thank ChatGPT and Grammarly for proofreading my thesis so carefully.

Thanks, Mom and Dad, for all the things you've done so I could be here today. You've always had my back and believed in me. To my late grandma, who worried about my exams even more than I did – this is the last degree I'm going for. Eli and Mohammad, congratulations on your new addition! Your support has meant the world to me, and I miss you dearly.

To my parents-in-law and Moudi, thank you for your constant love and emotional support.

And finally, to Hamed, you've been my rock throughout this journey. I couldn't have done it without you. You've been my rocket fuel, propelling me to reach for the stars!

Abstract

Metal nitride nanocrystals are a versatile class of nanomaterials with a wide range of optical properties, depending on their chemical composition. These properties can vary from those typical of traditional semiconductor nanocrystals, often referred to as quantum dots, to more metallic character, featuring plasmon resonance. However, the synthesis of colloidal metal nitride nanocrystals presents unique challenges due to the less developed precursor chemistry compared to other nanocrystal systems, such as metal, metal chalcogenide, or metal phosphide nanocrystals.

This thesis begins with a comprehensive literature review of current synthetic methods for producing metal nitride nanocrystals, with a primary focus on chemical conversion reactions, laying the foundation for our research. Our investigation focuses on copper nitride (Cu_3N), a well-studied metal nitride synthesized via wet chemistry. We explore the precursor conversion process and the complexities of surface chemistry associated with Cu_3N. Building upon the insights gained from Cu_3N chemistry, we investigate various wet chemical approaches aimed at developing methodologies for producing colloidally stable metal nitrides at relatively low temperatures.

Recognizing that some nitride formations require higher temperatures to achieve crystalline materials, we delve into the realm of solid-state chemistry. Our work provides an in-depth examination of solid-state-based synthesis methods, particularly focusing on titanium nitride metal nitrides.

Finally, we turn our attention to the surface chemistry for nanocrystals, with a specific focus on the use of silane as a versatile ligand. Throughout this thesis, we aim to comprehensively cover synthetic strategies, chemical complexities, and surface chemistry aspects associated with metal nitride nanocrystals. The insights provided in this work are intended to serve as a valuable guide for the further development and applications of colloidal nitride nanocrystals in various fields of nanoscience and technology.

Contents

Acronyms

mpg-C_3N_4	mesoporous graphitic carbon nitride.
*p*XRD	x-ray powder diffraction.
BE	binding energy.
COSY	homonuclear correlation spectroscopy.
CVD	chemical vapour deposition.
DFT	density functional theory.
DLS	dynamic light scattering.
DOSY	diffusion ordered spectroscopy.
E_F	Fermi energy.
FT-IR	fourier-transform infrared spectroscopy.
GC-MS	gas chromatography–mass spectrometry.
HAADF-STEM	high-angle annular dark-field scanning transmission electron microscopy.
HMS	hexadecyltrimethoxysilane.
HMT	hexamethylenetetraamine.
HR-TEM	high-resolution transmission electron microscopy.

LSPR	localized surface plasmon resonance.
MS	hexadecyilmono-methoxy silane.
NCs	nanocrystals.
NMR	nuclear magnetic resonance.
NOESY	nuclear overhauser effect spectroscopy.
NPs	nanoparticles.
OA	oleic acid.
ODA	octadecylamine.
ODE	1-octadecene.
OER	oxygen evolution reaction.
OLAm	oleylamine.
ORR	oxygen reduction reaction.
PDF	x-ray total scattering and pair distribution function analysis.
PL	photoluminescence spectroscopy.
PPC	pyrrole-*2*-carbaldpropyliminato copper(II).
QDs	quantum dots.
SEM	scanning electron microscope.
SLS	solution-liquid-solid.
TEM	transmission electron microscopy.
TGA	thermogravimetric analysis.

TMAH	tetramethylammonium hydroxide.
TMS amine	tris(trimethylsilyl)amine.
TOP	tri-*n*-octylphosphine.
TOPO	trioctylphosphine oxide.
VBM	valence band maximum.
XPS	x-ray photoelectron spectroscopy.

The path less traveled may be fraught with challenges, but it's also where the most exceptional discoveries are made.

Anonymous

1 Introduction

1.1 Preface

Various nanomaterials show size-dependent properties, *e.g.*, magnetic, electrical, and optical properties that cannot be achieved in the bulk material. Therefore, the synthesis of uniform nanocrystals (NCs) with controlled size and shape has been attracting a lot of attention.[1] While atomic precision is still more an aspiration than a reality in NCs science,[2] it is imperative to produce colloids with narrow size distributions (low polydispersity) to allow the study of size dependent properties.[3] Ligand-assisted, wet chemical synthesis has provided the necessary control over NCs size and shape.[4] However, it is a complex process, combining metal-organic chemistry, inorganic crystallization, and surface chemistry to yield an organic/inorganic hybrid object that is colloidally stable. The precursor conversion mechanism of many metals, metal chalcogenide, metal phosphide, and metal halide NCs has been elucidated,[5–8] and their surface chemistry increasingly better understood.[9–15] The crystallization mechanism,*i.e.,* nucleation and growth, causes more discussion in the literature[16;17] as the approaches based on classical nucleation theory are at odds with the Finke-Watzky based mechanisms.[18;19]

Recent evidence shows that many NCs do not nucleate via a burst nucleation event,

[‡]**Adapted from**: Parvizian, M.; De Roo, J.; Precursor chemistry of metal nitride nanocrystals; *Nanoscale*, **2021**, 13, 18865-18882

but rather that nucleation is a continuous process.[20–22] Continuous nucleation does not necessarily lead to polydisperse ensembles because small NCs grow faster than larger NCs, allowing the newly formed NCs to catch up with the growing NCs population.[21–24] Even without a comprehensive framework for NC crystallization, chemists have been able to adjust the final NCs size by controlling the precursor conversion rate.[25] The three aspects of colloidal synthesis (precursor conversion, crystallization, and surface chemistry) are interdependent. An additional, often neglected parameter is the solvent. During high temperature NC synthesis, certain popular solvents, such as 1-octadecene (ODE) and trioctylphosphine oxide (TOPO), decompose or polymerize, forming products that compromise the purity of the final NCs.[26;27] Moreover, the purity of the ligand can considerably influence the solubility of the starting precursors and provide a better capping of the final NCs. For instance, oleylamine (OLAm) stands out as one of the most commonly employed ligands, demonstrating significantly improved encapsulation properties when subjected to purification.[28]

While metal, metal chalcogenide, and metal halide NCs are well studied, the metal pnictides have received less attention, with the exception of metal phosphides.[8;29–32]Metal nitrides in particular are a versatile class of nanomaterials but their synthesis is not well developed. One difficulty is the higher thermodynamic stability of the oxides, compared to the nitrides, see Table 1.1. One can rationalize the lower standard formation free energy for nitrides because of the high bond enthalpy of molecular nitrogen (941 kJ mol^{-1}) versus oxygen (500 kJ mol^{-1}).[33;34] Another factor is the lower ionic character of metal nitrides since the enthalpy of formation of N^{3-} is much higher than for O^{2-} (2300 kJ mol^{-1} versus 700 kJ mol^{-1}).[35] Only AlN and alkali(ne earth) metal nitrides are regarded as saline nitrides and they react rapidly with water, releasing ammonia.[36] On the other hand, boron and silicon nitride are almost purely covalent compounds with high stability.[36] Transition metals like titanium form interstitial nitrides with extremely high chemical, thermal, and mechanical stability.[36] Given the above considerations, it is no surprise that metal nitride synthesis is generally carried out at a high temperature and with nitrogen-containing reagents more reactive than molecular nitrogen.

Table 1.1 Standard Gibbs free energies of formation (kJ/mol) for selected oxides and nitrides at room temperature.[37]

Oxides	ΔG_f°	**Nitrides**	ΔG_f°
TiO_2	−891.2	TiN	−309.2
ZrO_2	−1042	ZrN	−336.8
MnO_2	−464.4	Mn_3N_2	−146.4
Fe_2O_3	−744.8	Fe_2N	+12.6
CoO	−213.8	Co_3N	+8.4
CuO	−128.4	Cu_3N	+74.5
ZnO_2	−318.4	Zn_3N_2	−20.9

This thesis embarks on a journey to enhance our understanding of the precursor conversion mechanism in previously reported metal nitrides, principally copper nitride NCs. Our goal is to apply this knowledge to create other metal nitrides like Ni_3N, Zn_3N_2, and TiN. Through meticulous exploration and experimentation, we aim to uncover the processes involved in their formation, paving the way for new possibilities in the realm of colloidal NCs synthesis.

1.2 Literature review

This section is predominantly concentrated on wet chemical synthesis techniques that yield NCs with strong colloidal stability. Other methods such as gas phase or physical approaches, are only included when informative. Here, alkali or alkaline earth nitrides NCs are not discussed as there are no synthetic procedures available and they are extremely sensitive towards moisture, rendering them less appealing from a technological standpoint. Our systematic exploration follows the periodic table, sequentially addressing nitrides within each group. The journey commences with group 4 and concludes with group 13.

1.2.1 Group 4 metal nitrides

Group 4 transition metal nitrides have a high melting point, high chemical stability, and excellent corrosion resistance. TiN, ZrN, and HfN have a cubic crystal structure (Fm-3m

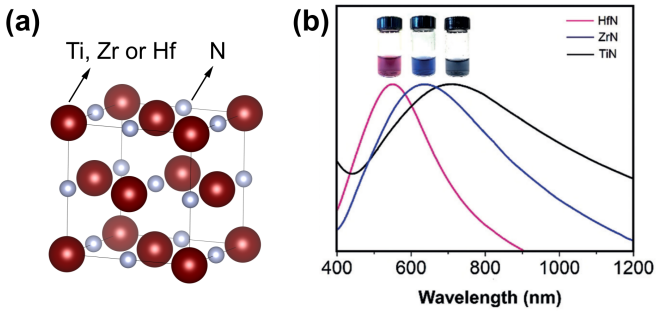

Figure 1.1 (a) Crystal structure of group 4 metal nitride. The metal is represented in purple and the nitrogen atom in grey. Structures plotted using VESTA.[46] Cif file obtained from ref.[47–49] (b) Absorption spectra of aqueous dispersions of TiN, ZrN, and HfN NCs. The inset shows a photograph of the NCs dispersed in water. Reprinted from ref[38] with permission from John Wiley and Sons, Copyright 2019.

space group) with a lattice constant of 4.239 Å, 4.585 Å, and 4.510 Å respectively, see Figure 1.1. Their structure is similar to their corresponding fcc metallic structure with interstitial nitrogen atoms in the octahedral holes. Group 4 metal nitride NCs exhibit a localized surface plasmon resonance (LSPR) in the visible region (HfN and ZrN) or the near infrared regime (TiN), see Figure 1.1.[38] The plasmonic response translates into a highly efficient conversion of sunlight into heat, an effect that has been used for water evaporation and desalination.[39–42] The position of the LSPR of TiN in the infrared region makes it suitable for photothermal therapies or plasmon-induced photocatalysis.[43] Given the optical properties of the group 4 metal nitrides, they are a sustainable alternative for gold NCs. Furthermore, they exhibit interesting catalytic properties. ZrN NCs possess excellent activity and long-term stability (superior to platinum) as catalysts for the electrochemical oxygen reduction reaction (ORR).[44] Also HfN NCs are catalytically active for the oxygen evolution reaction (OER).[45]

In 1988, TiN films were prepared using atomic layer epitaxy at 500 °C; where $TiCl_4$ precursor was pulsed into a reactor with gaseous ammonia.[50] The color depends on the stoichiometry of the film. For 40 % N, a golden yellow color is observed while for 50 %,

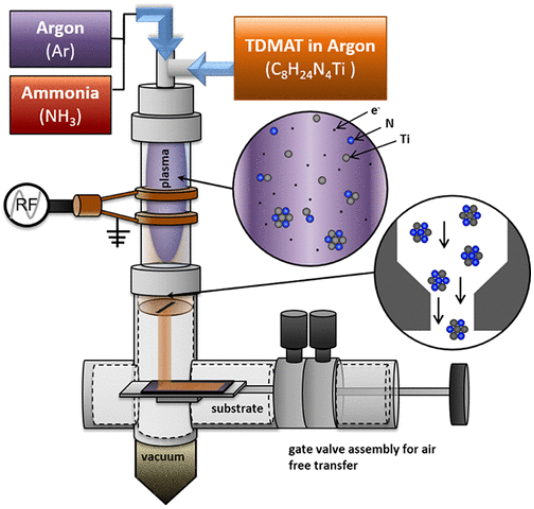

Figure 1.2 Diagram of the nonthermal plasma apparatus for TiN NCs synthesis. Reprinted with permission from[53]. Copyright 2018 American Chemical Society.

a dark violet is obtained. Alternatively, $Ti(NMe_2)_4$ is reacted with ammonia. Similar strategies apply to ZrN and HfN. An extensive account of customized precursors for chemical vapour deposition (CVD) of the group 4 nitrides is reviewed by Kafizas *et al.*[51]

Non-thermal plasma synthesis

In 2017, powders of TiN were synthesized in a non-thermal plasma reactor (Figure 1.2) from gaseous $TiCl_4$ and ammonia.[52]

$$6\ TiCl_4 + 8\ NH_3 \longrightarrow 6\ TiN + N_2 + 24\ HCl \tag{1.1}$$

The particle size is tuned from 3 to 8 nm by decreasing the flow rate of ammonia. The smaller particles are more oxidized than the bigger particles, but all show a plasmon resonance between 800 and 1000 nm. One can obtain ZrN NCs in a similar fashion using $ZrCl_4$ and NH_3 as the precursors.[54] After synthesis, the powders need to be heated at 200 °C in an Ar atmosphere to remove the ammonium salt

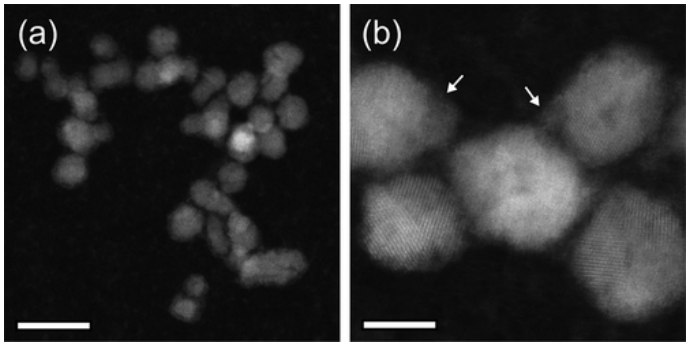

Figure 1.3 High-angle annular dark-field scanning transmission electron microscopy (HAADF-STEM) images of the obtained TiN NCs via non-thermal plasma synthesis . Scale bars are (a) 20 nm and (b) 5 nm. Reprinted with permission from.[53] Copyright 2018 American Chemical Society.

by-products. To avoid this last step, $TiCl_4$ was later replaced with titanium (IV) tetrakis(dimethylamido)($Ti(NMe_2)_4$).[53]

$$6\ Ti(NMe_2)_4 + 8\ NH_3 \longrightarrow 6\ TiN + N_2 + 24\ HNMe_2 \tag{1.2}$$

Also here, the particles are 6–8 nm in size (Figure 1.3) and have a well-defined plasmon resonance (around 800 nm). However, the particles are not monocrystalline (consisting of 2–3 nm crystallites) and contain a considerable amount of carbon.

Solution chemistry of titanium complexes

In solution, $TiCl_4$ reacts with *tert*-butylamine to the mixed chloro amido complex **1**, see Figure 1.4.[55] **1** has been used as a single source precursor for the CVD deposition of TiN. When **1** is reacted with triphenylphosphine oxide, **2** is formed (Figure 1.4), which does not convert to TiN during CVD. Complex **1** is unstable at room temperature and slowly loses *tert*-butylamine, probably forming an imido species. This is supported by the formation of the monomeric *tert*-butylimido complex **3** by the addition of *tert*-butylpyridine as neutral Lewis base (Figure 1.4).[56] Chapter 3 of this thesis delves into a more detailed discussion of additional instances where titanium complexes are employed

in solution-based chemistry to facilitate nitride formation.

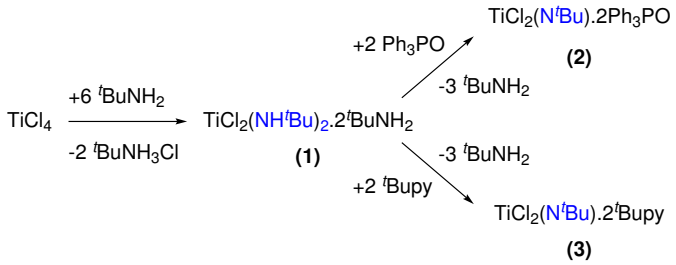

Figure 1.4 | Reactions of titanium chloride with *tert*-butylamine and triphenylphosphine oxide or *tert*-butylpyridine.

Nitride formation from the corresponding metal oxide

TiN NCs were obtained by Fischer *et al.* by using a mesoporous graphitic carbon nitride (*mpg*-C_3N_4) as both the confinement and nitrogen source.[57] In this strategy, amorphous TiO_2 (confined in the pores) is first prepared via a sol-gel procedure starting from $TiCl_4$ in ethanol. In a second step, this composite product is heated to 800 °C under an inert atmosphere or in sealed quartz ampoules. The confined metal oxide is transformed into pure TiN while the *mpg*-C_3N_4 is decomposed, see Figure 1.5. The size of the final TiN NCs can be slightly adjusted (5.6 nm to 7.1 nm) by controlling either the pores of the starting *mpg*-C_3N_4 or changing the concentration of the initial $TiCl_4$ precursor (filling rate). However, the resulting NCs are strongly aggregated.[57]

In 2007, Buha *et al.* investigated the thermal transformation of pre-synthesized anatase TiO_2 NCs into nanocrystalline TiN by using cyanamide or urea as a nitrogen source at 800 °C under nitrogen atmosphere.[58] Complete transformation is achieved when starting from 5 nm titania while with 10 and 20 nm titania, anatase impurities are still present. This reflects the solid state nature of the approach. When using a high excess of cyanamide or urea, a large amount of amorphous carbon is also produced (20–25 wt%). This can be minimized to 2 wt% by reducing the cyanamide or urea amount. The resulting TiN NCs have an average crystallite size of 3 nm and are aggregated to 50 nm agglomerates, embedded in amorphous carbon. Similarly, ZrN NCs were synthesized by

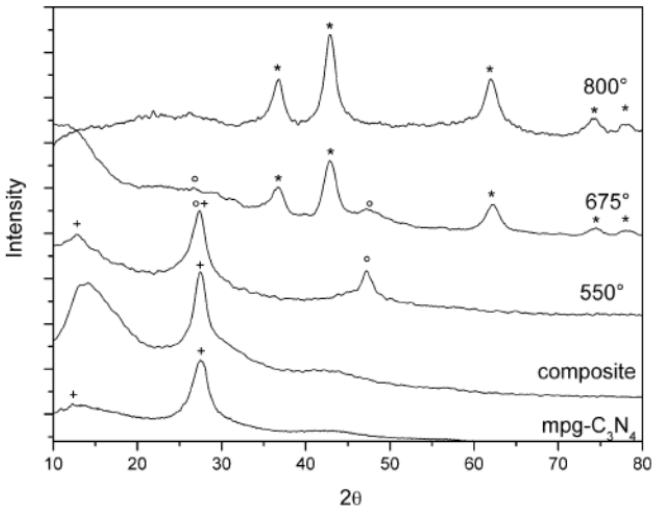

Figure 1.5 Temperature-dependent x-ray powder diffraction (*p*XRD) analysis of the TiO_2 precursor/*mpg*-C_3N_4 composites. (+) represents *mpg*-C_3N_4; (o), TiO_2; and (*), TiN. Reprinted from ref[57] with permission from John Wiley and Sons, Copyright 2007.

reacting 10–15 nm ZrO_2 NCs with urea at 1100 °C under an ammonia flow.[59] In 2009, Giordano *et al.* introduced the *urea glass route*, a method involving sol-gel chemistry and the above strategy of Buha, resulting in the formation of metal nitrides like TiN, with the optimal urea-to-titanium ratio being four and required temperatures as high as 800 °C for complete crystallization. This approach was extended to various other metal nitrides including VN, NbN, GaN, CrN, Mo_2N and nanocomposites such as *mpg*-C_3N_4 doped with TiN.[60–62]

In Chapter 4 of this thesis, an in-depth exploration is conducted to discuss further instances wherein group 4 metal nitrides are synthesized through solid-state reactions, starting from their respective metal oxide precursors.

1.2.2 Group 5 metal nitrides

Group 5 metal nitrides (vanadium, niobium, and tantalum nitrides) have the same crystal structure as group 4 metal nitrides a cubic crystal structure with a Fm-3m space group

with a lattice constant of 4.13 Å,[63] 4.394 Å,[47] and 4.331 Å[64] respectively. These group 5 nitrides exist as well in other oxidation states with less common crystal structures (orthorhombic, tetragonal, and hexagonal), *e.g.,* Ta_3N_5, Ta_4N_5 or Ta_5N_6. Vanadium nitride (VN) has attracted interest as an active material for supercapacitors due to its high specific capacitance as well as high electrical conductivity.[65] Niobium nitrides (Nb_2N, Nb_4N_3, NbN, etc.) are mainly investigated as superconductors. Furthermore, nitrogen-rich niobium nitrides are good candidates for electrochemical capacitors.[66;67]

VN and NbN nanopowders were synthesized via the urea glass route, see above.[60] Agglomerated VN NCs with a crystallite size of 6 nm have been synthesized by Choi *et al.* via a two-step method. First, ammonolysis of VCl_4 forms amorphous $V(NH_2)_3Cl$. Second, the amorphous precursor is crystallized at 400 °C in the presence of NH_4Cl under an ammonia atmosphere.[68] This method is one of the main chemical methods to form VN NCs,[69] as well as NbN NCs.[70]

In 1972, Ta_3N_5 powder and thin films were obtained at 800 °C starting from ammonia and Ta_2O_5 powder or Ta thin films respectively.[71] This strategy was recently pursued to prepare Ta_3N_5 nanotubes.[72] In 1995, TaN films were made using the CVD method with tris(diethylamido)(*tert*-butylimido)tantalum(V) as precursor at temperatures ranging from 450 to 650 °C.[73] Nanocrystalline TaN with a cubic phase has been synthesized via a solid combustion synthesis using K_2TaF_7, NaN_3, and NH_4F precursors under high temperatures up to 850 to 950 °C.[74]

In 2011, Ho *et al.* reported three methods for the synthesis of colloidal Ta_3N_5 NCs.[75] In their first method $TaCl_5$ is dispersed in ODE. At 310 °C, tris(trimethylsilyl)amine ($(TMS)_3N$), dissolved in tri-*n*-octylphosphine (TOP) is injected and the particles are left to crystallize for 20 min at 300 °C.

$$TaCl_5 + R_3P + (TMS)_3N \xrightarrow[ODE]{\text{300-310°C}} Ta_3N_5 \tag{1.3}$$

The resulting NCs (23 nm, see Figure 1.6 (a)) could not be redispersed in any solvent after precipitation due to a lack of strongly binding ligands. Smaller (10 nm) NCs were

formed at a reaction temperature of 200 °C. The authors report that the synthesis is sensitive to the purity of $TaCl_5$; at least 99.99% purity is required, and even then the yield was very low (which was attributed to the low solubility of $TaCl_5$ in ODE). In their second method, tantalum (V) chloride was dissolved in a mixture of OLAm and TOPO. Li_3N was added at 300 °C.

$$TaCl_5 + Li_3N \xrightarrow[\text{TOPO, OLAm}]{300\,^\circ\text{C}} Ta_3N_5 \tag{1.4}$$

The resulting NCs (2–8 nm after 20 min reaction, see Figure 1.6 (c)) could be redispersed in hexane after precipitation with methanol. When the reaction is left to proceed for 1 h, 10 nm NCs are obtained. Their absorption spectrum has two absorption onsets (467 nm and 515 nm) which is explained by the absorption of Ta_3N_5 (515 nm) and that of a higher bandgap material, likely an oxidized shell. X-ray photoelectron spectroscopy (XPS) data indeed confirm the presence of oxidic tantalum. To counter the low yields in the previous methods, the authors devised a third method. Pentakis(dimethylamino)tantalum (V) and $(TMS)_3N$ were dissolved in ODE and injected in pure ODE at 300 °C (Figure 1.6 (b)). However, the formed particles were amorphous and highly sensitive to air.[75] For all three methods, the crystallinity of the resulting particles was solely assessed by transmission electron microscopy (TEM) and an ensemble measurement, e.g., *p*XRD, is missing.

$$Ta(NMe_2)_5 + (TMS)_3N \xrightarrow[\text{ODE}]{300\,^\circ\text{C}} TaN_x \tag{1.5}$$

In 2013, a sol-gel pathway was demonstrated with $Ta(NMe_2)_5$ and *n*-propylamine.[76] Transamination occurs readily but the condensation appears to be slower than for titanium, see section on titanium nitride for details on transamination and condensation. Upon solvent evaporation, a gel was formed. Solvent removal by vacuum resulted in a xerogel that converted in an ammonia atmosphere at 800 °C into Ta_3N_5 powder with a crystal size of 20 nm. Thin films were obtained by coating the silica slides with the

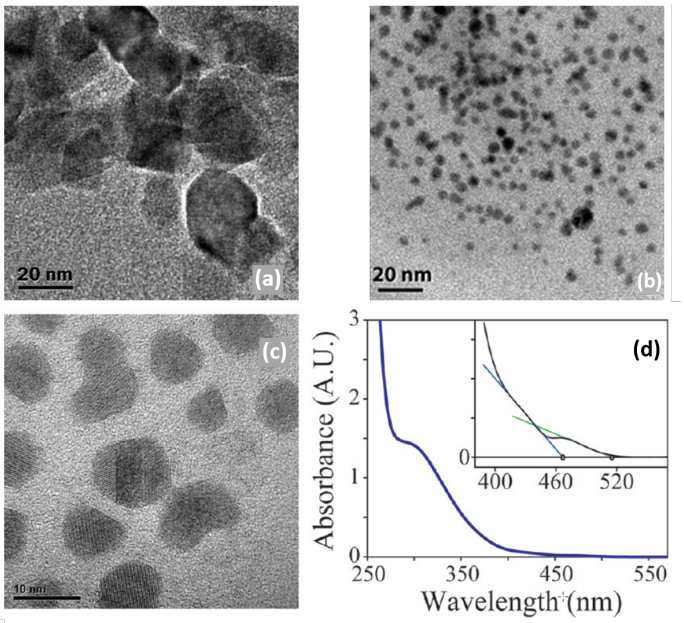

Figure 1.6 TEM images of Ta_3N_5 obtained by Ho *et al.*[75] (a) NPs obtained with $TaCl_5$ and $(TMS)_3N$ (scale 20 nm), (b) with $Ta(NMe_2)_5$ and $(TMS)_3N$ (scale 20 nm) (c) with $TaCl_5$ and Li_3N (scale 10 nm). (d) Absorption spectrum of the obtained 10 nm Ta_3N_5. The inset shows the two limiting regimes. Adapted with permission from reference.[75] Copyright 2010 American Chemical Society.

sol. Annealing at 600 °C leads to TaN while heating to 800 °C yields Ta_3N_5.[76] It is thus clear from the above that NCs of the group 5 nitrides have not been convincingly obtained in colloidal form. While this is the first challenge for the future, the second challenge is to control the oxidation state and the polymorphism of these materials.

1.2.3 Nickel(I) nitride

Nickel(I) nitride (Ni_3N) has a hexagonal epsilon-Fe_3N-type structure with a P6(3)22 space group, see Figure 1.7. The two lattice constants are 4.622 Å and 4.305 Å.[77] Ni_3N is interesting for various applications such as lithium-ion batteries,[78] magnetic NCs,[79;80] catalysis and electrocatalysis,[81;82] including hydrogenation, hydrogen, and OER.[83;84] The early chemical synthetic methods to obtain Ni_3N were based on nickel complexes

decomposition at high temperatures and in the presence of ammonia or hydrazine.[78;80] Up to this point, a lack of literature exists in the examination of solution-based synthesis techniques that yield phase-pure Ni_3N. The few existing studies are discussed in detail in Chapter 3 to establish a more robust connection with our attempts to synthesize Ni_3N.

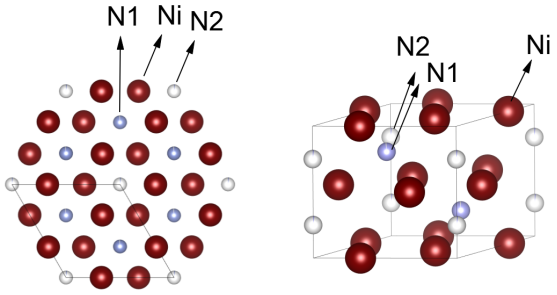

Figure 1.7 Crystal structure of Ni_3N. The nickel atoms are represented in dark red and the nitrogen atoms in cyan and white. Structures plotted using VESTA.[46] Cif file obtained from Ref.[77]

1.2.4 Copper(I) nitride

Copper(I) nitride (Cu_3N) adopts an anti-ReO_3 crystal structure within the P$m3m$ space group, featuring a lattice constant of 3.817 Å, as illustrated in Figure 1.8.[85;86] As a semiconductor with a band-gap of 1.7 eV, Cu_3N holds promise for applications in solar cells.[87] Its thin films have found utility in optical storage devices[88] and resistive random access memory chips.[89] Furthermore, Cu_3N NCs have demonstrated catalytic activity in the reduction of CO_2 to ethylene,[90] alkaline water electrolysis,[91] and ORR.[92] By doping Cu_3N with metals such as Pd, Cu_3Pd_xN (with $0.02 < x < 1$) a more metallic behavior can be obtained.[93–95] The crystal structure of the latter closely resembles that of Cu_3N, featuring a palladium atom at the center of the unit cell, as depicted in Figure 1.8. It is noteworthy that Cu_3N forms at relatively low temperatures but decomposes into metallic copper at higher temperatures. Specifically, under an inert atmosphere, Cu_3N films decompose at 475 °C.[88] When subjected to heating in air, Cu_3N decomposes into CuO.[96]

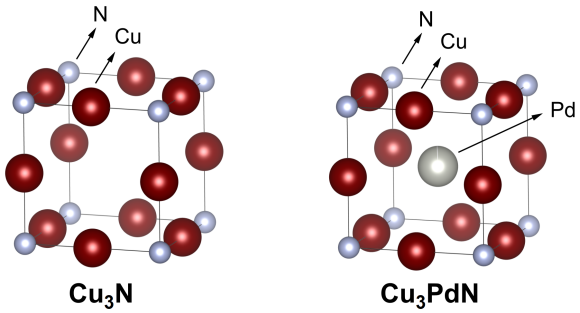

Figure 1.8 Crystal structure of Cu_3N and the doped Cu_3PdN. The copper is represented in dark red, the palladium in grey, and the nitrogen atom in cyan. Structures plotted using VESTA.[46] Cif file obtained from Ref.[97;98]

In 1939, Juza *et al.* synthesized Cu_3N powders by reacting CuF_2 with ammonia gas (ammonolyis reaction).[99] Phase pure Cu_3N was obtained at reaction temperatures between 250–325 °C (after 6 h reaction time).[100] At higher temperatures, Cu(0) is formed. Alternatively, Zachweija and Jacobs synthesized Cu_3N by thermal decomposition of $[Cu(NH_3)_x](NO_3)$.[97] In 2005, Choi *et al.* combined copper(II) chloride and sodium azide in superheated toluene or THF.[96] The intermediate copper(II) azide decomposes to Cu_3N powder at 185 °C.

$$CuCl_2 + 2\ NaN_3 \xrightarrow[\text{THF or toluene}]{<120\,^\circ\text{C}} Cu(N_3)_2 + 2\ NaCl \tag{1.6}$$

$$2\ Cu(N_3)_2 \xrightarrow[\text{THF or toluene}]{185\,^\circ\text{C}} 2\ Cu_3N + 11\ N_2$$

The low reaction temperature is remarkably lower than previously reported for the similar synthesis of other metal nitrides such as TiN and GaN. Unfortunately, the reaction time is very long (about three days) and metal azides are thermally unstable and shock sensitive, which limits the reaction to small scales. Finally, the obtained Cu_3N is not phase-pure and some NaCl impurities remain present in the sample. The solution-based synthesis of Cu_3N using $Cu(NO_3)_2$ as the precursor has been extensively researched, with various synthesis variations being documented. This pathway is perhaps the most widely explored method for forming metal nitrides. As a result, this section comprises

an independent chapter (Chapter 2), wherein we conduct a thorough investigation into these synthesis approaches. Below, summarized as a solution-based or sol-gel route, are the alternative synthesis methods that have been reported for Cu_3N.

Solution-Based Synthesis Routes

Deshmukh *et al.* reacted $Cu(OMe)_2$ in benzylamine ($BnNH_2$) and obtained very small, spherical Cu_3N NCs (2.2 ± 0.5 nm).[101;102]

$$Cu(OMe)_2 + 117\ BnNH_2 \xrightarrow[15\ min]{140\,^\circ C} Cu_3N \tag{1.7}$$

The standard synthesis is performed at 140 °C, under an inert atmosphere, in a pressure tube. Throughout the reaction, the color changes from dark blue to red. The average crystal size (determined from *p*XRD) is quite insensitive to the reaction conditions (80–180 °C, 5–60 min) and varies from 1.8 to 2.8 nm. The authors further suggested a precursor conversion mechanism by analyzing the reaction by-products with gas chromatography–mass spectrometry (GC-MS), see Figure 1.9. In the first step, copper(II) methoxide oxidizes benzylamine to benzenemethanimine and is reduced to copper(I). This proposal is based on the detection of methanol in GC-MS. This reactivity is special for $Cu(OMe)_2$ since other Cu(II) salts, such as $CuCl_2$, make stable complexes with amines and fail to produce Cu_3N. The benzenemethanimine intermediate reacts with benzylamine, yielding *N*-benzylidenebenzylamine (detected by GC-MS) and ammonia. The *in-situ* formed ammonia reacts with Cu(OMe) to form Cu_3N. Traces of benzonitrile are also observed at the GC-MS, which is justified by further oxidation of benzenemethanimine in the presence of Cu(II). This synthetic strategy was adopted by Liu *et al.*.[103]

In 2018, Mondal and co-workers obtained Cu_3N by reacting hexamethylenetetraamine (HMT) and $Cu(NO_3)_2.5H_2O$ in *n*-hexanol at 200 °C for one hour under an inert atmosphere.[104] HMT undergoes hydrolysis and forms formaldehyde and NH_3. The latter is the source of nitrogen as described in Figure 1.10. Copper (II) nitrate is in this case

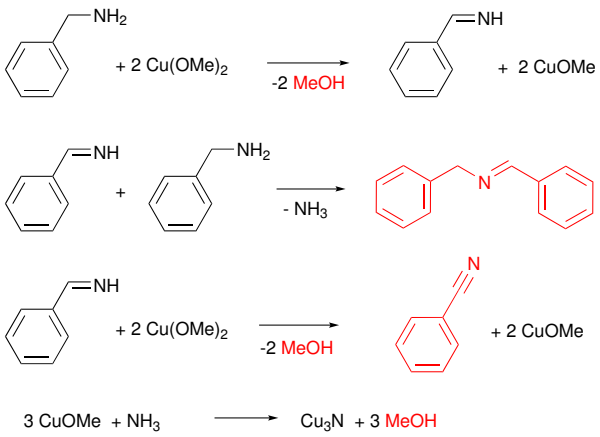

Figure 1.9 | Proposed reaction mechanism of $Cu(OMe)_2$ with $BnNH_2$ that leads to the formation of Cu_3N.[101] Molecules in red are the one detected by GC-MS.

simply the source of water and copper and not the nitrogen source. Cu(II) is assumed to be reduced by the formaldehyde intermediate, but the authors do not show evidence for the formation of formic acid. The final NCs are around 80 nm in size, which is most likely due to the absence of a strongly coordinating ligand.

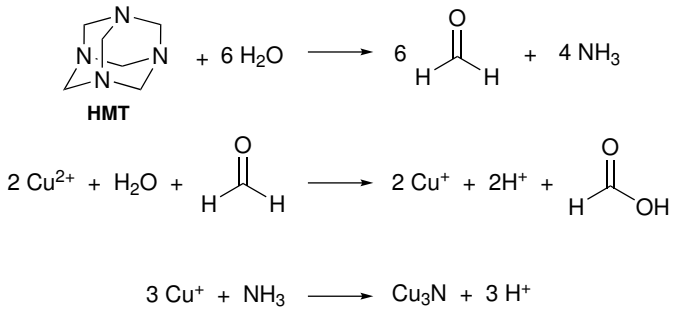

Figure 1.10 | Proposed reaction mechanism for Cu_3N formation from hexamethylenetetraamine and $Cu(NO_3)_2.5H_2O$.[104]

Also in 2018, Sithole *et al.* synthesized a novel copper precursor: pyrrole-*2*-carbaldpropyliminato copper(II) (PPC), see Figure 1.11.[105] PPC is synthesized from pyrrole-*2*-carboxaldehyde, copper(II) acetate and propylamine in deionized water, filtered and recrystallized. In the second step, PPC is heated with octadecylamine (ODA) to form Cu_3N (Figure 1.11). The resulting spherical NCs are about 1.5 to 4 nm in

diameter, in contrast to the 18 nm cubes that are obtained with copper(II) nitrate under identical conditions. The photoluminescence of the smaller Cu_3N NCs is slightly blue-shifted to the emission of the larger NCs, which could be ascribed to quantum confinement. Indeed, we estimated from the calculated dielectric constant and the effective hole and electron masses, an exciton Bohr radius of about 3 nm. However, a direct relation between size and optical properties is currently missing.

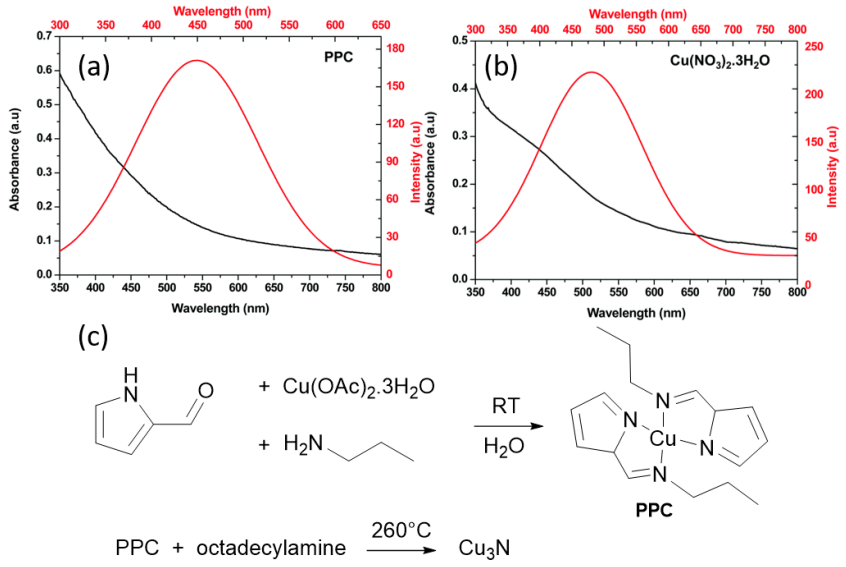

Figure 1.11 UV-Vis absorption and photoluminescence spectra of Cu_3N obtained via (a) PPC and (b) $Cu(NO_3)_2 \cdot 3\,H_2O$ method. (c) Reaction mechanism proposed for Cu_3N formation from the reaction of PPC and ODA shown below. Adapted from reference[105] with permission from the Royal Society of Chemistry.

Sol-Gel chemistry

In aqueous sol-gel chemistry, dissolved metal precursors are hydrolyzed with water and further condense in metal oxide particles and gels.[106] Similarly, researchers have synthesized copper(II) nitride NCs by amminolysis (reaction with ammonia) and condensation. In 2018, Egeberg *et al.* reacted CuI with ammonia under basic conditions to form

$Cu(NH_2)$.[107]

$$CuI \xrightarrow[\text{pyridine, -35 °C}]{KNH_2/lq\text{-}NH_3} Cu(NH_2) \xrightarrow[\text{pyridine, 130 °C}]{NH_3\uparrow} Cu_3N \tag{1.8}$$

By condensation of the copper amide under reflux conditions, small copper(I) nitride NCs are obtained (4.2 ± 0.7 nm), see Figure 1.12. Only pyridine is observed at the surface of the NCs according to fourier-transform infrared spectroscopy (FT-IR) and elemental analysis, which could explain why these NCs are air and moisture sensitive.

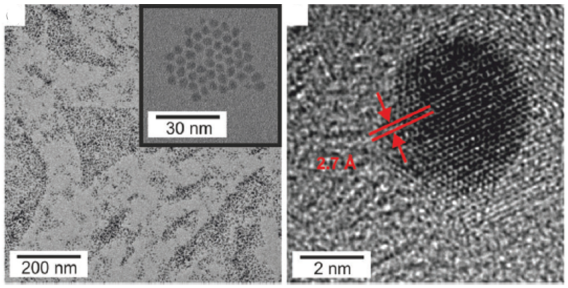

Figure 1.12 TEM images of Cu_3N NCs synthesized by sol-gel chemistry according to reference.[107] Reproduced from Ref.[107] with permission from the Royal Society of Chemistry.

Alternatively, Nakamura *et al.* have formed Cu_3N from copper(II) acetate in nonanol by bubbling ammonia through the mixture at 190 °C for 1 h.[108] The final NCs are not colloidally stable and form aggregates of about 200 nm with crystallite sizes of 20–30 nm. The same color changes are observed; from blue to yellow to dark brown. Single phase CuO is formed by using shorter chain alcohols such as pentanol, hexanol, and heptanol at 130 °C. With increasing temperature, an increasing amount of Cu_3N is obtained and from 170 °C, pure Cu_3N is formed. The authors propose the following mechanism. First, ammonia forms a complex with Cu(II), evidenced by a color change from green to blue. Second, the authors hypothesize Cu(II) is reduced by nonanol. The color change to yellow is consistent with a Cu(I) species but the authors do not detect the direct product, nonyl aldehyde. They do detect *9*-octadecenamide, of which it is unclear how it is exactly formed. Finally, the Cu(I) species reacts with ammonia to form Cu_3N. In the background, there is also the esterification of acetate with nonanol to nonyl acetate.

According to the mechanism, a lot of protons are released but the authors did not try to uncover the fate of these protons. Nor were alternative hypotheses considered such as the reduction of Cu(II) by ammonia itself.

1.2.5 Zinc(II) nitride

Zinc(II) nitride (Zn_3N_2) has a cubic crystal structure (Ia-3 space group) with a lattice constant of 9.7691 Å (Figure 1.13).[109] It is a nontoxic, earth-abundant, and low-cost semiconductor,[110] and is therefore promising for various applications. However, it has been less exploited than other nitrides due to the difficulties in preparation and its high reactivity towards water.[111] As a II-V group semiconductor, Zn_3N_2 has a high electron mobility and carrier concentration. The reported band gap for Zn_3N_2 varies from 1.0 to 3.3 eV depending on the preparation methods.[112–114] Various physical methods or nitridation approaches have been employed to synthesize Zn_3N_2 as thin films,[115] powders,[116] hollow balls,[117] or nanowires.[113] Much like Ni_3N, there are only a few chemical synthesis approaches that have been documented in the literature. These are discussed in Chapter 3 to establish a stronger correlation with our approaches for synthesizing Zn_3N_2 particles.

1.2.6 Group 13 nitrides

Among the group 13 nitrides, gallium(III) nitride has acquired the most fame due to its use in blue LEDs, a feat that has been awarded the 2014 Nobel Prize in Physics.[119] The most stable phase of the group 13 nitrides has the wurtzite crystal structure. The bandgap of AlN, GaN, and InN is 6.2 eV, 3.4 eV, and 0.7 eV respectively. As discussed before aluminum(III) nitride (AlN) is the least interesting nitride of group 13 since it is considered a saline nitride and rapidly reacts with water. However, AlN has high thermal conductivity (up to 320 W/mK), high acoustic wave velocity, and electrical resistance.[120] These properties raise the potential of AlN for applications such as thermal interfaces for electronic laser, brackets for LED technology, resonators, sensors, actuators, etc.[121–123] The different synthetic approaches for cubic AlN formation have been presented by

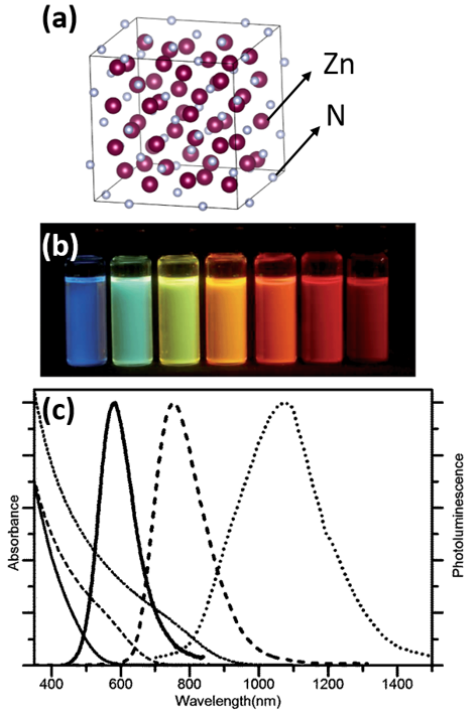

Figure 1.13 (a) Crystal structure of Zn_3N_2. The zinc cation is represented in purple and the nitrogen atom in grey. Structures plotted using VESTA.[46] Cif file obtained from Ref.[109] (b) Toluene solutions of OLAm capped Zn_3N_2 NCs sampled at different reaction times and excited with a 365 nm lamp. (c) Absorption (thin lines) and emission (thick lines) spectra of Zn_3N_2 NCs with mean diameters of 2.1 ± 0.4 nm (solid lines), 4.6 ± 2.3 nm (dashed lines) and 7.1 ± 2.0 nm (dotted lines). Reproduced from Ref.[118] with permission from the Royal Society of Chemistry.

Kudyakova *et al.*.[124]

Indium(III) and gallium(III) nitride (InN, GaN) NCs are considered the possible next generation of QDs. While the exciton Bohr radius of GaN is 3.2 nm, the exciton Bohr radius of InN is 8 nm. Together with the formation of solid solutions ($In_xGa_{1-x}N$), this provides ample opportunity to tune the optical properties using either quantum confinement or compositional control. GaN is also known as a bulk semiconductor suitable for applications in optoelectronics such as blue light emitting diodes. GaN is also being

investigated for high frequency and high power transistor design.[125;126] InN is a promising compound for optoelectronic applications due to its low bandgap, small effective mass, and efficient electron transport. InN is also considered for low-cost, high-efficiency solar cells, photomasks, laser diodes, sensors, and biological imaging.[127–131] InN NCs have complex plasmonic behavior due to a nonparabolic dispersion of its conduction band.[132;133]

Synthesis of group 13 nitride powders

In 2004, InN was prepared by the conversion of In_2O_3 under ammonia flow in a temperature range of 600 to 730 °C. Depending on the temperature, either spherical NCs or hollow microtubes are formed. This is due to the decomposition of InN at a temperature around 650 °C into metallic In and nitrogen.[134]

$$In_2O_3 + 2\,NH_3 \longrightarrow 2\,InN + 3\,H_2O$$

$$2\,InN \xrightarrow{650\,^\circ C} 2\,In + N_2$$

GaN NCs in a silica matrix were synthesized by first forming an oxide gel of gallium and silicon. The gel is then annealed at 900 °C for 5 h under NH_3 atmosphere.[135] Variations on this strategy exist where pure GaN nanocrystalline powders are formed by annealing Ga_2O_3, GaO(OH), or $NH_4[Ga(OH)_2CO_3]$ under an NH_3 atmosphere at 900–950 °C.[136–139] Similar to the case of TiN, the solid state reaction between Ga_2O_3 (or γ-Al_2O_3) and cyanamide CN_2H_2 yields GaN (or AlN) NCs.[58;140] Finally, the urea glass route was also successful in synthesizing GaN nanopowders.

Synthesis strategies based on azide or amide precursors

Colloidally stable, but poorly crystalline GaN NCs are obtained by refluxing $[Et_2Ga(N_3)]_3$, $(N_3)_2Ga[(CH_2)_3NMe_2]$, or $(Et_3N)Ga(N_3)_3$ in triglyme at 220 °C for 5 h.[141] Also, $GaCl_3$ and NaN_3 react to form gallium azide, which forms amorphous GaN at 220 °C or 260 °C in THF or toluene respectively. Annealing and NaCl removal

are necessary to form crystalline powders.[142] Finally, crystalline GaN NCs were formed from NaN_3 and metal Ga by heating to 700 °C under nitrogen in a high-pressure apparatus.[143]

Janik *et al.* formed GaN NCs via pyrolysis at 450–500 °C of a gallium imide $[Ga(NH)_{3/2}]_n$ precursor (obtained by reaction of $[Ga(NMe_2)_3]_2$ and NH_3).[144] In 1999, this method was improved by crystallizing the $[Ga(NH)_{3/2}]_n$ precursor in hot tri-*n*-octylamine (360 °C for 24 h) under a flow of ammonia.[145] During cooldown of the reaction mixture, a solution of hexadecylamine in tri-*n*-octylamine was added, which improved the colloidal stability of the final GaN NCs. These NCs have a diameter of 3 nm and feature a first excitonic emission at 3.65 eV, higher than the bulk bandgap of GaN. β-GaN NCs of 3–8 nm in size were obtained via microwave heating of $Ga(NH_2)_3$ in ionic liquid at 300 °C for 1 h. The colorless suspension of $Ga(NH_2)_3$ was obtained by dissolving $GaCl_3$ in liquid NH_3 at -35 °C and adding of KNH_2. The obtained NCs show a bandgap around 3.9 eV which is 0.6 eV above the β-GaN bulk bandgap. The authors attributed this blue shift to quantum confinement. The fluorescence properties of the as-synthesized NCs are shown in Figure 1.14.[146]

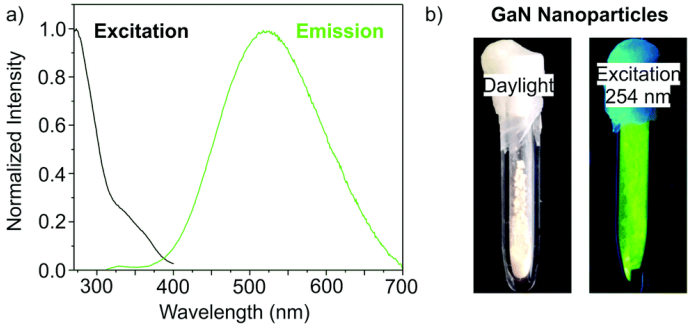

Figure 1.14 (a) Emission spectrum at 274 nm and excitation spectrum at 523 nm of the synthesized GaN. (b) Photographs of the as-synthesized GaN NCs in daylight and under excitation at 254 nm.Reprinted from Ref.[146] with permission from the Royal Society of Chemistry.

In 2006 Dingman *et al.* reported the synthesis of InN nanofibres at low temperatures (203 °C), catalyzed by nanometer sized droplets of In metal (also called a solution-

liquid-solid (SLS) mechanism).[147] The authors prepared two different indium precursors ($^{i}Pr_2InN_3$ and $^{t}Bu_2InN_3$) by reacting trialkylindium first with methanol and subsequently with trimethylsilylazide. Crystalline InN was then formed by reacting the as mentioned precursors with *1,1*-dimethylhydrazine ($H_2N{-}NMe_2$) at 203 °C for 20 h. The role of *1,1*-dimethylhydrazine is to reduce part of the indium precursors to In droplets, which then catalyze the InN crystallization.

$$R_3In + MeOH \xrightarrow{RT,10min} R_2InOMe + RH$$

$$R_2InOMe + TMSN_3 \xrightarrow{RT,210h} R_2InN_3 + TMSOMe$$

$$R_2InN_3 + H_2NNMe_2 \xrightarrow[20\ h]{203^{\circ}C} InN$$

In 2006 Choi *et al.* synthesized InN NCs from indium(III) bromide and sodium azide under solvothermal conditions.[148] The indium azide intermediate decomposes into InN and N_2.

$$InBr_3 + 3\ NaN_3 \xrightarrow{280^{\circ}C} [In(N_3)_3] + 3\ NaBr$$

$$[In(N_3)_3] \xrightarrow{280^{\circ}C} InN + 4\ N_2$$

The solvent used during the solvothermal treatment determines the final properties of the NCs. While toluene delivered 10 nm aggregated wurtzite InN, hexadecane yielded poorly crystalline InN. The reaction typically takes 3–5 days during which the reaction temperature is increased step by step to avoid explosive azide decomposition. Also, $In_xGa_{1-x}N$ alloyed particles were synthesized via this strategy.[148]

The reaction of potassium amide (KNH_2) and indium iodide in liquid ammonia yields an insoluble indium amide product. The latter is probably highly condensed, featuring imido bridges. Decomposition of this insoluble product at 400 °C under nitrogen atmosphere delivers InN, In, KNH_2, and NH_3.[149] Alternatively, InI_3 and $NaNH_2$ were reacted in anhydrous benzene in a Teflon-lined pressure bomb.[150] The crystallite

size of the resulting InN NCs varies from 9.9 ± 5 nm to 35.1 ± 10 nm by increasing the reaction time or temperature. At ambient pressure, InN NCs (6.2±2 nm diameter) have been synthesized using $InBr_3$ and $NaNH_2$ in hexadecane under an ammonia atmosphere.

$$InBr_3 + 3\ NaNH_2 \xrightarrow[3\ h]{250^\circ C} InN + In \tag{1.9}$$

A post-synthetic acid treatment (to remove In(0)) and functionalization with OLAm yielded colloidally stable particles, see Figure 1.15.[151] This method has been further studied by Palomaki *et al.* where they use In_2S_3 instead of $InBr_3$ and ODE as their solvent.[152]

$$In_2S_3 + NaNH_2 \xrightarrow[15\ min\ -\ 12\ h]{175\text{-}220^\circ C} InN + In \tag{1.10}$$

To improve the size dispersion, size-selective precipitation was performed by the drop-

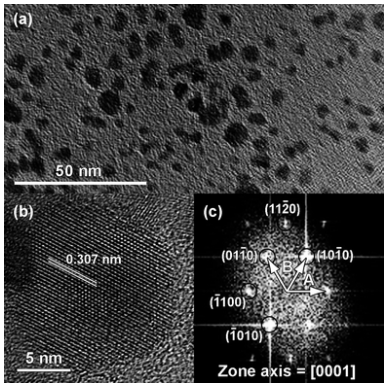

Figure 1.15 TEM images of the colloidally stable InN obtained by Hsieh *et al.* after acid treatment. (a)Low magnification image, (b) high resolution image, and (c) diffraction pattern obtained via fast Fourier transform (FFT). Reprinted with permission from reference[151] with permission from the Royal Society of Chemistry.

wise addition of acetonitrile to OLAm-capped InN NCs, and centrifugation. The final NCs size was tuned from 4.5 to 9.9 nm by varying the reaction time from 15 min to 12 h at 220 °C. The NCs size also increases from 4.1 to 8.0 nm by increasing the reaction temperature from 175 to 200 °C (at a fixed reaction time of 3 h). Below 175 °C, no InN

was formed. When $InCl_3.4H_2O$, $NaNH_2$, and sulfur were reacted in a pressure bomb at 160 °C for 30 h, wurtzite InN crystals (50–200 nm) were obtained.[153] According to *p*XRD, the reaction proceeds through a In_2S_3 intermediate. Even larger particles (500 nm) were obtained using $In(NO_3)_3.5H_2O$ as the precursor.

Colloidal InN NCs from lithium oleylamide

Beaulac and coworkers reported a surfactant-assisted procedure where all precursors are soluble.[154] $InBr_3$ is first dissolved in a mixture of OLAm and ODE solvent (or hexadecane). At 220 °C the authors inject lithium oleylamide, which was synthesized from OLAm, *n*-butyllithium (*n*-BuLi), and tetramethylethylenediamine (TMEDA). After 10 minutes, the reaction is stopped and the product is purified. TEM analysis shows that the obtained particles consist of a 30 nm In(0) core and InN outgrowths (Figure 1.16). The mixed composition of In and InN is confirmed by *p*XRD with sharp reflections for In and broader reflections for InN, consistent with their size difference (Figure 1.16). Using the same strategy as mentioned before, In is removed by nitric acid treatment and the InN NCs are stabilized by fictionalization with OLAm.[154]

Intrigued by the high dissociation energy of C-N bonds (330 $kJ.mol^{-1}$), Chen *et al.* investigated the mechanism of this reaction by analyzing the by-products via ^1H NMR, ^{13}C NMR, 2D homonuclear correlation spectroscopy (COSY) NMR, and mass spectrometry.[155] The authors propose that oleylamide is oxidized to oleylimine, thereby reducing In(III) to In(0), see Figure 1.17. A second equivalent of oleylamide performs a nucleophilic attack on the imine, yielding a secondary aldimine (RCH=NR) and releasing NH_2^-. The latter goes on to react with In(III) to form InN. The proposed mechanism is based on the observation of aldimine, ammonia, hydrogen, InN, and In as reaction products. Oleylimine is too unstable to be isolated. In(0) is always formed in larger yields than InN, meaning that not all reactive NH_2^- are converted to InN.

Other surfactant based strategies

$AlCl_3$, $GaCl_3$, and $InCl_3$ react with urea to form the crystalline complexes:

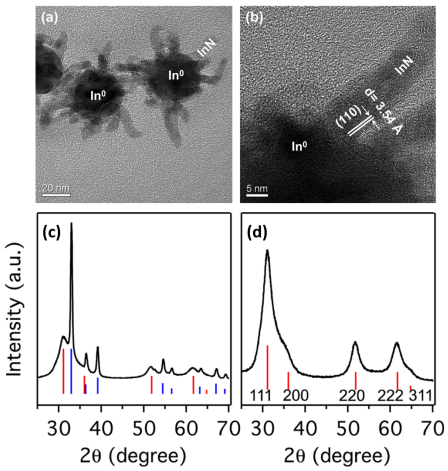

Figure 1.16 TEM images of the NCs. (a) Overview of the as prepared sample, showing the InN branches stemming out of larger In(0) NCs. (b) HR-TEM image of one of the InN branches in (a) at the surface of the In(0) NCs. *p*XRD pattern for the (c) as-prepared sample and (d) acid treated sample. The vertical lines show the *p*XRD patterns of bulk zincblende-InN (red) and tetragonal In(0) (blue). Reprinted with permission from reference.[154] Copyright 2016 American Chemical Society.

$[Al(H_2NCONH_2)_6]Cl_3$, $[Ga(H_2NCONH_2)_6]Cl_3$, and $In(H_2NCONH_2)_3Cl_3$.[156] In the aluminum and gallium complexes, six urea molecules are coordinated to the metal and the chloride is simply the counter ion of the positively charged complex. In the indium complex, three urea molecules and 3 chlorides build up the first coordination sphere. Pyrolysis of the complexes under nitrogen yields AlN, GaN, or a mixture of InN and In_2O_3. Refluxing $[Ga(H_2NCONH_2)_6]Cl_3$ in tri-*n*-octylamine (365 °C) for 24 h yields colloidal GaN NCs (2–3 nm). These particles show photoluminescence spectroscopy (PL) emission bands at 340 and 380 nm. Refluxing the Al and In complex yields AlN and InN (with a minor indium oxide impurity) respectively. Later, the authors showed that the obtained GaN NCs were amorphous, and further annealing in ammonia at 450 °C for 24 h was necessary to improve their crystallinity.[157] In 2019, Choi *et al.* designed a hot-injection strategy to obtain GaN QDs.[158] Gallium chloride and stearic acid were dissolved in ODE and heated to 280 °C under argon. Subsequently, a solution

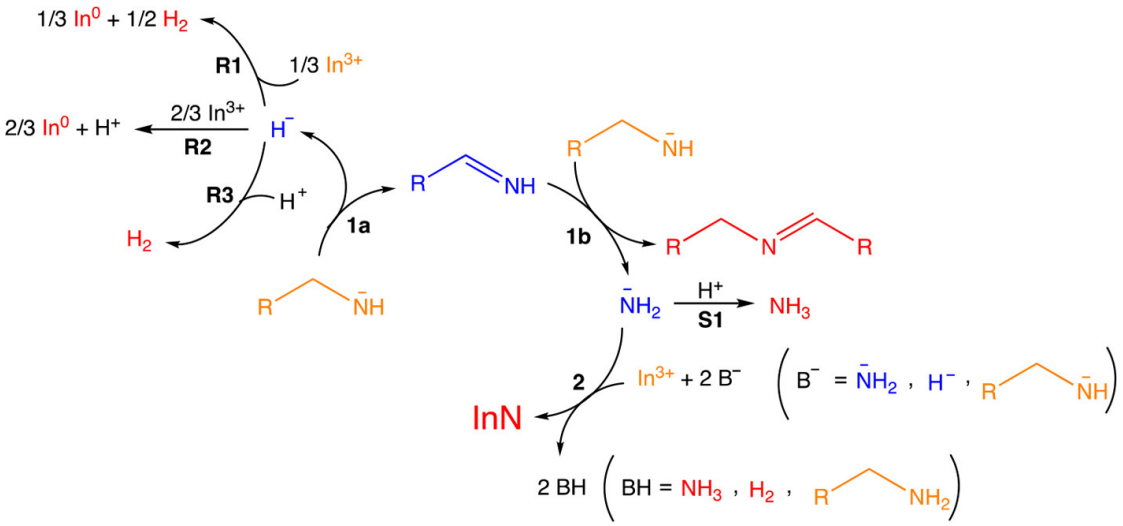

Figure 1.17 Overall reaction mechanism of InP. Reaction 1a, alkylamide precursor oxidation; reaction 1b, formation of the secondary imine leading to NH_2^- production; reaction 2, nitride formation; R1, R2, R3, three hypothetical reduction processes concomitant with reaction 1a; S1, detrimental hypothetical side reaction. Orange, reactants; blue, intermediates (not isolated); red, identified products. Uncoordinated forms are depicted here for simplicity. Reprinted with permission from reference.[155] Copyright 2018 American Chemical Society.

of lithium bis(trimethylsilyl)amide in hexane was rapidly injected.

$$GaCl_3 + LiN(TMS)_2 \xrightarrow[\text{ODE, stearic acid}]{\text{220-280 °C, 10-90 min}} GaN \tag{1.11}$$

The NCs size was hard to determine from TEM but surely below 5 nm, which is also confirmed by the very broad nature of the *p*XRD reflections. The PL emission of the QDs could be tuned from 315–355 nm, while the bulk PL is at 365 nm. Successful doping with zinc red-shifted the PL to 330–460 nm.[158]

In the forthcoming section, we will transition from the comprehensive literature review to an exploration of the methodological toolkit that has been instrumental throughout this doctoral research.

1.3 Methodological toolkit

This thesis revolves around NCs characterized by a hybrid organic-inorganic structure. The physical properties of these particles arise from the inorganic core, while their chemical attributes are influenced by the organic ligands. This design principle is tailored to ensure the colloidal stability of these particles when they are dispersed in a solution. For the examination of the inorganic core, as well as the assessment of crystallinity and phase purity, the primary method employed is x-ray powder diffraction (pXRD). Following this, additional techniques such as transmission electron microscopy (TEM) and x-ray total scattering and pair distribution function analysis (PDF) are utilized to offer further insights into particle size and the identification of local defects. When shifting the focus towards the analysis of the ligands, thermogravimetric analysis (TGA), fourier-transform infrared spectroscopy (FT-IR), nuclear magnetic resonance (NMR), and dynamic light scattering (DLS) have emerged as valuable methods. These techniques provide essential insights into the chemical nature of the ligands, quantification, and overall size of the NCs. This section will delve into the specific applications of pXRD and NMR techniques in greater detail.

1.3.1 X-ray powder diffraction

pXRD is one of the primary methods used to determine the atomic arrangement within a crystalline sample in powder form. This method relies on the principles of diffraction theory, as first formulated by Bragg's law. According to this theory, when incident X-ray radiation with a defined wavelength (λ) interacts with a crystal, constructive scattering occurs at specific angles (θ), as described by Equation 1.12, where (d) represents the distance between crystallographic planes and (n) represents an integer that corresponds to the order of the diffraction peak.

$$2dsin(\theta) = n\lambda \tag{1.12}$$

For every angle at which Bragg's law is satisfied, a reflection is observed in the diffractogram obtained using a fixed X-ray source. The width of each reflection is characteristic of the size of the crystallite. A sharp reflection corresponds to an infinite periodicity of the crystallite, typically corresponding to at least a few microns, whereas a broad reflection corresponds to NCs. The Scherrer equation (Equation 1.13) is employed to estimate the crystallite size (d).

$$d = \frac{0.9\lambda}{\beta cos\theta} \tag{1.13}$$

In the Scherrer equation, (θ) represents the diffraction angle, (λ) is the wavelength of the X-ray, and (β) is the full width at half maximum (FWHM) of the diffraction peak. The Scherrer equation is particularly effective for estimating the crystallite size when dealing with isotropic particles with sizes ranging from 5 to 50 nm. In the case of an anisotropic structure, the diffraction pattern can vary depending on the crystallographic direction. Sharp peaks are observed for the crystallographic direction with a high periodicity, indicating a strong diffraction signal, while broader peaks are seen for the direction with a shorter periodicity, suggesting weaker diffraction along that direction. The position of the reflection allows for the determination of a lattice constant. Lattice constants offer valuable insights into the structure of pure solids, as well as doped or alloyed materials. When a dopant has a larger radius than the initial ion it is replacing, the lattice expands, leading to an increase in the lattice constant. Consequently, this shift in the reflection peak occurs at lower 2θ angles in the diffractogram.[159]

1.3.2 1D NMR spectra

^{1}H NMR is employed as a primary tool for analyzing the surface chemistry of particles. When a molecule is bound to the surface, its resonances appear broader compared to when it is unbound or free in solution. The broadening of resonances in bound ligands arises from two distinct processes known as homogeneous and heterogeneous broadening. The homogeneous line width is directly proportional to the T_2 relaxation rate and increases with the size of the object. In the case of an unbound molecule, such as oleic

acid (OA), it demonstrates a significant degree of rotational freedom, leading to rapid tumbling. This rapid tumbling results in longer T_2 relaxation times, giving rise to sharp and well-defined resonances. However, upon binding OA to the surface of the nanoparticles (NPs), its rotational freedom becomes constrained, inducing slower tumbling and accelerated relaxation, thus shortening the T_2 time. This alteration broadens the resonance lines, a phenomenon attributed to homogeneous broadening. Furthermore, within NMR, another type of broadening is observed known as heterogeneous broadening. This phenomenon arises from the combination of resonances originating from varied chemical environments encountered by the bound ligands, resulting in distinct chemical shifts. The extent of this broadening phenomenon is heavily influenced by the affinity between the ligand shell and the solvent. When the ligand shell exhibits a high affinity for the solvent, it becomes well-solvated, resulting in fewer ligand-ligand interactions, leading to a decrease in heterogeneous line broadening. If there is a low affinity between the ligand shell and the solvent, the solvent is excluded from the ligand shell, leading to interactions between ligands in diverse ways. This interaction gives rise to heterogeneous line broadening. Homogeneous line broadening in the ligand shell tends to escalate proportionally with the size of the NPs. As the dimensions of the NPs increase, the ligand shell expands, resulting in a more pronounced homogeneous line broadening effect. However, heterogeneous line width initially increases with the size of the NPs until it reaches a saturation point at a core size of approximately 8–10 nm. Beyond this core size, further enlargement of the NPs has negligible influence on the extent of heterogeneous line broadening (Figure 1.18).[160;161]

1.3.3 Diffusion ordered NMR spectroscopy

Diffusion ordered spectroscopy (DOSY) is an additional tool in the field of NMR that aids in the identification of bound and unbound molecules within a mixture. This technique relies on analyzing the diffusion coefficient of molecules to assess their state. The speed at which molecules move in a solution is directly influenced by factors such as size, shape, and chemical environment. Smaller molecules, like unbound ligands, tend to diffuse

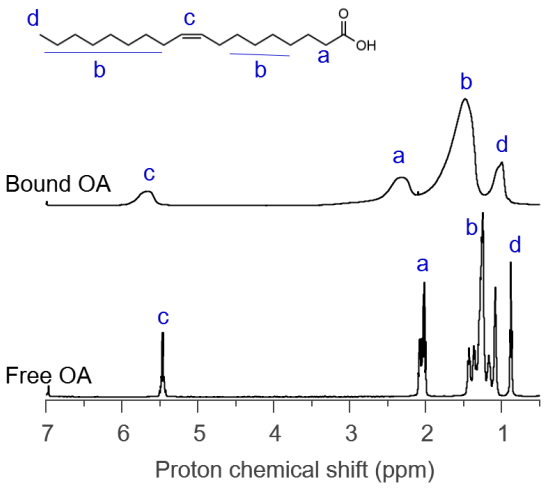

Figure 1.18 | ^{1}H NMR of OA as a free molecule compared to tightly bound OA to the surface of ZrO_2 NCs in benzene-d_6.

more rapidly as they move freely in the solution. On the other hand, larger molecules, such as ligands bound to a NCs, exhibit limited movement and diffuse more slowly. By measuring the differences in diffusion coefficients, it becomes possible to differentiate between bound and unbound ligands.

The DOSY measurement involves the utilization of pulsed Field Gradient NMR, which employs a magnetic field gradient (g) along the z-axis for a short duration (δ). This gradient causes each spin to have a distinct frequency based on its position along the z-axis. Subsequently, a diffusion time (Δ) is introduced, allowing the molecules to diffuse and change their positions within the sample. After this diffusion period, an identical but opposite gradient (g) is applied. When a molecule's spin does not exhibit diffusion motion, the z-dependent frequency remains unchanged after the application of the gradients, leading to complete refocusing. However, if the spins undergo diffusion motion, they will occupy different z-positions, causing them to experience varying amplitudes for the opposite magnetic field gradient. As a result, the refocusing is incomplete, leading to a reduction in the intensity of the resulting signal.

The diffusion coefficient is acquired by conducting a series of 1D spectra while varying

the applied gradient strength. The decay of peak intensity (I) is determined using the Stejskal-Tanner equation, which relates it to the intensity at zero gradient strength (I_0), the gyromagnetic ratio (γ), the gradient length (δ), and the diffusion time (Δ). During the pulsed field gradient experiment, the latter two parameters remain constant. The relationship is expressed by the following equation 1.14.

$$I = I_0 e^{-(\gamma \delta g)^2 D(\Delta - 0.6\delta)} \tag{1.14}$$

By utilizing Equation 1.14, the natural logarithm of the intensity (ln(I)) is plotted as a function of the squared gradient strength (g^2). When dealing with a single diffusing species, a mono-exponential decay is observed, resulting in a straight line. However, when two species with different diffusion coefficients are present and overlapping, a bi-exponential decay is expected.

In the scenario of a tightly bound ligand to a NCs, the organic molecule diffuses in conjunction with the NC. The term *solvodynamic diameter* refers to the total diameter of the particle representing the combined size of the particle and the bound organic molecule together with the first solvent shell. It is possible to establish a correlation between the diffusion coefficient and the solvodynamic diameter using the Stokes-Einstein Equation 1.15, where (D) represents the diffusion coefficient, (T) represents the temperature, (η) represents the viscosity of the solvent, and (d_s) corresponds to the solvodynamic diameter.

$$D = \frac{K_B T}{3\pi\eta d_s} \tag{1.15}$$

The dynamics of ligand binding can be assessed by comparing the expected solvodynamic diameter to the observed diameter. For a tightly bound ligand, the expected solvodynamic diameter corresponds to the sum of the diameter of the NCs with twice the length of the ligand. If the observed diameter is smaller than the expected diameter, it suggests the presence of a combination of tightly bound and free ligands (indicating incomplete purification) or loosely bound ligands (in a fast exchange). The observed

diameter, D_{obs}, can then be expressed as a weighted average of bound and free ligands.

$$D_{obs} = \chi_{bound} D_{bound} + \chi_{free} D_{free} \tag{1.16}$$

1.4 Outline

Up to date, it is clear that the late transition metals and group 13 metal nitrides have been more extensively studied. While the reaction mechanism (precursor conversion) is most studied for the group 13 nitrides, the most uniform nanocrystals are obtained for Cu_3N. At the same time, we were forced to conclude that there do not exist any convincing reports of the colloidal synthesis of group 4 and group 5 nitrides. Only nanopowders were successfully obtained, of which some could be dispersed in water, albeit in aggregated form. An additional hurdle for the group 4 and 5 nitrides is the required reduction during the synthesis. For example, most common precursors for TiN and TaN are based on Ti(IV) or Ta(V), while the final nitrides contain the metal in the +III oxidation state. This thesis primarily focuses on the development of novel synthesis strategies for metal nitride NCs, with a particular emphasis on Cu_3N, a nitride compound that has received attention in the literature.

Chapter 2 delves into the precursor conversion chemistry and surface chemistry of both Cu_3N and Cu_3PdN NCs. Within this chapter, we successfully obtain phase-pure nanocubes that exhibit colloidal stability, marking a significant achievement in the synthesis of these materials. The elucidation of the pathway by which copper(II) nitrate and OLAm form Cu_3N is a central focus. Our findings reveal that OLAm serves a dual role as both a reductant and a nitrogen source. In addition to the synthesis aspects, we thoroughly investigate the surface chemistry of these NCs. Our results indicate the presence of a mixed ligand shell composed of aliphatic amines and carboxylates, which are formed in situ during the synthesis process.

In line with this inspiration, in Chapter 3 we explore alternative solution-based methods for obtaining various metal nitrides, including TiN, Ni_3N, and Zn_3N_2. In this pursuit, we have systematically investigated various strategies, involving diverse nitrogen sources

and mechanisms to drive the reactions, such as Si-halogen bond formation and salt formation, all with the primary goal of generating ammonia or nitrogen sources readily available to react with the metal in the process. This chapter provides a comprehensive summary of the results derived from these different approaches and experimental investigations.

Throughout the experiments, the crystallization step consistently emerges as the bottleneck. In order to surmount this challenge, we adopted a solid-state approach (Chapter 4). However, solid-state reactions often demand high temperatures exceeding 500 °C. To circumvent this limitation, we turned to molten salts as a high temperature solvent system. Through our exploration of TiN synthesis in various molten salt environments, we identified an optimized synthesis method that allowed us to significantly reduce the temperature to as low as 350 °C while maintaining excellent crystallinity. To the best of our knowledge, this represents the pioneering achievement of obtaining highly crystalline TiN NCs at such reduced temperatures.

When dealing with NCs, maintaining colloidal stability is consistently a crucial consideration. Silanes, a versatile class of materials, are frequently employed as surfactants. They exhibit remarkable versatility due to the presence of diverse functional groups within their molecular structures, rendering them suitable for a wide range of applications, particularly in the realm of biocompatibility. Numerous studies have documented the process of ligand exchange from native ligands to silanes post-synthesis.

In Chapter 5, we embarked on a more in-depth exploration of the exchange mechanism, seeking to elucidate both the substances being released and those potentially adhering to the surface. These preliminary findings lay the groundwork for future investigations in this field.

References

[1] Kwon, S. G.; Hyeon, T. Colloidal Chemical Synthesis and Formation Kinetics of Uniformly Sized Nanocrystals of Metals, Oxides, and Chalcogenides. *Accounts of Chemical Research* **2008**, *41*, 1696–1709.

[2] Hens, Z.; De Roo, J. Atomically Precise Nanocrystals. *Journal of the American Chemical Society* **2020**, *142*, 15627–15637.

[3] Matijevic, E. Preparation and properties of uniform size colloids. *Chemistry of Materials* **1993**, *5*, 412–426.

[4] Park, J.; Joo, J.; Kwon, S. G.; Jang, Y.; Hyeon, T. Synthesis of monodisperse spherical nanocrystals. *Angewandte Chemie International Edition* **2007**, *46*, 4630–4660.

[5] Ojea-Jiménez, I.; Romero, F. M.; Bastús, N. G.; Puntes, V. Small Gold Nanoparticles Synthesized with Sodium Citrate and Heavy Water: Insights into the Reaction Mechanism. *Journal of Physical Chemistry C* **2010**, *114*, 1800–1804.

[6] Garcia-Rodriguez, R.; Hendricks, M. P.; Cossairt, B. M.; Liu, H. T.; Owen, J. S. Conversion Reactions of Cadmium Chalcogenide Nanocrystal Precursors. *Chemistry of Materials* **2013**, *25*, 1233–1249.

[7] Niederberger, M.; Garnweitner, G. Organic reaction pathways in the nonaqueous synthesis of metal oxide nanoparticles. *Chemistry-a European Journal* **2006**, *12*, 7282–7302.

[8] Tessier, M. D.; De Nolf, K.; Dupont, D.; Sinnaeve, D.; De Roo, J.; Hens, Z. Aminophosphines: A Double Role in the Synthesis of Colloidal Indium Phosphide Quantum Dots. *Journal of the American Chemical Society* **2016**, *138*, 5923–5929.

[9] Boles, M. A.; Ling, D.; Hyeon, T.; Talapin, D. V. The surface science of nanocrystals. *Nature Materials* **2016**, *15*, 141–53.

[10] De Roo, J.; Van den Broeck, F.; De Keukeleere, K.; Martins, J. C.; Van Driessche, I.; Hens, Z. Unravelling the Surface Chemistry of Metal Oxide Nanocrystals, the Role of Acids and Bases. *Journal of the American Chemical Society* **2014**, *136*, 9650–9657.

[11] Eagle, F. W.; Park, N.; Cash, M.; Cossairt, B. M. Surface Chemistry and Quantum Dot Luminescence: Shell Growth, Atomistic Modification, and Beyond. *American Chemical Society Energy Letters* **2021**, *0*, 977–984.

[12] Kister, T.; Monego, D.; Mulvaney, P.; Widmer-Cooper, A.; Kraus, T. Colloidal Stability of Apolar Nanoparticles: The Role of Particle Size and Ligand Shell Structure. *American Chemical Society Nano* **2018**, *12*, 5969–5977.

[13] Yang, Y.; Qin, H.; Peng, X. Intramolecular Entropy and Size-Dependent Solution Properties of Nanocrystal–Ligands Complexes. *Nano Letters* **2016**, *16*, 2127–2132.

[14] Anderson, N. C.; Owen, J. S. Soluble, Chloride-Terminated CdSe Nanocrystals: Ligand Exchange Monitored by H-1 and P-31 NMR Spectroscopy. *Chemistry of Materials* **2013**, *25*, 69–76.

[15] De Roo, J.; Van Driessche, I.; Martins, J. C.; Hens, Z. Colloidal metal oxide nanocrystal catalysis by sustained chemically driven ligand displacement. *Nature Materials* **2016**, *15*, 517–521.

[16] Martin, J. D. Particle Size Is a Primary Determinant for Sigmoidal Kinetics of Nanoparticle Formation: A "Disproof" of the Finke–Watzky (F-W) Nanoparticle Nucleation and Growth Mechanism. *Chemistry of Materials* **2020**, *32*, 3651–3656.

[17] Finke, R. G.; Watzky, M. A.; Whitehead, C. B. Response to "Particle Size Is a Primary Determinant for Sigmoidal Kinetics of Nanoparticle Formation: A "Disproof" of the Finke–Watzky (F-W) Nanoparticle Nucleation and Growth Mechanism". *Chemistry of Materials* **2020**, *32*, 3657–3672.

[18] Lamer, V. K.; Dinegar, R. H. Theory, Production and Mechanism of Formation of Monodispersed Hydrosols. *Journal of the American Chemical Society* **1950**, *72*, 4847–4854.

[19] Özkar, S.; Finke, R. G. Nanoparticle Nucleation Is Termolecular in Metal and Involves Hydrogen: Evidence for a Kinetically Effective Nucleus of Three $[Ir_3H_{2x} \cdot P_2W_{15}Nb_3O_{62}]^{6-}$ in $Ir(0)_n$ Nanoparticle Formation From $[(1,5\text{-COD})Ir^{I} \cdot P_2W_{15}Nb_3O_{62}]^{8-}$ Plus Dihydrogen. *Journal of the American Chemical Society* **2017**, *139*, 5444–5457.

[20] Mozaffari, S.; Li, W.; Thompson, C.; Ivanov, S.; Seifert, S.; Lee, B.; Kovarik, L.; Karim, A. M. Colloidal nanoparticle size control: experimental and kinetic modeling investigation of the ligand–metal binding role in controlling the nucleation and growth kinetics. *Nanoscale* **2017**, *9*, 13772–13785.

[21] McMurtry, B. M.; Qian, K.; Teglasi, J. K.; Swarnakar, A. K.; De Roo, J.; Owen, J. S. Continuous Nucleation and Size Dependent Growth Kinetics of Indium Phosphide Nanocrystals. *Chemistry of Materials* **2020**, *32*, 4358–4368.

[22] Prins, P. T. et al. Extended Nucleation and Superfocusing in Colloidal Semiconductor Nanocrystal Synthesis. *Nano Letters* **2021**, *21*, 2487–2496.

[23] Mozaffari, S.; Li, W.; Dixit, M.; Seifert, S.; Lee, B.; Kovarik, L.; Mpourmpakis, G.; Karim, A. M. The role of nanoparticle size and ligand coverage in size focusing of colloidal metal nanoparticles. *Nanoscale Advances* **2019**, *1*, 4052–4066.

[24] Handwerk, D. R.; Shipman, P. D.; Whitehead, C. B.; Özkar, S.; Finke, R. G. Mechanism-Enabled Population Balance Modeling of Particle Formation en Route

to Particle Average Size and Size Distribution Understanding and Control. *Journal of the American Chemical Society* **2019**, *141*, 15827–15839.

[25] Hendricks, M. P.; Campos, M. P.; Cleveland, G. T.; Plante, I. J.-L.; Owen, J. S. A tunable library of substituted thiourea precursors to metal sulfide nanocrystals. *Science* **2015**, *348*, 1226–1230.

[26] Dhaene, E.; Billet, J.; Bennett, E.; Van Driessche, I.; De Roo, J. The Trouble with ODE: Polymerization during Nanocrystal Synthesis. *Nano Letters* **2019**, *19*, 7411–7417.

[27] De Keukeleere, K.; Coucke, S.; De Canck, E.; Van Der Voort, P.; Delpech, F.; Coppel, Y.; Hens, Z.; Van Driessche, I.; Owen, J. S.; De Roo, J. Stabilization of Colloidal Ti, Zr, and Hf Oxide Nanocrystals by Protonated Tri-n-octylphosphine Oxide (TOPO) and Its Decomposition Products. *Chemistry of Materials* **2017**, *29*, 10233–10242.

[28] Baranov, D.; Lynch, M. J.; Curtis, A. C.; Carollo, A. R.; Douglass, C. R.; Mateo-Tejada, A. M.; Jonas, D. M. Purification of Oleylamine for Materials Synthesis and Spectroscopic Diagnostics for trans Isomers. *Chemistry of Materials* **2019**, *31*, 1223–1230.

[29] Calvin, J. J.; Swabeck, J. K.; Sedlak, A. B.; Kim, Y.; Jang, E.; Alivisatos, A. P. Thermodynamic Investigation of Increased Luminescence in Indium Phosphide Quantum Dots by Treatment with Metal Halide Salts. *Journal of the American Chemical Society* **2020**, *142*, 18897–18906.

[30] Friedfeld, M. R.; Stein, J. L.; Ritchhart, A.; Cossairt, B. M. Conversion Reactions of Atomically Precise Semiconductor Clusters. *Accounts of Chemical Research* **2018**, *51*, 2803–2810.

[31] Mundy, M. E.; Ung, D.; Lai, N. L.; Jahrman, E. P.; Seidler, G. T.; Cossairt, B. M. Aminophosphines as Versatile Precursors for the Synthesis of Metal Phosphide Nanocrystals. *Chemistry of Materials* **2018**, *30*, 5373–5379.

[32] Rachkov, A. G.; Schimpf, A. M. Colloidal Synthesis of Tunable Copper Phosphide Nanocrystals. *Chemistry of Materials* **2021**, *33*, 1394–1406.

[33] Sadoway, D. R. The eelectrochemical processing of refractory metals. *JOM* **1991**, *43*, 15–19.

[34] MIURA, A. Low-temperature synthesis and rational design of nitrides and oxynitrides for novel functional material development. *Journal of the Ceramic Society of Japan* **2017**, *125*, 552–558.

[35] Fung, K.; Mantov, G. Electrochemistry of titanium(II) in $AlCl_3$ + NaCl melts. *Journal of Electroanalytical Chemistry and Interfacial Electrochemistry* **1972**, *35*, 27–34.

[36] Housecroft, C. *Inorganic Chemistry*; Pearson, 2018; Vol. 72, pp 650–651.

[37] Elder, S. H.; DiSalvo, F. J.; Topor, L.; Navrotsky, A. Thermodynamics of ternary nitride formation by ammonolysis: application to lithium molybdenum nitride ($LiMoN_2$), sodium tungsten nitride (Na_3WN_3), and sodium tungsten oxide nitride (Na_3WO_3N). *Chemistry of Materials* **1993**, *5*, 1545–1553.

[38] Karaballi, R. A.; Humagain, G.; Fleischman, B. R. A.; Dasog, M. Synthesis of Plasmonic Group-4 Nitride Nanocrystals by Solid-State Metathesis. *Angewandte Chemie International Edition* **2019**, *58*, 3147–3150.

[39] Ishii, S.; Sugavaneshwar, R. P.; Nagao, T. Titanium Nitride Nanoparticles as Plasmonic Solar Heat Transducers. *Journal of Physical Chemistry C* **2016**, *120*, 2343–2348.

[40] Traver, E.; Karaballi, R. A.; Monfared, Y. E.; Daurie, H.; Gagnon, G. A.; Dasog, M. TiN, ZrN, and HfN Nanoparticles on Nanoporous Aluminum Oxide Membranes for Solar-Driven Water Evaporation and Desalination. *American Chemical Society Applied Nano Materials* **2020**, *3*, 2787–2794.

[41] Karaballi, R. A.; Monfared, Y. E.; Dasog, M. Overview of Synthetic Methods to Prepare Plasmonic Transition-Metal Nitride Nanoparticles. *Chemistry* **2020**, *26*, 8499–8505.

[42] Karaballi, R. A.; Esfahani Monfared, Y.; Dasog, M. Photothermal Transduction Efficiencies of Plasmonic Group 4 Metal Nitride Nanocrystals. *Langmuir* **2020**, *36*, 5058–5064.

[43] Guler, U.; Suslov, S.; Kildishev, A. V.; Boltasseva, A.; Shalaev, V. M. Colloidal Plasmonic Titanium Nitride Nanoparticles: Properties and Applications. *Nanophotonics* **2015**, *4*, 269–276.

[44] Yuan, Y.; Wang, J.; Adimi, S.; Shen, H.; Thomas, T.; Ma, R.; Attfield, J. P.; Yang, M. Zirconium nitride catalysts surpass platinum for oxygen reduction. *Nature Materials* **2019**, *19*, 282–286.

[45] Defilippi, C.; Shinde, D. V.; Dang, Z.; Manna, L.; Hardacre, C.; Greer, A. J.; D'Agostino, C.; Giordano, C. HfN Nanoparticles: An Unexplored Catalyst for the Electrocatalytic Oxygen Evolution Reaction. *Angewandte Chemie International Edition* **2019**, *58*, 15464–15470.

[46] Momma, K.; Izumi, F. "VESTA 3 for three-dimensional visualization of crystal, volumetric and morphology data,". *Journal of Applied Crystallography* **2011**, *44*, 1272–1276.

[47] Christensen, A. N.; Romano, V.; Hesse, R.; Andresen, A. F.; Fischer, P. A Neutron Diffraction Investigation on Single Crystals of Titanium Carbide, Titanium Nitride, and Zirconium Nitride. *Acta Chemica Scandinavica* **1975**, *29a*, 563–564.

[48] Glaser, F. W.; Moskowitz, D.; Post, B. A Study of Some Binary Hafnium Compounds. *JOM* **1953**, *5*, 1119–1120.

[49] Becker, K.; Ebert, F. Die Kristallstruktur einiger binärer Carbide und Nitride. *Zeitschrift für Physik* **1925**, *31*, 268–272.

[50] Hiltunen, L.; Leskela, M.; Makela, M.; Niinisto, L.; Nykanen, E.; Soininen, P. Nitrides of titanium, niobium, tantalum and molybdenum grown as thin-films by the atomic layer epitaxy method. *Thin Solid Films* **1988**, *166*, 149–154.

[51] Kafizas, A.; Carmalt, C. J.; Parkin, I. P. CVD and precursor chemistry of transition metal nitrides. *Coordination Chemistry Reviews* **2013**, *257*, 2073–2119.

[52] Alvarez Barragan, A.; Ilawe, N. V.; Zhong, L.; Wong, B. M.; Mangolini, L. A Non-Thermal Plasma Route to Plasmonic TiN Nanoparticles. *Journal of Physical Chemistry C* **2017**, *121*, 2316–2322.

[53] Schramke, K. S.; Qin, Y. X.; Held, J. T.; Mkhoyan, K. A.; Kortshagen, U. R. Nonthermal Plasma Synthesis of Titanium Nitride Nanocrystals with Plasmon Resonances at Near-Infrared Wavelengths Relevant to Photothermal Therapy. *Acs Applied Nano Materials* **2018**, *1*, 2869–2876.

[54] Exarhos, S.; Alvarez-Barragan, A.; Aytan, E.; Balandin, A. A.; Mangolini, L. Plasmonic Core–Shell Zirconium Nitride–Silicon Oxynitride Nanoparticles. *American Chemical Society Energy Letters* **2018**, *3*, 2349–2356.

[55] Winter, C. H.; Sheridan, P. H.; Lewkebandara, T. S.; Heeg, M. J.; Proscia, J. W. A Single-Source Precursor to Titanium Nitride Thin-Films - Evidence for the Intermediacy of Imido Complexes in the Chemical Vapor-Deposition Process. *Journal of the American Chemical Society* **1992**, *114*, 1095–1097.

[56] Dunn, S. C.; Batsanov, A. S.; Mountford, P. A general route to sandwich and half-sandwich titanium imido complexes: X-ray structure of [Ti(η4-Me8taa)(NBut)](Me4taa = tetramethyldibenzotetraaza[14]annulene). *Journal of the Chemical Society, Chemical Communications* **1994**, 2007–2008.

[57] Fischer, A.; Antonietti, M.; Thomas, A. Growth confined by the nitrogen source: Synthesis of pure metal nitride nanoparticles in mesoporous graphitic carbon nitride. *Advanced Materials* **2007**, *19*, 264–267.

[58] Buha, J.; Djerdj, I.; Antonietti, M.; Niederberger, M. Thermal transformation of metal oxide nanoparticles into nanocrystalline metal nitrides using cyanamide and urea as nitrogen source. *Chemistry of Materials* **2007**, *19*, 3499–3505.

[59] Liu, Y.; Zhang, X.; Lu, L.; Ye, J.; Wang, J.; Li, X.; Bai, X.; Wang, W. Nanoplasmonic zirconium nitride photocatalyst for direct overall water splitting. *Chinese Chemical Letters* **2021**, *33*, 1271–1274.

[60] Giordano, C.; Erpen, C.; Yao, W. T.; Milke, B.; Antonietti, M. Metal Nitride and Metal Carbide Nanoparticles by a Soft Urea Pathway. *Chemistry of Materials* **2009**, *21*, 5136–5144.

[61] Shanker, G. S.; Bhosale, R.; Ogale, S.; Nag, A. 2D Nanocomposite of g-C_3N_4 and TiN Embedded N-Doped Graphene for Photoelectrochemical Reduction of Water Using Sunlight. *Advanced Materials Interfaces* **2018**, *5*, 1801488.

[62] Shanker, G. S.; Markad, G. B.; Jagadeeswararao, M.; Bansode, U.; Nag, A. Colloidal Nanocomposite of TiN and N-Doped Few-Layer Graphene for Plasmonics and Electrocatalysis. *American Chemical Society Energy Letters* **2017**, *2*, 2251–2256.

[63] Hosoya, S.; Yamagishi, T.; Tokonami, M. Study of Electron State in Vanadium Nitride by Intensity Measurements of X-Ray Diffraction. *Journal of the Physical Society of Japan* **1968**, *24*, 363–367.

[64] Gatterer, J.; Dufek, G.; Ettmayer, P.; Kieffer, R. Das kubische Tantalmononitrid (B 1-Typ) und seine Mischbarkeit mit den isotypen Übergangsmetallnitriden undcarbiden. *Monatshefte für Chemie - Chemical Monthly* **1975**, *106*, 1137–1147.

[65] Liu, Y.; Wu, Q.; Liu, L.; Manasa, P.; Kang, L.; Ran, F. Vanadium nitride for aqueous supercapacitors: a topic review. *Journal of Materials Chemistry A* **2020**, *8*, 8218–8233.

[66] Cui, H.; Zhu, G.; Liu, X.; Liu, F.; Xie, Y.; Yang, C.; Lin, T.; Gu, H.; Huang, F. Niobium Nitride Nb_4N_5 as a New High-Performance Electrode Material for Supercapacitors. *Advanced Science* **2015**, *2*, 1500126.

[67] Li, Z.; He, Q.; Xu, X.; Zhao, Y.; Liu, X.; Zhou, C.; Ai, D.; Xia, L.; Mai, L. A 3D Nitrogen-Doped Graphene/TiN Nanowires Composite as a Strong Polysulfide Anchor for Lithium-Sulfur Batteries with Enhanced Rate Performance and High Areal Capacity. *Advanced Materials* **2018**, *30*, e1804089.

[68] Choi, D.; Blomgren, G.; Kumta, P. Fast and Reversible Surface Redox Reaction in Nanocrystalline Vanadium Nitride Supercapacitors. *Advanced Materials* **2006**, *18*, 1178–1182.

[69] Huang, T.; Mao, S.; Zhou, G.; Wen, Z.; Huang, X.; Ci, S.; Chen, J. Hydrothermal synthesis of vanadium nitride and modulation of its catalytic performance for oxygen reduction reaction. *Nanoscale* **2014**, *6*, 9608.

[70] Choi, D.; Kumta, P. N. Synthesis and Characterization of Nanostructured Niobium and Molybdenum Nitrides by a Two-Step Transition Metal Halide Approach. *Journal of the American Ceramic Society* **2011**, *94*, 2371–2378.

[71] Swisher, J. H.; Read, M. H. Thermodynamic Properties and Electrical Conductivity of Ta_3n_5 and Taon. *Metallurgical Transactions* **1972**, *3*, 493–498.

[72] Wang, L.; Zhou, X.; Nguyen, N. T.; Hwang, I.; Schmuki, P. Strongly Enhanced Water Splitting Performance of Ta_3N_5 Nanotube Photoanodes with Subnitrides. *Adv Mater* **2016**, *28*, 2432–8.

[73] Tsai, M. H.; Sun, S. C.; Chiu, H. T.; Tsai, C. E.; Chuang, S. H. Metalorganic Chemical-Vapor-Deposition of Tantalum Nitride by Tertbutylimidotris(Diethylamido)Tantalum for Advanced Metallization. *Applied Physics Letters* **1995**, *67*, 1128–1130.

[74] Lee, Y.-J.; Kim, D.-Y.; Lee, K.-H.; Han, M.-H.; Kang, K.-S.; Bae, K.-K.; Lee, J.-H. Ammonium fluoride-activated synthesis of cubic δ-TaN nanoparticles at low temperatures. *Nanoscale Research Letters* **2013**, *8*, 1–9.

[75] Ho, C.-T.; Low, K.-B.; Klie, R. F.; Maeda, K.; Domen, K.; Meyer, R. J.; Snee, P. T. Synthesis and Characterization of Semiconductor Tantalum Nitride Nanoparticles. *Journal of Physical Chemistry C* **2010**, *115*, 647–652.

[76] Mallinson, C. F.; Gray, B. M.; Hector, A. L.; McLachlan, M. A.; Owen, J. R. Templated non-oxide sol-gel preparation of well-ordered macroporous (inverse opal) Ta3N5 films. *Inorganic Chemistry* **2013**, *52*, 9994–9.

[77] Leineweber, A.; Jacobs, H.; Hull, S. Ordering of Nitrogen in Nickel Nitride Ni_3N Determined by Neutron Diffraction. *Inorganic Chemistry* **2001**, *40*, 5818–5822.

[78] Gillot, F.; Oró-Solé, J.; Palacín, M. R. Nickel nitride as negative electrode material for lithium ion batteries. *Journal of Materials Chemistry* **2011**, *21*, 9997–10002.

[79] Dunand, D. C.; Müllner, P. Size Effects on Magnetic Actuation in Ni-Mn-Ga Shape-Memory Alloys. *Advanced Materials* **2010**, *23*, 216–232.

[80] Gajbhiye, N.; Ningthoujam, R.; Weissmller, J. Synthesis and Magnetic Studies of Nanocrystalline Nickel Nitride Material. *physica status solidi (a)* **2002**, *189*, 691–695.

[81] Bartholomew, C. Chemistry of nickel-alumina catalysts. *Journal of Catalysis* **1976**, *45*, 41–53.

[82] Shalom, M.; Molinari, V.; Esposito, D.; Clavel, G.; Ressnig, D.; Giordano, C.; Antonietti, M. Sponge-like Nickel and Nickel Nitride Structures for Catalytic Applications. *Advanced Materials* **2013**, *26*, 1272–1276.

[83] Xu, K.; Chen, P.; Li, X.; Tong, Y.; Ding, H.; Wu, X.; Chu, W.; Peng, Z.; Wu, C.; Xie, Y. Metallic Nickel Nitride Nanosheets Realizing Enhanced Electrochemical

Water Oxidation. *Journal of the American Chemical Society* **2015**, *137*, 4119–4125.

[84] Gao, D.; Zhang, J.; Wang, T.; Xiao, W.; Tao, K.; Xue, D.; Ding, J. Metallic Ni_3N nanosheets with exposed active surface sites for efficient hydrogen evolution. *Journal of Materials Chemistry A* **2016**, *4*, 17363–17369.

[85] Winiarski, M. J. Band gap evolution of bulk Cu_3N and monolayer Cu_2N under nonhydrostatic strain. *Journal of Solid State Chemistry* **2018**, *266*, 161–165.

[86] Bocharov, D.; Anspoks, A.; Timoshenko, J.; Kalinko, A.; Krack, M.; Kuzmin, A. Interpretation of the Cu K-edge EXAFS spectra of Cu_3N using ab initio molecular dynamics. *Radiation Physics and Chemistry* **2020**, *175*, 108100–8.

[87] Zakutayev, A.; Caskey, C. M.; Fioretti, A. N.; Ginley, D. S.; Vidal, J.; Stevanovic, V.; Tea, E.; Lany, S. Defect Tolerant Semiconductors for Solar Energy Conversion. *Journal of Physical Chemistry Letters* **2014**, *5*, 1117–1125.

[88] Maruyama, T.; Morishita, T. Copper nitride and tin nitride thin films for write-once optical recording media. *Applied Physics Letters* **1996**, *69*, 890–891.

[89] Zhu, W.; Zhang, X.; Fu, X.; Zhou, Y.; Luo, S.; Wu, X. Resistive-switching behavior and mechanism in copper-nitride thin films prepared by DC magnetron sputtering. *physica status solidi (a)* **2012**, *209*, 1996–2001.

[90] Yin, Z.; Yu, C.; Zhao, Z.; Guo, X.; Shen, M.; Li, N.; Muzzio, M.; Li, J.; Liu, H.; Lin, H.; Yin, J.; Lu, G.; Su, D.; Sun, S. Cu_3N Nanocubes for Selective Electrochemical Reduction of CO_2 to Ethylene. *Nano Letters* **2019**, *19*, 8658–8663.

[91] Panda, C.; Menezes, P. W.; Zheng, M.; Orthmann, S.; Driess, M. In Situ Formation of Nanostructured Core–Shell Cu_3N–CuO to Promote Alkaline Water Electrolysis. *American Chemical Society Energy Letters* **2019**, *4*, 747–754.

[92] Xi, P. X.; Xu, Z. H.; Gao, D. Q.; Chen, F. J.; Xue, D. S.; Tao, C. L.; Chen, Z. N. Solvothermal synthesis of magnetic copper nitride nanocubes with highly elec-

trocatalytic reduction properties. *Royal Society of Chemistry Advances* **2014**, *4*, 14206–14209.

[93] Hahn, U.; Weber, W. Electronic structure and chemical-bonding mechanism of Cu_3N, Cui_3NPd, and related Cu(I) compounds. *Physical Review B* **1996**, *53*, 12684–12693.

[94] Gulo, F.; Simon, A.; Kohler, J.; Kremer, R. K. Li-Cu exchange in intercalated Cu_3N–with a remark on Cu_4N. *Angewandte Chemie International Edition* **2004**, *43*, 2032–4.

[95] Cui, X. Y.; Soon, A.; Phillips, A. E.; Zheng, R. K.; Liu, Z. W.; Delley, B.; Ringer, S. P.; Stampfl, C. First principles study of 3d transition metal dopedCu_3N. *Journal of Magnetism and Magnetic Materials* **2012**, *324*, 3138–3143.

[96] Choi, J.; Gillan, E. G. Solvothermal synthesis of nanocrystalline copper nitride from an energetically unstable copper azide precursor. *Inorganic Chemistry* **2005**, *44*, 7385–93.

[97] Zachwieja, U.; Jacobs, H. Ammonothermalsynthese von kupfernitrid, Cu_3N. *Journal of the Less Common Metals* **1990**, *161*, 175–184.

[98] Jacobs, H.; Zachwieja, U. Kupferpalladiumnitride, Cu_3Pd_xN mit x = 0,020 und 0,989, Perowskite mit "bindender $3d^{10}$-$4d^{10}$-Wechselwirkung". *Journal of the Less Common Metals* **1991**, *170*, 185–190.

[99] Juza, R.; Hahn, H. Kupfernitrid Metallamide und Metallnitride. VII. *Zeitschrift for anorganische und allgemeine Chemie* **1939**, *241*, 172–178.

[100] Paniconi, G.; Stoeva, Z.; Doberstein, H.; Smith, R. I.; Gallagher, B. L.; Gregory, D. H. Structural chemistry of Cu_3N powders obtained by ammonolysis reactions. *Solid State Sciences* **2007**, *9*, 907–913.

[101] Deshmukh, R.; Zeng, G. B.; Tervoort, E.; Staniuk, M.; Wood, D.; Niederberger, M. Ultrasmall Cu_3N Nanoparticles: Surfactant-Free Solution-Phase Synthesis, Nitri-

dation Mechanism, and Application for Lithium Storage. *Chemistry of Materials* **2015**, *27*, 8282–8288.

[102] Deshmukh, R.; Tervoort, E.; Kach, J.; Rechberger, F.; Niederberger, M. Assembly of ultrasmall Cu3N nanoparticles into three-dimensional porous monolithic aerogels. *Dalton Trans* **2016**, *45*, 11616–9.

[103] Liu, Y.; Lin, D.; Yuen, P. Y.; Liu, K.; Xie, J.; Dauskardt, R. H.; Cui, Y. An Artificial Solid Electrolyte Interphase with High Li-Ion Conductivity, Mechanical Strength, and Flexibility for Stable Lithium Metal Anodes. *Advanced Materials* **2017**, *29*, 1605531.

[104] Mondal, S.; Raj, C. R. Copper Nitride Nanostructure for the Electrocatalytic Reduction of Oxygen: Kinetics and Reaction Pathway. *Journal of Physical Chemistry C* **2018**, *122*, 18468–18475.

[105] Sithole, R. K.; Machogo, L. F. E.; Airo, M. A.; Gqoba, S. S.; Moloto, M. J.; Shumbula, P.; Van Wyk, J.; Moloto, N. Synthesis and characterization of Cu_3N nanoparticles using pyrrole-2-carbaldpropyliminato Cu(II) complex and $Cu(NO_3)_2$ as single-source precursors: the search for an ideal precursor. *New Journal of Chemistry* **2018**, *42*, 3042–3049.

[106] Livage, J.; Sanchez, C.; Henry, M.; Doeuff, S. The chemistry of the sol-gel process. *Solid State Ionics* **1989**, *32-33*, 633–638.

[107] Egeberg, A.; Warmuth, L.; Riegsinger, S.; Gerthsen, D.; Feldmann, C. Pyridine-based low-temperature synthesis of CoN, Ni_3N and Cu_3N nanoparticles. *Chemical Communications journal* **2018**, *54*, 9957–9960.

[108] Nakamura, T.; Hayashi, H.; Hanaoka, T. A.; Ebina, T. Preparation of copper nitride (Cu_3N) nanoparticles in long-chain alcohols at 130-200 degrees C and nitridation mechanism. *Inorganic Chemistry* **2014**, *53*, 710–5.

[109] Partin, D.; Williams, D.; O'Keeffe, M. The Crystal Structures of Mg_3N_2 and Zn_3N_2. *Journal of Solid State Chemistry* **1997**, *132*, 56–59.

[110] Coronel, N. C. Ph.D. thesis, California Institute of Technology, 2016.

[111] Yang, T.; Zhang, Z.; Li, Y.; Lv, M.; Song, S.; Wu, Z.; Yan, J.; Han, S. Structural and optical properties of zinc nitride films prepared by rf magnetron sputtering. *Applied Surface Science* **2009**, *255*, 3544–3547.

[112] Kuriyama, K.; Takahashi, Y.; Sunohara, F. Optical band gap of Zn_3N_2 films. *Physical Review B* **1993**, *48*, 2781–2782.

[113] Zong, F.; Ma, H.; Ma, J.; Du, W.; Zhang, X.; Xiao, H.; Ji, F.; Xue, C. Structural properties and photoluminescence of zinc nitride nanowires. *Applied Physics Letters* **2005**, *87*, 233104.

[114] Prabha, S.; Durgalakshmi, D.; Subramani, K.; Aruna, P.; Ganesan, S. Enhanced Emission of Zinc Nitride Colloidal Nanoparticles with Organic Dyes for Optical Sensors and Imaging Application. *ACS Applied Materials & Interfaces* **2020**, *12*, 19245–19257.

[115] Jayatissa, A. H.; Wen, T.; Gautam, M. Optical properties of zinc nitride films deposited by the rf magnetron sputtering method. *Journal of Physics D: Applied Physics* **2012**, *45*, 045402.

[116] Paniconi, G.; Stoeva, Z.; Smith, R. I.; Dippo, P. C.; Gallagher, B. L.; Gregory, D. H. Synthesis, stoichiometry and thermal stability of Zn_3N_2 powders prepared by ammonolysis reactions. *Journal of Solid State Chemistry* **2008**, *181*, 158–165.

[117] Zong, F.; Ma, H.; Xue, C.; Du, W.; Zhang, X.; Xiao, H.; Ma, J.; Ji, F. Structural properties of zinc nitride empty balls. *Materials Letters* **2006**, *60*, 905–908.

[118] Taylor, P. N.; Schreuder, M. A.; Smeeton, T. M.; Grundy, A. J. D.; Dimmock, J. A. R.; Hooper, S. E.; Heffernan, J.; Kauer, M. Synthesis of widely tunable and

highly luminescent zinc nitride nanocrystals. *J. Mater. Chem. C* **2014**, *2*, 4379–4382.

[119] Amano, H.; Sawaki, N.; Akasaki, I.; Toyoda, Y. Metalorganic vapor phase epitaxial growth of a high quality GaN film using an AlN buffer layer. *Applied Physics Letters* **1986**, *48*, 353–355.

[120] Kaur, M.; Singh, K.; Singh, P.; Kaur, A.; Meena, R.; Singh, G. P.; Barabadi, H.; Saravanan, M.; Kumar, A. Emerging aluminium nitride nanoparticles: chemical synthesis and exploration of their biocompatibility and anticancer activity against cervical cancer cells. *Nanomedicine Journal* **2020**, *7*, 221–225.

[121] Bian, Y.; Liu, M.; Ke, G.; Chen, Y.; DiBattista, J.; Chan, E.; Yang, Y. Aluminum nitride thin film growth and applications for heat dissipation. *Surface and Coatings Technology* **2015**, *267*, 65–69.

[122] Li, C.; Liu, X.; Shu, L.; Li, Y. AlN-based surface acoustic wave resonators for temperature sensing applications. *Materials Express* **2015**, *5*, 367–370.

[123] Li, C.; Liu, X.-Z.; Peng, B.; Shu, L.; Li, Y.-R. AlN-based surface acoustic wave resonators on platinum bottom electrodes for high-temperature sensing applications. *Rare Metals* **2016**, *35*, 408–411.

[124] Kudyakova, V.; Shishkin, R.; Elagin, A.; Baranov, M.; Beketov, A. Aluminium nitride cubic modifications synthesis methods and its features. Review. *Journal of the European Ceramic Society* **2017**, *37*, 1143–1156.

[125] Arizaga, G. G.; Oviedo, M. J.; Lopez, O. E. Electrical properties of polycrystalline GaN films functionalized with cysteine and stabilization of GaN nanoparticles in aqueous media. *Colloids Surf B Biointerfaces* **2012**, *98*, 63–71.

[126] Antoniammal, P.; Arivuoli, D. Size and Shape Dependence on Melting Temperature of Gallium Nitride Nanoparticles. *Journal of Nanomaterials* **2012**, *2012*, 1–11.

[127] Nakamura, S.; Fasol, G. *The Blue Laser Diode*; Springer Berlin Heidelberg, 1997; pp 313–315.

[128] Starikov, E.; Shiktorov, P.; Gružinskis, V.; Reggiani, L.; Varani, L.; Vaissière, J.; Zhao, J. H. Monte Carlo calculations of THz generation in wide gap semiconductors. *Physica B: Condensed Matter* **2002**, *314*, 171–175.

[129] Neff, H.; Semchinova, O.; Lima, A.; Filimonov, A.; Holzhueter, G. Photovoltaic properties and technological aspects of $In_1-xGaxN$/Si, Ge (0<x<0.6) heterojunction solar cells. *Solar Energy Materials and Solar Cells* **2006**, *90*, 982–997.

[130] Nguyen, H. P. T.; Chang, Y.-L.; Shih, I.; Mi, Z. InN p-i-n Nanowire Solar Cells on Si. *IEEE Journal of Selected Topics in Quantum Electronics* **2011**, *17*, 1062–1069.

[131] Wu, J. When group-III nitrides go infrared: New properties and perspectives. *Journal of Applied Physics* **2009**, *106*, 011101.

[132] Liu, Z. H.; Beaulac, R. Nature of the Infrared Transition of Colloidal Indium Nitride Nanocrystals: Nonparabolicity Effects on the Plasmonic Behavior of Doped Semiconductor Nanomaterials. *Chemistry of Materials* **2017**, *29*, 7507–7514.

[133] Liu, Z.; Janes, L. M.; Saniepay, M.; Beaulac, R. Charge Storage and Quantum Confinement Resilience in Colloidal Indium Nitride Nanocrystals. *Chemistry of Materials* **2018**, *30*, 5435–5443.

[134] Schwenzer, B.; Loeffler, L.; Seshadri, R.; Keller, S.; Lange, F. F.; DenBaars, S. P.; Mishra, U. K. Preparation of indium nitride micro- and nanostructures by ammonolysis of indium oxide. *Journal of Materials Chemistry* **2004**, *14*, 637.

[135] Sinha, G.; Panda, S. K.; Mishra, P.; Ganguli, D.; Chaudhuri, S. Gallium nitride quantum dots in a nitrogen-bonded silica gel matrix. *Journal of Physics-Condensed Matter* **2007**, *19*, 346209.

[136] Chen, Y.; Jyoti, N.; Kim, J. Strong deep-UV and visible luminescence from GaN nanoparticles. *Applied Physics A* **2010**, *102*, 517–519.

[137] Chen, Y.; Maniruzzaman, M.; Kim, J. Soft-chemistry based fabrication of gallium nitride nanoparticles. *International Journal of Precision Engineering and Manufacturing* **2011**, *12*, 573–576.

[138] Xiao, H.; Pei, H.; Liu, J.; Cui, J.; Jiang, B.; Hou, Q.; Hu, W. Fabrication, characterization, and photocatalysis of GaN–Ga_2O_3 core-shell nanoparticles. *Materials Letters* **2012**, *71*, 145–147.

[139] Yan, H.; Liu, K.; Luo, R.; Chen, S.; Cao, H. Synthesis of GaN nanoparticles from $NH_4[Ga(OH)_2CO_3]$ under a flow of ammonia gas. *Materials Letters* **2010**, *64*, 2109–2111.

[140] Li, P. G.; Lei, M.; Du, Y. X.; Guo, X.; Tang, W. H. Synthesis of N-deficient GaN nanoparticles and its enhanced dielectric response. *Applied Surface Science* **2009**, *255*, 3843–3847.

[141] Manz, A.; Birkner, A.; Kolbe, M.; Fischer, R. A. Solution Synthesis of Colloidal Gallium Nitride at Unprecedented Low Temperatures. *Advanced Materials* **2000**, *12*, 569–573.

[142] Grocholl, L.; Wang, J. J.; Gillan, E. G. Solvothermal azide decomposition route to GaN nanoparticles, nanorods, and faceted crystallites. *Chemistry of Materials* **2001**, *13*, 4290–4296.

[143] Kawamura, F.; Watanabe, K.; Takeda, T.; Taniguchi, T. Synthesis of high-crystallinity cubic-GaN nanoparticles using the Na flux method—A proposed new usage for a belt-type high-pressure apparatus. *Journal of Crystal Growth* **2011**, *321*, 100–105.

[144] Janik, J. F.; Wells, R. L. Gallium Imide, $Ga(NH)_{3/2n}$, a New Polymeric Precursor for Gallium Nitride Powders. *Chemistry of Materials* **1996**, *8*, 2708–2711.

[145] Micic, O. I.; Ahrenkiel, S. P.; Bertram, D.; Nozik, A. J. Synthesis, structure, and

optical properties of colloidal GaN quantum dots. *Applied Physics Letters* **1999**, *75*, 478–480.

[146] Gaiser, H. F.; Popescu, R.; Gerthsen, D.; Feldmann, C. Ionic-liquid-based synthesis of GaN nanoparticles. *Chemical Communications* **2020**, *56*, 2312–2315.

[147] Dingman, S. D.; Rath, N. P.; Markowitz, P. D.; Gibbons, P. C.; Buhro, W. E. Low-Temperature, Catalyzed Growth of Indium Nitride Fibers from Azido-Indium Precursors. *Angewandte Chemie International Edition* **2000**, *39*, 1470–1472.

[148] Choi, J.; Gillan, E. G. Low-temperature solvothermal synthesis of nanocrystalline indium nitride and Ga–In–N composites from the decomposition of metal azides. *J. Mater. Chem.* **2006**, *16*, 3774–3784.

[149] Purdy, A. P. Indium(III) amides and nitrides. *Inorganic Chemistry* **1994**, *33*, 282–286.

[150] Wu, C.; Li, T.; Lei, L.; Hu, S.; Liu, Y.; Xie, Y. Indium nitride from indium iodide at low temperatures: synthesis and their optical properties. *New Journal of Chemistry* **2005**, *29*, 1610.

[151] Hsieh, J. C.; Yun, D. S.; Hu, E.; Belcher, A. M. Ambient pressure, low-temperature synthesis and characterization of colloidal InN nanocrystals. *Journal of Materials Chemistry* **2010**, *20*, 1435.

[152] Palomaki, P. K.; Miller, E. M.; Neale, N. R. Control of plasmonic and interband transitions in colloidal indium nitride nanocrystals. *J Am Chem Soc* **2013**, *135*, 14142–50.

[153] Wang, L.; Shen, Q.; Zhao, D.; Lu, J.; Liu, W.; Zhang, J.; Bao, K.; Zhou, Q. Chemical synthesis of hexagonal indium nitride nanocrystallines at low temperature. *Journal of Crystal Growth* **2017**, *471*, 62–65.

[154] Karan, N. S.; Chen, Y.; Liu, Z.; Beaulac, R. Solution–Liquid–Solid Approach to Colloidal Indium Nitride Nanoparticles from Simple Alkylamide Precursors. *Chemistry of Materials* **2016**, *28*, 5601–5605.

[155] Chen, Y.; Landes, N. T.; Little, D. J.; Beaulac, R. Conversion Mechanism of Soluble Alkylamide Precursors for the Synthesis of Colloidal Nitride Nanomaterials. *Journal of the American Chemical Society* **2018**, *140*, 10421–10424.

[156] Sardar, K.; Dan, M.; Schwenzer, B.; Rao, C. N. R. A simple single-source precursor route to the nanostructures of AlN, GaN and InN. *Journal of Materials Chemistry* **2005**, *15*, 2175–2177.

[157] Chitara, B.; Late, D. J.; Krupanidhi, S. B.; Rao, C. N. R. Room-temperature gas sensors based on gallium nitride nanoparticles. *Solid State Communications* **2010**, *150*, 2053–2056.

[158] Choi, Y. C.; Kim, H.; Lee, C.; Son, J.; Baik, H.; Park, S.; Kim, J.; Jeong, K. S. Blue Emission of α-GaN Colloidal Quantum Dots via Zn Doping. *Chemistry of Materials* **2019**, *31*, 5370–5375.

[159] Holder, C. F.; Schaak, R. E. Tutorial on Powder X-ray Diffraction for Characterizing Nanoscale Materials. *American Chemical Society Nano* **2019**, *13*, 7359–7365.

[160] De Roo, J.; Yazdani, N.; Drijvers, E.; Lauria, A.; Maes, J.; Owen, J. S.; Van Driessche, I.; Niederberger, M.; Wood, V.; Martins, J. C.; Infante, I.; Hens, Z. Probing Solvent–Ligand Interactions in Colloidal Nanocrystals by the NMR Line Broadening. *Chemistry of Materials* **2018**, *30*, 5485–5492.

[161] Parvizian, M.; Bechter, J.; Huber, J.; Chettata, N.; Roo, J. D. An Experimental Introduction to Colloidal Nanocrystals through InP and InP/ZnS Quantum Dots. *Journal of Chemical Education* **2023**, *100*, 1613–1620.

In science, there are no shortcuts to truth, and it is not enough to have an opinion; you must provide evidence.

Carl Sagan

2 The Chemistry of Cu_3N and Cu_3PdN Nanocrystals

2.1 Introduction

Copper nitride (Cu_3N) has garnered attention as an inexpensive, non-toxic material with potential applications in solar cells[1], high-density optical data storage[2], and electrocatalysis (oxygen evolution and CO_2 reduction)[3–5]. Cu_3N is a semiconductor with a calculated indirect bandgap of 1 eV and an anti-ReO_3 cubic crystal structure.[1;6;7] The body center position can be occupied by dopants (e.g., palladium) forming structures such as Cu_3Pd_xN. Upon doping, the lattice constant increases,[8;9] and the electronic structure of the material is reported to change from semiconducting to semi-metallic.[10;11] Bulk Cu_3N forms at relatively low temperatures but decomposes at higher temperatures (475 °C) to metallic copper (under an inert atmosphere) or copper oxide (in the air).[2;12] The first wet-chemical synthesis of bulk Cu_3N powders was based on aminolysis or the

[‡]**Adapted from**: Parvizian, M. Duran Balsa, A.; Pokratath, R.; Kalha, C.; Lee, S.; Van den Eynden, D.; Ibanez, M.; Regoutz, A. ; De Roo, J.; The Chemistry of Cu_3N and Cu_3PdN Nanocrystals; *Angew Chem Int Ed Engl*, **2022**, 61, 1521-3773
Contributions: Parvizian, M. conducted the synthesis and characterization using XRD, DLS, UV-Vis, and NMR techniques and analyzed the provided data. This project was substantially carried out during the timeframe of Duran Balsa, A.'s master's thesis, with Parvizian, M. overseeing the process. Pokratath, R. handled the PDF and TGA analyses. Kalha, C. conducted advanced XPS analysis under the supervision of Regoutz, A. Lee, S., and Van den Eynden, D. performed TEM measurements.

solvothermal decomposition of copper azides.[12–14] Ultra-small (2–4 nm) and colloidally stable nanocrystals (NCs) of Cu_3N have been synthesized from $Cu(OMe)_2$ in benzylamine,[15] or by aminolysis of Cu(I) in pyridine.[16] Larger colloidal Cu_3N nanocubes have been obtained from copper(II) nitrate and alkylamine, see equation 2.1.[3;5;17–21] In most cases, additional solvent is added (usually 1-octadecene (ODE)). The equivalents of ligand (32–66), the reaction temperature (220–280 °C), and time (10–60 min) vary, as does the nature of the alkyl chain of the amine (oleylamine (OLAm), hexadecylamine or octadecylamine (ODA)). Changing the nature of the amine allows tuning the final size from 10 to 25 nm (Figure 2.1).[17]

$$Cu(NO_3)_2 \cdot 3\,H_2O + 32{-}66\ RNH_2 \xrightarrow[ODE]{220\text{-}280\,^\circ C,10\text{-}60\ min} 1/_3\,Cu_3N + by{-}products \qquad (2.1)$$

An overview of the reported Cu_3N synthesis conditions and outcomes are condensed into table 2.1.

Unfortunately, the reaction mechanism and the by-products are not well established. Some authors claim that nitrate is the nitrogen source, and thus nitrogen is supposed to be reduced from its highest oxidation state in nitrate to its lowest oxidation state in nitride, and this process is presumably catalyzed by the amine ligand.[19] Such an eight-electron redox process is unlikely to happen in a single reaction. Other authors assume that Cu(II) is first fully reduced to Cu(0) and subsequently reacts with dinitrogen (a possible decomposition product of the nitrate complex).[21] However, the nitrogen-nitrogen bond in dinitrogen is extremely strong (946 kJ/mol),[26] and N_2 is thus not likely to react with elemental copper at 250 °C. There is currently insufficient evidence to claim a mechanism for the precursor conversion. Regarding the crystallization mechanism, it was shown that first small, amorphous particles form, which subsequently ripen into Cu_3N nanocubes.[5] The growth mechanism was investigated by analyzing reaction aliquots at 2, 5 and 10 min by TEM (Figure 2.2). In addition, long reaction times (at 260 °C) wash shown to lead to the decomposition of the as-synthesized Cu_3N into Cu(0) particles.[21]

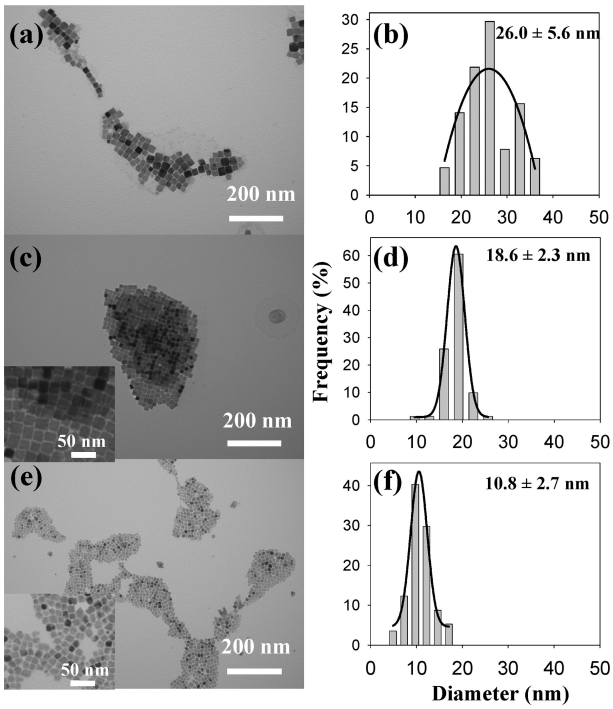

Figure 2.1 TEM images and the corresponding size histograms of Cu_3N NCs synthesized from copper(II) nitrate and various primary amines in ODE solvent, according to reference[17]. (a,b) ODA (c,d) hexadecylamine, and (e,f) OLAm. Reprinted with permission from ref[17]. Copyright 2011 American Chemical Society. Note that the authors labeled the axis *diameter*. Given the cubic morphology of the NCs, this is confusing and the cube edge length is a more appropriate measure for the size.

Table 2.1 | Synthetic conditions for colloidal Cu_3N NCs

Precursor[a]	[Cu] (mM)	Solvent[b]/ ligand[c]	Ligand/Cu ratio	Temperature (°C)	Time (min)	Morphology	Phase	Size (nm)	Ref.
$Cu(NO_3)_2.3H_2O$	101	ODA	32	240	10	cubic	Cu_3N	15	[19]
$Cu(NO_3)_2.3H_2O$	101	ODA	32	280	5	spherical	Cu_3N	10	[19]
$Cu(NO_3)_2.3H_2O$	101	ODA	32	260 + 240	5 + 5	spherical	Cu_3N	15	[19]
$Cu(NO_3)_2.3H_2O$	101	ODA	32	220 + 240	5 + 5	spherical	Cu_3N	15	[19]
$Cu(NO_3)_2.3H_2O$	101	ODA	32	220	20	irregular	Cu_3N	50	[19]
$Cu(NO_3)_2.3H_2O$		ODA	40	240	10		Cu + Cu_3N		[19]
$Cu(NO_3)_2.3H_2O$		ODA	13	240	10		CuO + Cu_3N		[19]
$Cu(NO_3)_2.3H_2O$	24	ODE / ODA	67	250	30	cubic	Cu_3N	26	[17]
$Cu(NO_3)_2.3H_2O$	24	ODE / HDA	69	250	30	cubic	Cu_3N	19	[17]
$Cu(NO_3)_2.3H_2O$	24	ODE / OLAm	63	250	30	cubic	Cu_3N	11	[17]
$Cu(NO_3)_2.3H_2O$	24	OLAm		250	30	irregular	Cu_3N		[17]
$Cu(NO_3)_2.3H_2O$	25	ODE / OLAm	31	240	15	cubic	Cu_3N		[18]
$Cu(NO_3)_2.3H_2O$+ $Pd(acac)_2$	25	ODE / OLAm	31	240	15	cubic	Cu_3PdN	16	[18]
$Cu(NO_3)_2.3H_2O$ + $Pd(acac)_2$	25	ODE / OLAm	31	190	30	cubic	Cu_3PdN		[22]
$Cu(NO_3)_2.3H_2O$	25	ODE / OLAm	31	210	30	cubic	Cu_3N		[22]
$Cu(NO_3)_2.3H_2O$	75	ODA / OLAm	45	240	20	cubic	Cu_3N	25	[5]
$Cu(NO_3)_2.3H_2O$	88	ODA / OLAm	41	240	30	cubic	Cu_3N	25	[3]
$Cu(NO_3)_2.3H_2O$	88	ODA / OLAm	41	250	30	cubic	Cu_3N	20	[3]
$Cu(NO_3)_2.3H_2O$	88	ODA / OLAm	41	260	30	cubic	Cu_3N	10	[3]
$Cu(NO_3)_2.3H_2O$	88	ODA / OLAm	41	230	30	spherical	Cu_3N	20	[3]
$Cu(NO_3)_2.5H_2O$ + HMT	50	hexanol	-	200	60	spherical	Cu_3N	80	[23]
$Cu(acetate)_2 \cdot H_2O$ + NH_3	10	nonanol	-	190	60	spherical	Cu_3N	200	[24]
PPC	50	ODA	74	260	5	spherical	Cu_3N	3	[25]
$Cu(NO_3)_2.3H_2O$	50	ODA	74	260	5	cubic	Cu_3N	19	[25]
$Cu(OMe)_2$	92	$BnNH_2$	117	140	15	spherical	Cu_3N	2	[15]
CuI + KNH_2 + NH_3	21	pyridine	-	-35 + 130	10 + 30	spherical	Cu_3N	4	[16]

[a] HMT = hexamethylenetetraamine, PPC = pyrrole-2-carbaldpropyliminato Cu(II); [b] ODE = 1-ODE; [c] ODA = Octadecylamine, OLAm = oleylamine, HDA = hexadecylamine

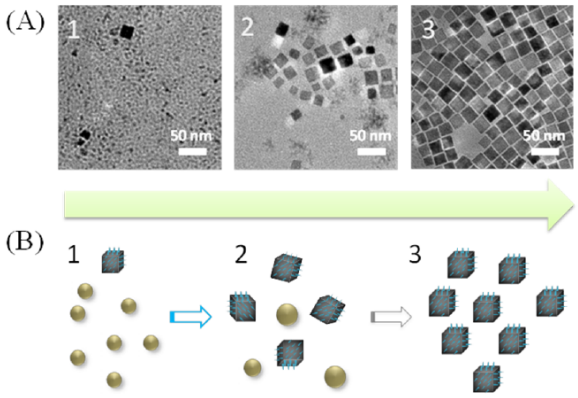

Figure 2.2 (A) TEM of the Cu_3N NCs synthesized according to reference[5], after 2, 5 and 10 min. (B) The proposed growth procedure of Cu_3N nanocubes. Reproduced from reference[5] with permission from the Royal Society of Chemistry.

The surface chemistry of Cu_3N NCs is also unknown. Although alkylamines are the only ligands present during the synthesis, there are several examples where the ligands can convert to other ligands during NCs synthesis, leading to surprising surface chemistries.[27;28] Given the importance of surface chemistry for nanocrystal applications it is imperative to elucidate and control it.[29] Amines typically bind to the nanocrystal surface as Lewis basic (L-type) ligands and feature an adsorption-desorption equilibrium that is often highly dynamic.[30–32] However, in the case of copper based NCs, amines have been observed to be tightly bound.[33;34] It is thus surprising that Cu_3N NCs have generally poor colloidal stability after purification.

In this work, we aimed at elucidating the precursor conversion mechanism and surface chemistry of Cu_3N (and Cu_3PdN) NCs, synthesized from copper(II) nitrate (and palladium acetylacetonate). We first screened the different synthetic methods in the literature, and found the report of Vaughn *et al.* as the most reproducible. We then explored the influence of different parameters on the reaction outcome, including the presence of water, temperature, time, etc. Having obtained the optimal conditions to form phase pure Cu_3N nanocubes, we then redesigned the purification procedure to yield colloidally stable Cu_3N NCs. We uncovered the precursor conversion mechanism

of the reaction. We found that nitrate and Cu(II) both oxidize alkylamine to a primary aldimine, forming Cu(I). Condensation of the primary aldimine with a second equivalent alkylamine, yields a secondary aldimine and ammonia. The latter is the active nitrogen precursor and reacts with Cu(I) to Cu_3N. Finally, the surface of these Cu_3N and Cu_3PdN particles has been analyzed. x-ray photoelectron spectroscopy (XPS) and fourier-transform infrared spectroscopy (FT-IR) established the presence of carboxylate ligands on the surface, together with amine ligands. Advanced nuclear magnetic resonance (NMR) revealed the dynamics of ligands binding. These fundamental chemistry insights will enable the elucidation of formation mechanisms of other copper-based colloidal NCs and other metal nitrides.

2.2 Experimental section

Materials

For the standard Cu_3N and copper palladium doped nitride nanoparticles (NPs), copper(II) nitrate ($Cu(NO_3)_2.3H_2O$, STREM Chemicals, 99.5 %) and distilled OLAm ($C_{18}H_{35}NH_2$, Sigma-Adrich, 70 %) were used as precursors in hexadecane ($C_{16}H_{34}$, Sigma Aldrich 99 %). Palladium(II) 2,4- pentadionate ($C_{10}H_{14}O_4Pd$, Alfa Aesar, Pd 34.7 %) was used for doping. For the mechanistic investigations, various precursors were used: copper chloride ($CuCl_2 \cdot 2\,H_2O$, Sigma-Adrich, $\geq$ 99.0 %), dioctylamine ($CH_3(CH_2)_7NH{-}(CH_2)_7CH_3$), Sigma-Aldrich, 97 %), trioctylamine (($(CH_3(CH_2)_7)_3N$, Sigma-Aldrich, 98 %). For the aldimine synthesis, lauric aldehyde ($CH_3(CH_2)_{10}CHO$, Sigma-Aldrich, $\geq$ 95 %) was used. Cyclohexane, absolute ethanol, and acetone were used for the purification step. Deuterated chloroform ($CDCl_3$, 98 %) was used for NMR study.

Synthesis of Cu_3N

The synthesis for Cu_3N NCs was adapted from the literature.[18] Copper(II) nitrate (0.24 mmol, 60 mg, 1 eq) was dissolved in 7.5 mL of hexadecane in a three-neck flask and

stirred. Distilled OLAm (7.57 mmol, 2.5 mL, 31 eq) was added and the mixture was degassed for 30 minutes at 50 °C. Under argon, the temperature was increased to 260 °C at a rate of 10 °C per minute. The mixture was left to react for 15 minutes. The flask was then removed from the heating mantle and left to cool to room temperature over an hour. The 10 mL solution of NPs was transferred to centrifuge tubes. A total of 15 mL of acetone was added and the particles were centrifuged at 5'000 rpm for 3 minutes. The supernatant was removed and the particles were redispersed in 4 mL of cyclohexane. A 10% by volume stock solution (SS) of purified OLAm in cyclohexane was prepared. OLAm (1 mL SS) was added to the redispersed particles, so the total redispersion volume was 5 mL. The particles were placed in the ultrasonic bath until fully redispersed. The particles were washed once more with acetone (15 mL) and this time redispersed in 3 mL of cyclohexane. 2 mL of the OLAm SS was added, so the volume was still 5 mL. The particles were placed in the ultrasonic bath. 15 mL of ethanol was added for a final wash and the particles were centrifuged at 8'000 rpm for 10 minutes. The supernatant was removed, and the particles were redispersed in 2 mL of cyclohexane.

Synthesis of Cu_3PdN

The synthesis for Cu_3PdN NCs was adapted from the literature.[18] Copper(II) nitrate (0.24 mmol, 60 mg, 1 eq) was dissolved in 7.5 mL of hexadecane in a three-neck flask and stirred. Palladium(II) 2,4- pentadionate (0.08 mmol, 25.2 mg, 0.33 eq) was added and stirred. Distilled OLAm (7.57 mmol, 2.5 mL, 31 eq) was added and the mixture was degassed for 30 minutes at 50 °C. Under argon, the temperature was increased to 240 °C at a rate of 10 °C per minute. The mixture was left to react for 15 minutes. The flask was removed from the heating mantle and left to cool to room temperature over an hour. The NCs were purified as described previously. However, contrary to the Cu_3N NPs, the final centrifugation after the ethanol wash required 10–15 minutes at 10'000 rpm to precipitate the NPs.

Synchrotron X-ray total scattering experiments

Samples were prepared in 1mm polyamide kapton tube. The samples were measured at beamline P21.1 at DESY in Hamburg, Germany. X-ray total scattering data were collected at room temperature in rapid acquisition mode, using a Perkin Elmer digital X-ray flat panel amorphous silicon detector (2048 × 2048 pixels and 200 × 200 μm pixel size) with a sample-to-detector distance of 380 mm. The incident wavelength of the X-rays was $\lambda = 0.1220$Å (101.62 keV). Calibration of the experimental setup was performed using a Ni standard. Raw 2D data were corrected for geometrical effects and polarization, then azimuthally integrated to produce 1D scattering intensities versus the magnitude of the momentum transfer Q (where Q = $4\pi \sin \theta/\lambda$ for elastic scattering) using pyFAI and xpdtools.[35;36] The program xPDFsuite with PDFgetX3 was used to perform the background subtraction, further corrections, and normalization to obtain the reduced total scattering structure function F(Q), and Fourier transformation to obtain the x-ray total scattering and pair distribution function analysis (PDF), G*(r)*.[37;38] For data reduction, the following parameters were used after proper background subtraction: Qmin = 0.8Å^{-1}, Qmax = 19Å^{-1}, Rpoly = 0.9Å . Modeling and fitting were carried out using Diffpy-CMI or PDFgui.[39;40]

XPS and DFT

XPS measurements were performed on a Thermo Scientific K-Alpha spectrometer with a monochromated microfocused Al $K\alpha$ X-ray source (hν = 1486.7 eV) and a spot size of 400 μm. The X-ray source was operated at 6 mA emission current and 12 kV anode bias and a flood gun was used for charge compensation. A pass energy of 20 eV was used for all core level and valence spectra. The Thermo Scientific Avantage software package was used for all data analysis. All XPS core level spectra were normalized to the peak height of the main feature in the Cu $2P_{2/3}$ spectra. The details of the density functional theory (DFT) calculations for Cu_3N, including the density of states, have been previously reported.[1;41–43] To enable the direct comparison of the theory with the

experimental valence spectra, the calculated projected density of states (PDOS) was broadened with a Gaussian to match the experimental broadening of 600 meV. The PDOS was weighted by one-electron photoionization cross sections for the respective orbitals of Cu and N using the Galore software package, based on Scofield cross-section values.[44–46]

NMR measurments

NMR measurements were recorded at 298K on a Bruker UltraShield 500 MHz spectrometer or a 600 MHz Bruker Avance III spectrometer. Regular ^{1}H NMR measurements were acquired with a 30 degree pulse with a recycle delay of 1.5 sec. Quantitative ^{1}H NMR measurements were acquired with a 90 degree pulse, 64k data points, 20 ppm spectral width, and a recycle delay of 30 sec. Diffusion ordered spectroscopy (DOSY) measurements were performed with a double stimulated echo and bipolar gradient pulses (dstebpgp2s). The gradient strength was varied quadratically from 2–95% of the probe's maximum value in 16 or 64 steps. The gradient pulse duration and diffusion delay were optimized to ensure a final attenuation of the signal in the final increment of less than 10% relative to the first increment. The diffusion coefficients were obtained by fitting a modified Stejskal-Tanner equation to the signal intensity decay:

$$I = I_0 e^{-(\gamma \delta g)^2 D(\Delta - 0.6\delta)}$$

I are the signal intensities, D is the linear diffusion coefficients, γ is the gyromagnetic ratio of the studied nucleus, g is the gradient strength, δ is the pulsed field gradient duration, and Δ is the diffusion delay. A correction factor of 0.6 is applied for δ due to the smoothed squared pulse shape used for the gradient pulses.[47]

Other instrumentation

TEM imaging was done using a JEOL JEM2800 field emission gun microscope operated at 200 kV equipped with a TVIPS XF416ES TEM camera. Dynamic light scattering

(DLS) measurements were conducted on a Malvern Zetasizer Ultra in backscattering mode (173 °) in a glass cuvette. All measurements were performed at 25 °C after equilibrating inside the system for 240 seconds, sample concentration was tuned to achieve system attenuator values between 9–10. UV-Vis spectra were recorded on a PerkinElmer Lambda 365. FT-IR spectra were recorded on a Perkin Elmer Spectrum Two spectrometer (attenuated total reflection, ATR).

2.3 Results and discussion

2.3.1 Synthesis optimization

We decided to optimize the procedure reported by Vaughn *et al.* by exploring the influence of different parameters.[18] First, we replaced ODE (the solvent) with hexadecane since we reported earlier that ODE polymerizes at 240 °C, contaminating the final nanocrystal product and complicating the purification.[48] Concerning reaction temperature, crystalline Cu_3N was formed between 220 °C and 260 °C (after 15 minutes), with the highest crystallinity for 260 °C (Figure 2.3). Interestingly, the crystallite size was found to be quite independent of the reaction temperature; 10–11 nm according to the Scherrer analysis of the x-ray powder diffraction (*p*XRD) reflections. At 200 °C, no particles could be isolated.

Furthermore, we took reaction aliquots at 5, 10, 15, 30, and 60 min at 240 °C and 260 °C. Each aliquot was purified and analyzed by TEM to observe the nanocrystal growth throughout the reaction. At 240 °C, we observed both small dots and fully formed nanocubes up to 15 min of reaction time (Figures 2.4). The small particles presumably ripen in the bigger nanocubes since the former disappear at 30 min. After 60 minutes at 240 °C, the *p*XRD showed pure Cu_3N. By comparison, at 260 °C, the nanocubes were already fully formed after 15 min. After 30 min at 260 °C, the particles started to decompose and crystalline Cu(0) was formed. Some Cu_2O could also be detected as a minority phase after full decomposition. (Figure 2.5).

The reported procedure has two steps where a vacuum is applied. This leads us to

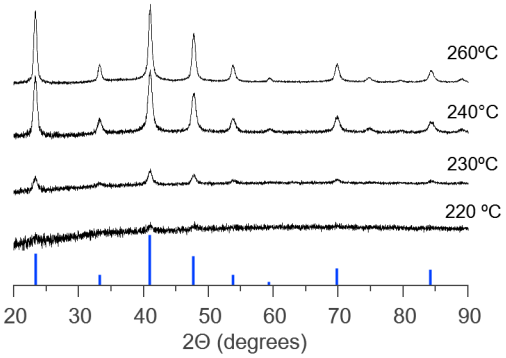

Figure 2.3 Powder *p*XRD of Cu_3N was obtained after 15 min at the different reaction temperatures. Bulk Cu_3N diffractogram is presented in blue.

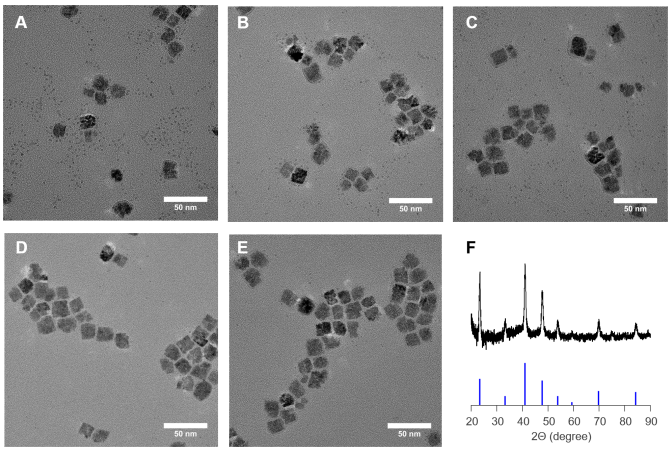

Figure 2.4 TEM images from aliquots at 5(A), 10 (B), 15 (C), 30 (D) and 60 (E) min at 240 °C. The *p*XRD of the final phase is shown corresponding to pure Cu_3N. No decomposition is observed even after 60 min.

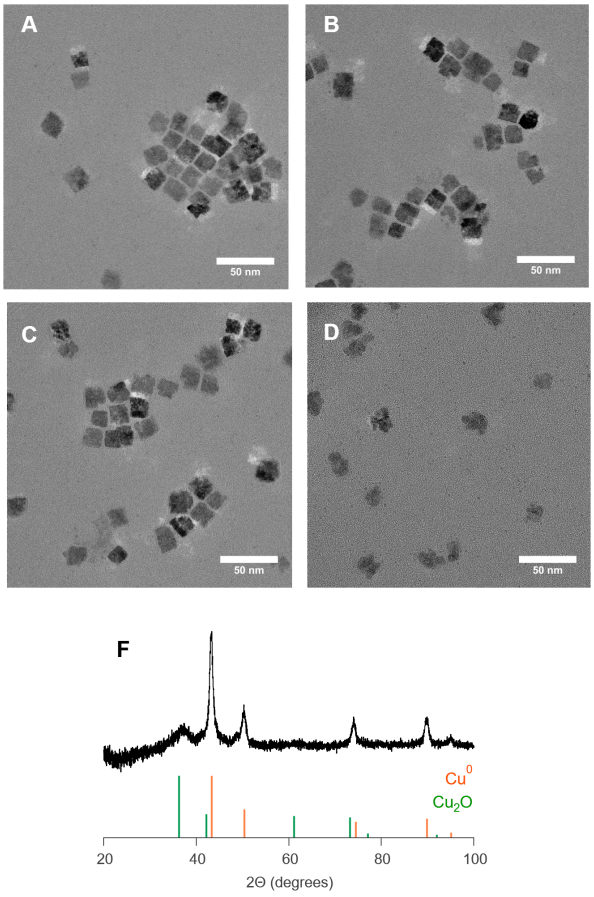

Figure 2.5 TEM images from aliquots at 5(A), 10 (B), 15 (C), and 30 (D) min at 260 °C. The *p*XRD of the final decomposed phase is shown corresponding to Cu^0.

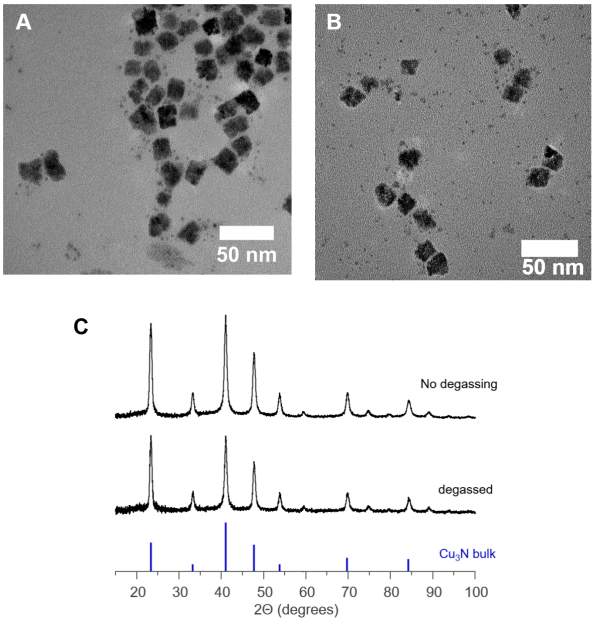

Figure 2.6 TEM images from the Cu_3N NCs obtained via a reaction with degassing (A) and without degassing (B). *p*XRD of the Cu_3N NCs obtained via a reaction with degassing and without degassing compared with the bulk (D). Note, that these reactions were not performed with the optimized procedure.

investigate the role of water and whether an inert atmosphere is strictly necessary. Note that the precursor contains water (an equivalent of 13 μL for a standard synthesis). We obtained identical Cu_3N NCs when the vacuum steps were omitted, or, when after applying vacuum (presumably removing water), 13 μL of water was injected into the reaction mixture (Figures 2.6). However, the same reaction in an open flask did not yield Cu_3N (or any isolatable material), indicating that an important gaseous intermediate can escape from the reaction mixture. To work under controlled and reproducible conditions, we still choose to perform a short (30 min) degassing step at 50 °C, but it appears that the synthesis is robust against air or water contamination.

We also found that both 30 and 60 equivalents of amine ligands yielded Cu_3N NCs (Figure 2.7).

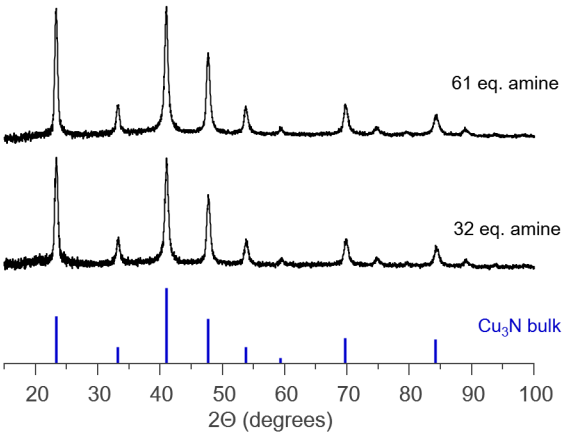

Figure 2.7 | *p*XRD of the Cu_3N NCs obtained with 32 and 61 equivalents of OLAm compared with the bulk.

Based on the above optimization, we arrived at the conditions in 2.2.

$$Cu(NO_3)_2 \cdot 3\,H_2O + 32\ RNH_2 \xrightarrow[\text{hexadecane}]{260\,^\circ C,15\ \text{min}} 1/_3\,Cu_3N + \text{by}-\text{products} \qquad (2.2)$$

2.3.2 Colloidal stability

After applying the reported precipitation-and-redispersion cycles (with ethanol and toluene)[18], the particles were redispersed in toluene (5 mL), but they precipitated within a couple of minutes, see Figure 2.8. Since the NCs were colloidally stable in the crude reaction mixture, we hypothesized that the ligands desorbed from the surface during the precipitation-and-redispersion cycles. The nature and volume of the solvent used for redispersion play an important role since they determine the position of the adsorption-desorption equilibrium. The ligand-solvent interaction should be favorable enough to disperse the NCs, but not so high that ligands prefer to be fully solvated over being bound to the surface.[49] During purification, it is also preferred to work with quite concentrated dispersions to minimize the loss of NCs over several cycles. On the other hand, too high concentrations might cause impurities to be trapped between the flocculating NCs. Considering the above points, we adapted the purification procedure. Various solvents (toluene, hexane, chloroform, and cyclohexane), as well as non-solvents (acetone,

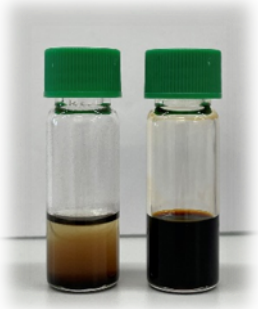

Figure 2.8 Photograph of Cu_3N NCs after regular (left) and optimized (right) purification.

ethanol, and methanol), were tested.

Our final procedure involves two precipitation cycles with acetone (15 mL) followed by final precipitation with ethanol (15 mL), always redispersing in cyclohexane (5 mL).[50] A 10 v% solution of distilled OLAm was added after the first acetone wash (1 mL) and after the second acetone wash (2 mL) followed by 5 minutes of sonication. There was no need for a final OLAm addition after the ethanol wash and the NCs remained colloidally stable. This procedure thus minimized the amount of excess ligand in the final product but provided a stable dispersion (11 mg/mL) of OLAm capped Cu_3N NCs, see Figure 2.8. Our samples were then analyzed by thermogravimetric analysis (TGA) in order to quantify the amount of ligand present. Since Cu_3N is being fully decomposed to Cu^0 at the end of the thermal process, the nitrogen loss should also be taken into account. We believe that the two first decomposition steps belong to the organics while the last decomposition starting at 356 °C belongs to Cu_3N decomposition (bulk Cu_3N decomposes around 400 °C). When starting with Cu_3N + organics, we recover, 65.9% of the mass as Cu^0 at 800 °C. Given the molar mass of Cu_3N (204.5 Da) and the molar mass of 3 copper atoms (190.5 Da), the 65.9% in Cu material corresponds to a theoretical amount of Cu_3N as

$$\frac{65.9\% \times 204.5}{190.5} = 70.7\%$$

We thus determined that the dried samples contained 29.2 w% organics (ligands) and

the final Cu_3N yield is 96 % (Figure 2.9).

Copper palladium nitride (Cu_3PdN) NCs were also synthesized. The procedure was identical to that of Cu_3N, except for the reaction temperature (240 °C) and the addition of 0.33 equivalents of Palladium(II) 2,4- pentadionate alongside the $Cu(NO_3)_2$. The doped NCs were purified with the optimized purification method. The synthesis yielded black NPs that were colloidally stable (13 mg/ mL). According to TGA, at the end of the heating process, the end product is Cu^0 and Pd^0 in a 3:1 ratio. The final mass was 86 % percent at 800 °C. Taking into account the molar mass of Cu_3PdN (310.9 Da) and that of 3 copper and 1 palladium atom (296.9 Da), we can calculate that the 86% composition of Cu and Pd corresponds to a theoretical amount of Cu_3PdN as:

$$\frac{86\% \times 310.9}{296.95} = 90\%$$

Additionally, assuming perfect Cu_3PdN stoichiometry, the ligands make up 13.22 wt% of the dried mass. The yield of Cu_3PdN is 91% (Figure 2.9).

2.3.3 Structural analysis

The final dispersions of Cu_3N and Cu_3PdN NCs were analyzed with TEM, *p*XRD and DLS (Figure 2.10). According to TEM, the average cube edge length is 13.5 nm (σ = 1.9 nm) for the Cu_3N nanocubes and 10.2 nm (σ = 1.4 nm) for the Cu_3PdN NCs. The solvodynamic diameter obtained from DLS analyses were 17 nm for Cu_3N and 13 nm for Cu_3PdN. The sizes obtained via DLS are in line with the sizes obtained via TEM since DLS determines the solvodynamic size of the whole particle, including the surface ligands. Both TEM and DLS support that the dispersions are highly stable since no aggregates are observed. *p*XRD shows quite sharp reflections for Cu_3N (crystallite size = 9.0±1.7 nm), while they are broader for Cu_3PdN (crystallite size = 4.5±1.1 nm). Compared with the sizes obtained from TEM, it is clear that the Cu_3PdN NCs are polycrystalline. A real space refinement of the x-ray total scattering and pair distribution function analysis (PDF) further confirms the structure of Cu_3N and Cu_3PdN (Figure

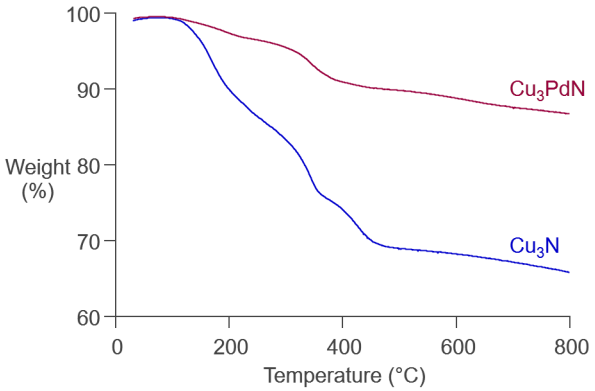

Figure 2.9 TGA plot of as-synthesized Cu_3N and Cu_3PdN. In the case of Cu_3N, three distinct decompositions are observed from 116 °C to 242 °C, 242 °C to 356 °C, and 356 °C to 456 °C followed by a semi-plateau until 800 °C. The end product at 800 °C is Cu^0 as judged by the rose gold color and reported literature. In the case of Cu_3PdN, only two decomposition steps can be recognized between 110 °C to 276 °C and 276 °C to 462 °C to finally reach a semi-plateau at 800 °C. We believe that the end products are Cu^0 and Pd.

A.1).

2.3.4 Precursor conversion mechanism

Regarding the precursor conversion mechanism, we found the proposed pathways in literature implausible and therefore proposed an alternative hypothesis in which the active nitride source is ammonia, see Figure 2.11. First, OLAm is oxidized to a primary aldimine by nitrate. Nucleophilic addition of a second equivalent of OLAm forms the more stable, secondary aldimine with the elimination of ammonia. Ammonia reacts with Cu(I) to Cu_3N. The Cu(I) species was generated by the reduction of Cu(II) by OLAm upon heating. Cyclic voltammetry confirms a lower reduction potential of Cu(II) to Cu(I) upon the addition of OLAm (at room temperature).[51] We hypothesize that the co-product of this Cu(II) reduction is the same primary aldimine as mentioned before.

The copper precursor, $Cu(NO_3)_2.3H_2O$, does not dissolve in the solvent (hexadecane) until OLAm is added, indicating the formation of a coordination complex. This is

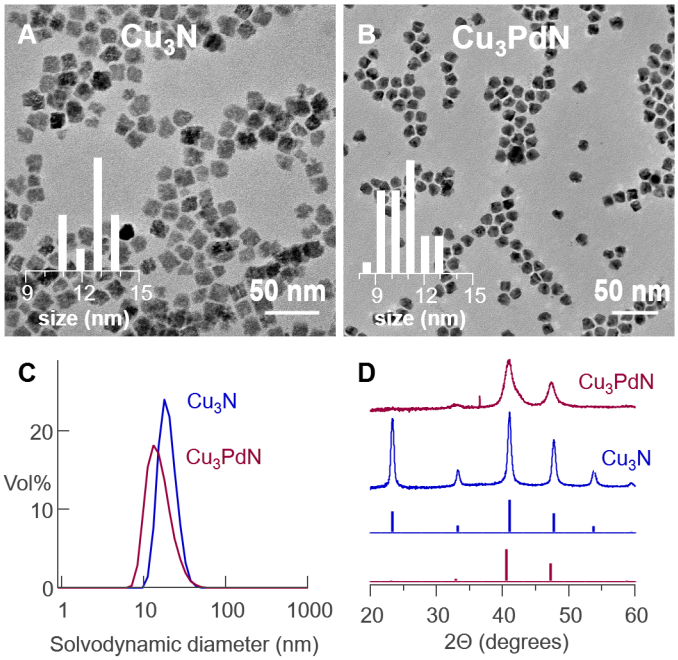

Figure 2.10 TEM images of (A) Cu_3N and (B) Cu_3PdN. The histograms are shown as an inset. The cube edge length is used as a measure of size. (C) DLS and (D) *p*XRD measurements (the reference *p*XRD reflections are shown as well)

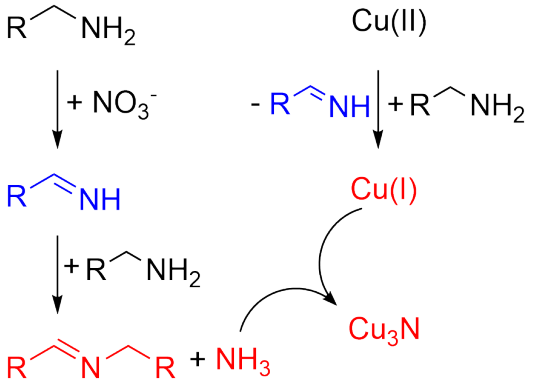

Figure 2.11 Our proposed pathway for Cu_3N formation. Precursors are shown in black, detected species in red, and hypothesized intermediates in blue

supported by the deep blue color of the reaction mixture, typical for Cu(II) coordinated by amines.[52;53] During the heat-up to 260 °C, the color of the solution changes from

blue to yellow around 185 °C, indicating the reduction of Cu(II) to Cu(I). Concomitant with the color change, new resonances appear in the ^{1}H NMR spectrum of the reaction mixture, see Figure 2.12. We assign these resonances to the secondary aldimine. Upon reaching the reaction temperature (240–260 °C), the reaction mixture turns black (indicating the formation of Cu_3N), and we observe in the ^{1}H NMR spectrum a significant increase in the aldimine concentration (Figure 2.12). We confirmed the identity of the aldimine by synthesizing the secondary aldimine of dodecyl aldehyde and octadeylamine, and we found perfect agreement of the resonances 1–3.

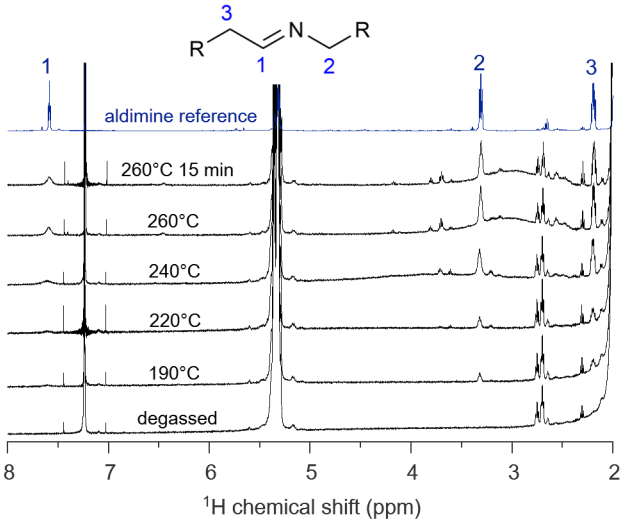

Figure 2.12 | ^{1}H NMR spectra of aliquots after degassing, at 190 °C (after the color change), at 220 °C, at 240 °C, at 260 °C and at the end of the reaction. Aldimine formation is observed starting from 190 °C. The aldimine reference is shown for comparison.

Ammonia is detected in the reaction mixture by bubbling Ar through the reaction mixture during synthesis and dissolving the gasses in either 40 mL or 80 mL water. A commercial ammonia test kit indicates a concentration of 200 mg/L or 100 mg/L respectively (Figure A.2). Given that the reaction is executed at a scale of 0.24 mmol Cu, and assuming that every nitrate (0.48 mmol) oxidizes one OLAm molecule, this is the expected amount of ammonia (0.48 mmol, 8 mg). We can also quantify the aldimine

formation by using the alkene resonance of OLAm as the internal standard. For every aldimine, we find 18 oleyl chains, indicating a conversion of 5.5 %. Given that 7.6 mmol OLAm was used, this amounts to 0.42 mmol aldimine. This value is in reasonable agreement with the amount of ammonia detected (taking into account the error on the ammonia measurement and the fact that OLAm is only 70 % pure). This quantitative picture thus confirms our hypothesis and indicates a one-to-one stoichiometry between nitrate, aldimine, and ammonia. We did not obtain Cu_3N in this experiment since we removed ammonia from the reaction mixture. This indicates that ammonia is essential in nitride formation. Literature shows that ammonia indeed reacts with copper salts to Cu_3N.[16;24]

We also quantified the small amount of aldimine (0.1 mmol) generated during the reduction of Cu(II) to Cu(I). This value is about half of the copper amount (0.24 mmol) and can be easily rationalized based on electron counting in the redox reactions. Indeed, the reduction of Cu(II) to Cu(I) is a one-electron process while the oxidation of primary amine to aldimine is a two-electron process, see Figure 2.13. Aldimine has also been observed in the synthesis of Cu(0) and Pd(0) NCs,[54;55] and it appears to be the typical oxidation product of OLAm. Figure 2.13 also makes clear that the oxidation of primary amine generates a large amount of protons which are presumably absorbed by the excess OLAm. These protons are observed in the ^{1}H NMR spectrum as a broad resonance around 3 ppm, see Figure 2.12. They do not appear in the typical region for alkylammonium resonances, since maximally 1.2 mmol protons are generated and OLAm is still present in excess (7 mmol). Given that proton equilibria are typically fast, we thus observe the population averaged chemical shift between protonated OLAm and unprotonated OLAm.

Our proposed pathway requires a primary amine. To further test our hypothesis, we thus attempted the synthesis of Cu_3N with dioctylamine and trioctylamine. As expected, the reaction did not produce Cu_3N but Cu_2O instead, see Figure 2.14. Also in the NMR spectrum, we do not find aldimine in the case of trioctylamine and only a very small amount in the case of dioctylamine. The latter can be directly oxidized

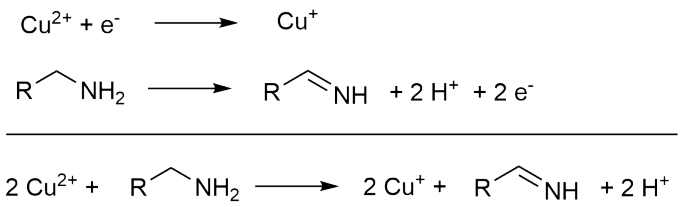

Figure 2.13 | Redox half reactions and overall reaction for the reduction of Cu^{2+} by primary amines.

to a secondary aldimine, without a primary aldimine intermediate (and thus without ammonia elimination) (Figure A.3). As an additional control, we performed a reaction with copper(II) nitrate and dioctylamine, and bubbled ammonia through the reaction mixture as soon as Cu(I) was formed. *p*XRD analysis shows that Cu_3N is formed during this reaction along with some Cu_2O (Figure A.4). This control experiment suggests that our proposed pathway – Cu(I) reacting with in-situ produced ammonia – is plausible.

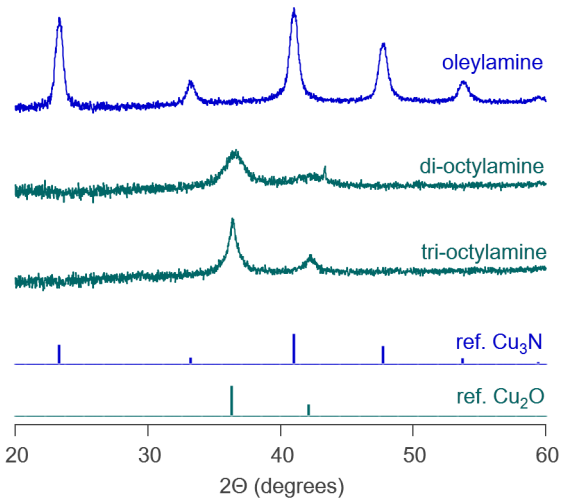

Figure 2.14 | *p*XRD spectra of the syntheses with different amines. The reference of bulk Cu_3N (blue) and bulk Cu_2O (green) are shown.

We thus firmly established that nitrate is not the nitrogen source for Cu_3N but rather oxidizes the amine to aldimine. Cu_3PdN nanocrystal follows the same mechanism based on the formation of aldimine and ammonia during the reaction (Figure A.5).

The mechanism is reminiscent of the one for InN, where In_3^+ oxidizes primary amines into aldimine and nucleophilic attack of lithium oleylamide generates amide, NH_2^-.[56] However, an important difference is that for copper, an additional oxidant (nitrate) is required. The reduction of Cu^{2+} alone does not seem to generate sufficient ammonia to form Cu_3N since other copper salts do not generate Cu_3N.[19] Or perhaps it generates ammonia at too low temperatures, where the formation of Cu_3N is not yet favored. More detailed insight into the crystallization mechanism of Cu_3N could shed light on this issue.

2.3.5 Surface chemistry

XPS was used to explore the surface chemistry. Survey spectra for both compounds (Figure A.6) show spectral signatures from all expected elements. In addition, a small amount of silicon was detected most likely from the silicone grease used during the synthesis. The binding energy (BE) position of the main feature in the Cu $2p_{3/2}$ core level (932.7 ± 0.1 eV) is commensurate with the expected Cu(I) oxidation state for both samples (Figure 2.15A). In addition, both samples show a shoulder towards the higher BE of the main peak (marked with an asterisk in Figure 2.15A), and in the Cu_3PdN sample, a clear Cu(II) satellite is also visible. From peak fit analysis (Figure A.7), the contribution of these additional chemical states relative to the main Cu(I) line is 12.3 ± 0.5 rel.at.% for Cu_3N and 17.9 ± 0.5 rel.at.% for Cu_3PdN, respectively. The Pd $3d$ core level (Figure 2.15B) is only observed for the Cu_3PdN sample. The BE of the Pd $3d_{5/2}$ component (335.5 ± 0.1 eV) is commensurate with Pd(0) or Pd(I) with a spin-orbit-splitting of the doublet of 14.6 eV. In both samples, the N $1s$ core level (Figure 2.15C) displays two contributions. The lower BE feature at 397.8 ± 0.2 eV corresponds to metal-nitride and the higher BE feature at 399.6 ± 0.2 eV corresponds to the expected OLAm ligand, bound to the nanocrystal surface. The O $1s$ core level (Figure 2.15D) shows three discernible contributions from metal oxide, metal hydroxide, and carboxylate environments. Together with the Cu(II) species, we infer that the surface of the particles contains an amorphous copper oxyhydroxide layer. The carboxylate is assigned to a

surface bound oleate ligand and its presence is also detected by FT-IR (broad signal at 1577 cm^{-1}, see (Figure 2.16). Oleate is most likely formed by oxidation of OLAm by nitrate, as we reported earlier in the synthesis of cerium oxide NCs.[28]

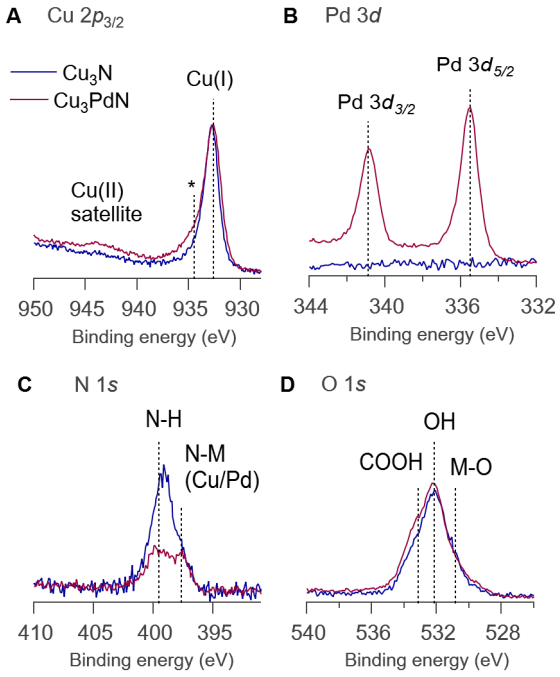

Figure 2.15 | XPS core level spectra of Cu_3N and Cu_3PdN, including (A) Cu $2p_{3/2}$, (B) Pd $3d$, (C) N $1s$, and (D) O $1s$.

The ^{1}H NMR spectra of Cu_3N and Cu_3PdN show the typical signature of an oleyl chain (Figure 2.17A). While the alkene resonance is reasonably sharp, the resonances close to the binding group are indistinguishable from the background. This broadening is likely due to fast T_2 relaxation induced by copper.[34] Based on the line width of the alkene resonance,[57] we inferred that the ligand is dynamic and in a fast exchange between a bound and free state. This is confirmed by a relatively high diffusion coefficient (D = 174μm^2/s) determined by pulsed field gradient experiments on the Cu_3N dispersion (Figure A.8). For Cu_3PdN, we noticed a second, very broad alkene resonance of low intensity underneath the sharp signal. A careful pulsed field gradient experiment revealed that the alkene resonance is a superposition of two species, one diffusing with D = 48

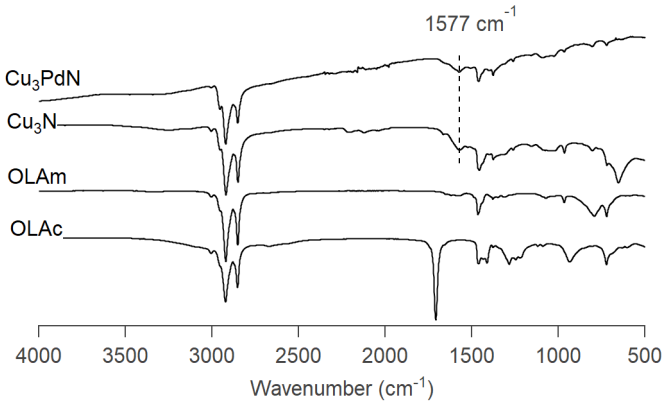

Figure 2.16 FT-IR spectra of Cu_3N NCs after purification compared with OLAm and oleic acid (OA) references. The C=O vibration of bound oleate is detected at 1577 cm^{-1}.

μm^2/s and the other one with D = 667 μm^2/s (Figure 2.17B). The small diffusion coefficient corresponds to a solvodynamic diameter of 17 nm (via the Stokes-Einstein equation), which agrees quite well with a nanocrystal of 12 nm and a ligand shell of 2 nm thickness. We thus assign the broad resonance to a tightly bound ligand, presumably the oleate. The larger diffusion constant corresponds most likely to OLAm. We could only detect the tightly bound oleate in the Cu_3PdN sample, but oleate is also present on the surface of Cu_3N according to our XPS results, albeit to a lesser extent. Unfortunately, all signals appear more broadened in the Cu_3N sample and the tightly bound oleate could not be detected in NMR.

In addition to the identification of the chemical states present in the samples, XPS was also used to probe the electronic structure of Cu_3N and Cu_3PdN by collecting valence band spectra. Figure 2.18A shows the valence band spectra of the two compounds, as well as the broadened and cross section weighted total density of states of Cu_3N from DFT calculations. The experimental and theoretical results for Cu_3N agree very well. The projected density of states calculations (Figure A.9) show that the valence band of Cu_3N is dominated by Cu 3d states with only minor mixing of Cu 3p states and minimal nitrogen contributions. The valence band maximum (VBM) position of Cu_3N is 0.55 ±

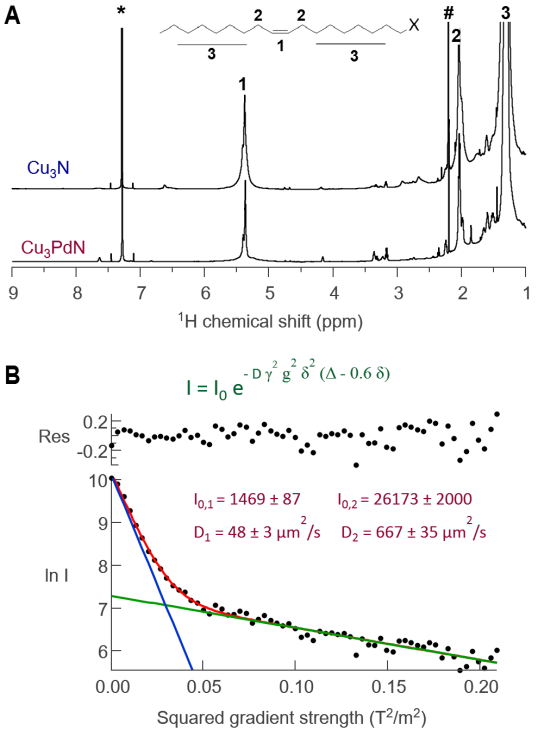

Figure 2.17 NMR of the purified Cu_3N and Cu_3PdN NCs. (A) ^{1}H-NMR spectrum of the NCs in chloroform-d indicating the presence of an tablel chain. The resonance marked with # belongs to residual acetone. (B) Diffusion decay of the alkene region of the Cu_3PdN NCs showing a slow and a fast diffusing species. The residuals of the fit are also shown.

0.05 eV from the Fermi energy (E_F). In comparison, the valence spectrum of Cu_3PdN shows additional intensity towards the E_F from Pd states closing the VBM-E_F gap.

In parallel, UV-Vis has been used to determine the optical band gap of the particles. An indirect band gap has been reported for Cu_3N thin films according to theoretical band structure calculations.[1] To our knowledge, the type of optical band gap (direct or indirect) has not yet been reported for Cu_3PdN. In this work, we assumed an indirect optical bandgap for both samples. A Tauc plot analysis resulted in an optical bandgap of 1.4 ± 0.1 eV and 0.2 ± 0.1 eV for our Cu_3N and Cu_3PdN NCs, respectively (Figure 2.18B and 2.18C). The reduction in optical band gap is commensurate with the closing of the electronic VBM-E_F separation observed in XPS.

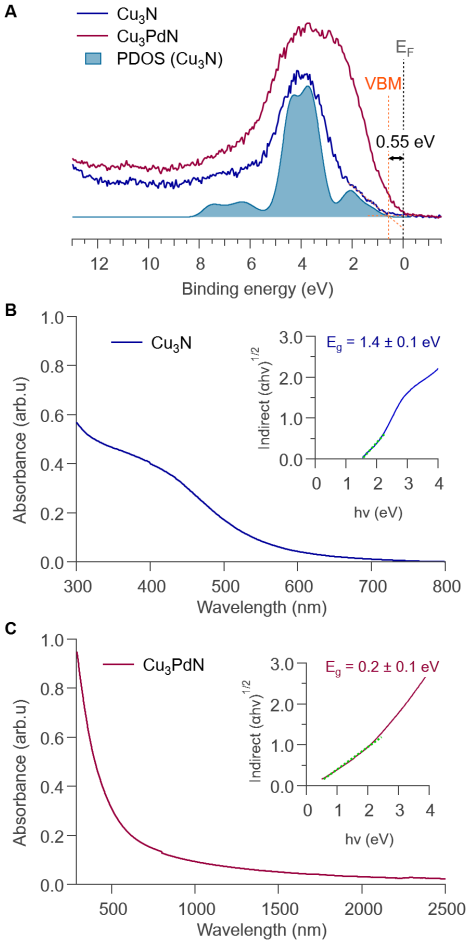

Figure 2.18 (A) Valence region of Cu_3N and Cu_3PdN, including XPS valence spectra and the broadened and cross-section-weighted sum of the projected density of states (PDOS) from DFT. The position of the VBM of Cu_3N and the position of the Fermi energy (E_F) are also shown. (B)-(C) UV-Vis absorption spectra of Cu_3N in cyclohexane and Cu_3PdN in tetrachloroethylene with their corresponding Tauc plots as an inset, respectively. Indirect bandgaps were determined from linear fitting to the low energy region of the Tauc plots (shown in the dotted green line).

2.4 Conclusion

In conclusion, we successfully optimized the synthesis of Cu_3N and Cu_3PdN NCs in order to obtain phase pure, colloidally stable NCs via modulating the reaction parameters with a focus on the purification. We provided experimental support for a precursor conversion pathway that hypothesized ammonia as the active nitrogen source. We proposed that primary aldimine is the oxidation product of the ligand (OLAm), oxidized by both Cu(II) and nitrate. Nucleophilic addition and elimination of a second OLAm molecule onto the primary aldimine released ammonia, which subsequently reacted with Cu(I) to form Cu_3N and Cu_3PdN. The surface of the NCs was capped by a mixture of OLAm and oleate. The latter was formed in situ from the further oxidation of aldimine. The addition of palladium to Cu_3N reduces the optical band gap as well as the separation between the VBM and Fermi energy (E_F).

References

[1] Zakutayev, A.; Caskey, C. M.; Fioretti, A. N.; Ginley, D. S.; Vidal, J.; Stevanovic, V.; Tea, E.; Lany, S. Defect Tolerant Semiconductors for Solar Energy Conversion. *Journal of Physical Chemistry Letters* **2014**, *5*, 1117–1125.

[2] Maruyama, T.; Morishita, T. Copper nitride and tin nitride thin films for write-once optical recording media. *Applied Physics Letters* **1996**, *69*, 890–891.

[3] Yin, Z.; Yu, C.; Zhao, Z.; Guo, X.; Shen, M.; Li, N.; Muzzio, M.; Li, J.; Liu, H.; Lin, H.; Yin, J.; Lu, G.; Su, D.; Sun, S. Cu_3N Nanocubes for Selective Electrochemical Reduction of CO_2 to Ethylene. *Nano Letters* **2019**, *19*, 8658–8663.

[4] Panda, C.; Menezes, P. W.; Zheng, M.; Orthmann, S.; Driess, M. In Situ Formation of Nanostructured Core–Shell Cu_3N–CuO to Promote Alkaline Water Electrolysis. *American Chemical Society Energy Letters* **2019**, *4*, 747–754.

[5] Xi, P. X.; Xu, Z. H.; Gao, D. Q.; Chen, F. J.; Xue, D. S.; Tao, C. L.; Chen, Z. N. Solvothermal synthesis of magnetic copper nitride nanocubes with highly electrocatalytic reduction properties. *Royal Society of Chemistry Advances* **2014**, *4*, 14206–14209.

[6] Bocharov, D.; Anspoks, A.; Timoshenko, J.; Kalinko, A.; Krack, M.; Kuzmin, A. Interpretation of the Cu K-edge EXAFS spectra of Cu_3N using ab initio molecular dynamics. *Radiation Physics and Chemistry* **2020**, *175*, 108100–8.

[7] Paniconi, G.; Stoeva, Z.; Doberstein, H.; Smith, R. I.; Gallagher, B. L.; Gregory, D. H. Structural chemistry of Cu_3N powders obtained by ammonolysis reactions. *Solid State Sciences* **2007**, *9*, 907–913.

[8] Cui, X. Y.; Soon, A.; Phillips, A. E.; Zheng, R. K.; Liu, Z. W.; Delley, B.; Ringer, S. P.; Stampfl, C. First principles study of 3d transition metal dopedCu_3N. *Journal of Magnetism and Magnetic Materials* **2012**, *324*, 3138–3143.

[9] Jacobs, H.; Zachwieja, U. Kupferpalladiumnitride, Cu_3Pd_xN mit x = 0,020 und 0,989, Perowskite mit "bindender $3d^{10}$-$4d^{10}$-Wechselwirkung". *Journal of the Less Common Metals* **1991**, *170*, 185–190.

[10] Hahn, U.; Weber, W. Electronic structure and chemical-bonding mechanism of Cu_3N, Cui_3NPd, and related Cu(I) compounds. *Physical Review B* **1996**, *53*, 12684–12693.

[11] Gulo, F.; Simon, A.; Kohler, J.; Kremer, R. K. Li-Cu exchange in intercalated Cu_3N–with a remark on Cu_4N. *Angewandte Chemie International Edition* **2004**, *43*, 2032–4.

[12] Choi, J.; Gillan, E. G. Solvothermal synthesis of nanocrystalline copper nitride from an energetically unstable copper azide precursor. *Inorganic Chemistry* **2005**, *44*, 7385–93.

[13] Zachwieja, U.; Jacobs, H. Ammonothermalsynthese von kupfernitrid, Cu_3N. *Journal of the Less Common Metals* **1990**, *161*, 175–184.

[14] Juza, R.; Hahn, H. Kupfernitrid Metallamide und Metallnitride. VII. *Zeitschrift for anorganische und allgemeine Chemie* **1939**, *241*, 172–178.

[15] Deshmukh, R.; Zeng, G. B.; Tervoort, E.; Staniuk, M.; Wood, D.; Niederberger, M. Ultrasmall Cu_3N Nanoparticles: Surfactant-Free Solution-Phase Synthesis, Nitridation Mechanism, and Application for Lithium Storage. *Chemistry of Materials* **2015**, *27*, 8282–8288.

[16] Egeberg, A.; Warmuth, L.; Riegsinger, S.; Gerthsen, D.; Feldmann, C. Pyridine-based low-temperature synthesis of CoN, Ni_3N and Cu_3N nanoparticles. *Chemical Communications journal* **2018**, *54*, 9957–9960.

[17] Wu, H.; Chen, W. Copper nitride nanocubes: size-controlled synthesis and application as cathode catalyst in alkaline fuel cells. *J Am Chem Soc* **2011**, *133*, 15236–9.

[18] Vaughn Ii, D. D.; Araujo, J.; Meduri, P.; Callejas, J. F.; Hickner, M. A.; Schaak, R. E. Solution Synthesis of Cu_3PdN Nanocrystals as Ternary Metal Nitride Electrocatalysts for the Oxygen Reduction Reaction. *Chemistry of Materials* **2014**, *26*, 6226–6232.

[19] Wang, D.; Li, Y. Controllable synthesis of Cu-based nanocrystals in ODA solvent. *Chem Commun (Camb)* **2011**, *47*, 3604–6.

[20] Sithole, R. K.; Machogo, L. F. E.; Moloto, M. J.; Gqoba, S. S.; Mubiayi, K. P.; Van Wyk, J.; Moloto, N. One-step synthesis of Cu_3N, Cu_2S and Cu_9S_5 and photocatalytic degradation of methyl orange and methylene blue. *Journal of Photochemistry and Photobiology a-Chemistry* **2020**, *397*, 112577.

[21] Kadzutu-Sithole, R.; Machogo-Phao, L. F. E.; Kolokoto, T.; Zimuwandeyi, M.; Gqoba, S. S.; Mubiayi, K. P.; Moloto, M. J.; Wyk, J. V.; Moloto, N. Elucidating the effect of precursor decomposition time on the structural and optical properties of copper(I) nitride nanocubes. *Royal Society of Chemistry Advances* **2020**, *10*, 34231–34246.

[22] Lord, R. W.; Holder, C. F.; Fenton, J. L.; Schaak, R. E. Seeded Growth of Metal Nitrides on Noble-Metal Nanoparticles To Form Complex Nanoscale Heterostructures. *Chemistry of Materials* **2019**, *31*, 4605–4613.

[23] Mondal, S.; Raj, C. R. Copper Nitride Nanostructure for the Electrocatalytic Reduction of Oxygen: Kinetics and Reaction Pathway. *Journal of Physical Chemistry C* **2018**, *122*, 18468–18475.

[24] Nakamura, T.; Hayashi, H.; Hanaoka, T. A.; Ebina, T. Preparation of copper nitride (Cu_3N) nanoparticles in long-chain alcohols at 130-200 degrees C and nitridation mechanism. *Inorganic Chemistry* **2014**, *53*, 710–5.

[25] Sithole, R. K.; Machogo, L. F. E.; Airo, M. A.; Gqoba, S. S.; Moloto, M. J.; Shumbula, P.; Van Wyk, J.; Moloto, N. Synthesis and characterization of Cu_3N nanoparticles using pyrrole-2-carbaldpropyliminato Cu(II) complex and $Cu(NO_3)_2$ as single-source precursors: the search for an ideal precursor. *New Journal of Chemistry* **2018**, *42*, 3042–3049.

[26] Housecroft, C. *Inorganic Chemistry*; Pearson, 2018; Vol. 72, pp 650–651.

[27] De Keukeleere, K.; Coucke, S.; De Canck, E.; Van Der Voort, P.; Delpech, F.; Coppel, Y.; Hens, Z.; Van Driessche, I.; Owen, J. S.; De Roo, J. Stabilization of Colloidal Ti, Zr, and Hf Oxide Nanocrystals by Protonated Tri-n-octylphosphine Oxide (TOPO) and Its Decomposition Products. *Chemistry of Materials* **2017**, *29*, 10233–10242.

[28] Calcabrini, M.; den Eynden, D. V.; Ribot, S. S.; Pokratath, R.; Llorca, J.; Roo, J. D.; Ibáñez, M. Ligand Conversion in Nanocrystal Synthesis: The Oxidation of Alkylamines to Fatty Acids by Nitrate. *Journal of the American Chemical Society Gold* **2021**, *1*, 1898–1903.

[29] Boles, M. A.; Ling, D.; Hyeon, T.; Talapin, D. V. The surface science of nanocrystals. *Nature Materials* **2016**, *15*, 141–53.

[30] Fritzinger, B.; Moreels, I.; Lommens, P.; Koole, R.; Hens, Z.; Martins, J. C. In Situ Observation of Rapid Ligand Exchange in Colloidal Nanocrystal Suspensions Using Transfer NOE Nuclear Magnetic Resonance Spectroscopy. *Journal of the American Chemical Society* **2009**, *131*, 3024–3032.

[31] Anderson, N. C.; Chen, P. E.; Buckley, A. K.; De Roo, J.; Owen, J. S. Stereoelectronic Effects on the Binding of Neutral Lewis Bases to CdSe Nanocrystals. *Journal of the American Chemical Society* **2018**, *140*, 7199–7205.

[32] Grote, C.; Chiad, K. J.; Vollmer, D.; Garnweitner, G. Unspecific ligand binding yielding stable colloidal ITO-nanoparticle dispersions. *Chemical Communications journal* **2012**, *48*, 1464–1466.

[33] Dierick, R.; den Broeck, F. V.; Nolf, K. D.; Zhao, Q.; Vantomme, A.; Martins, J. C.; Hens, Z. Surface Chemistry of $CuInS_2$ Colloidal Nanocrystals, Tight Binding of L-Type Ligands. *Chemistry of Materials* **2014**, *26*, 5950–5957.

[34] Oliva-Puigdomènech, A.; De Roo, J.; Kuhs, J.; Detavernier, C.; Martins, J. C.; Hens, Z. Ligand Binding to Copper Nanocrystals: Amines and Carboxylic Acids and the Role of Surface Oxides. *Chemistry of Materials* **2019**, *31*, 2058–2067.

[35] Ashiotis, G.; Deschildre, A.; Nawaz, Z.; Wright, J. P.; Karkoulis, D.; Picca, F. E.; Kieffer, J. The fast azimuthal integration Python library:pyFAI. *Journal of Applied Crystallography* **2015**, *48*, 510–519.

[36] Wright, C. J.; Zhou, X.-D. Computer-assisted area detector masking. *Journal of Synchrotron Radiation* **2017**, *24*, 506–508.

[37] Juhás, P.; Davis, T.; Farrow, C. L.; Billinge, S. J. L. PDFgetX_3: a rapid and highly automatable program for processing powder diffraction data into total scattering pair distribution functions. *Journal of Applied Crystallography* **2013**, *46*, 560–566.

[38] Yang, X.; Juhas, P.; Farrow, C. L.; Billinge, S. J. L. xPDFsuite: an end-to-end software solution for high throughput pair distribution function transformation, visualization and analysis. *arXiv: Materials Science* **2014**.

[39] Juhás, P.; Farrow, C. L.; Yang, X.; Knox, K. R.; Billinge, S. J. L. Complex modeling: a strategy and software program for combining multiple information sources to solve ill posed structure and nanostructure inverse problems. *Acta Crystallographica Section A Foundations and Advances* **2015**, *71*, 562–568.

[40] Farrow, C. L.; Juhas, P.; Liu, J. W.; Bryndin, D.; Božin, E. S.; Bloch, J.; Proffen, T.; Billinge, S. J. L. PDFfit$_2$ and PDFgui: computer programs for studying nanostructure in crystals. *Journal of Physics: Condensed Matter* **2007**, *19*, 335219.

[41] Lany, S. Band-structure calculations for the 3d transition metal oxides in GW. *Physical Review B* **2013**, *87*, 085112.

[42] Stevanović, V.; Lany, S.; Zhang, X.; Zunger, A. Correcting density functional theory for accurate predictions of compound enthalpies of formation: Fitted elemental-phase reference energies. *Physical Review B* **2012**, *85*, 115104.

[43] Lany, S. Semiconducting transition metal oxides. *Journal of Physics: Condensed Matter* **2015**, *27*, 283203.

[44] Scofield, J. H. Theoretical photoionization cross sections from 1 to 1500 keV. **1973**.

[45] Jackson, A. J.; Ganose, A. M.; Regoutz, A.; Egdell, R. G.; Scanlon, D. O. Galore: Broadening and weighting for simulation of photoelectron spectroscopy. *Journal of Open Source Software* **2018**, *3*, 773.

[46] C. Kalha, A. R., N. K. Fernando *Digitisation of Scofield Photoionisation Cross Section Tabulated Data*, 2020.

[47] Sinnaeve, D. The Stejskal-Tanner equation generalized for any gradient shape-an overview of most pulse sequences measuring free diffusion. *Concepts in Magnetic Resonance Part A* **2012**, *40A*, 39–65.

[48] Dhaene, E.; Billet, J.; Bennett, E.; Van Driessche, I.; De Roo, J. The Trouble with ODE: Polymerization during Nanocrystal Synthesis. *Nano Letters* **2019**, *19*, 7411–7417.

[49] Zito, J.; Infante, I. The Future of Ligand Engineering in Colloidal Semiconductor Nanocrystals. *Accounts of Chemical Research* **2021**, *54*, 1555–1564.

[50] Doblas, D.; Kister, T.; Cano-Bonilla, M.; González-García, L.; Kraus, T. Colloidal Solubility and Agglomeration of Apolar Nanoparticles in Different Solvents. *Nano Letters* **2019**, *19*, 5246–5252.

[51] Castilla-Amorós, L.; Stoian, D.; Pankhurst, J. R.; Varandili, S. B.; Buonsanti, R. Exploring the Chemical Reactivity of Gallium Liquid Metal Nanoparticles in Galvanic Replacement. *Journal of the American Chemical Society* **2020**, *142*, 19283–19290.

[52] Cui, H.; Zhu, G.; Liu, X.; Liu, F.; Xie, Y.; Yang, C.; Lin, T.; Gu, H.; Huang, F. Niobium Nitride Nb_4N_5 as a New High-Performance Electrode Material for Supercapacitors. *Advanced Science* **2015**, *2*, 1500126.

[53] Jeong, S.; Liu, Y.; Zhong, Y.; Zhan, X.; Li, Y.; Wang, Y.; Cha, P. M.; Chen, J.; Ye, X. Heterometallic Seed-Mediated Growth of Monodisperse Colloidal Copper Nanorods with Widely Tunable Plasmonic Resonances. *Nano Letters* **2020**, *20*, 7263–7271.

[54] Man, R. W. Y.; Brown, A. R. C.; Wolf, M. O. Mechanism of Formation of Palladium Nanoparticles: Lewis Base Assisted, Low-Temperature Preparation of Monodisperse Nanoparticles. *Angewandte Chemie International Edition* **2012**, *51*, 11350–11353.

[55] Villanueva, F. Y.; Green, P. B.; Qiu, C.; Ullah, S. R.; Buenviaje, K.; Howe, J. Y.; Majewski, M. B.; Wilson, M. W. B. Binary $Cu_{2-x}S$ Templates Direct the Formation of Quaternary Cu_2ZnSnS_4 (Kesterite, Wurtzite) Nanocrystals. *ACS Nano* **2021**, *15*, 18085–18099.

[56] Chen, Y.; Landes, N. T.; Little, D. J.; Beaulac, R. Conversion Mechanism of Soluble Alkylamide Precursors for the Synthesis of Colloidal Nitride Nanomaterials. *Journal of the American Chemical Society* **2018**, *140*, 10421–10424.

[57] De Roo, J.; Yazdani, N.; Drijvers, E.; Lauria, A.; Maes, J.; Owen, J. S.; Van Driessche, I.; Niederberger, M.; Wood, V.; Martins, J. C.; Infante, I.; Hens, Z. Probing Solvent–Ligand Interactions in Colloidal Nanocrystals by the NMR Line Broadening. *Chemistry of Materials* **2018**, *30*, 5485–5492.

Success is walking from failure to failure with no loss of enthusiasm.

Winston Churchill

3 Molecular Precursors Towards Metal Nitrides Formation

3.1 Preamble

Based on the concept of solution-based synthesis of Cu_3N, we have chosen to investigate the synthesis of various metal nitrides in solution at low temperatures. The primary motivation for avoiding high temperatures ($\geq$ 500 °C) is to prevent irreversible agglomeration, promote uniform compositions with high surface areas, and achieve precise size control. Our objective is to develop a synthesis method that can produce colloidally stable nitride nanocrystals (NCs) at a reasonably low temperature (350 °C $\leq$) by utilizing a standard glassware setup. In the subsequent sections, we present our studies on the synthesis of titanium nitride (TiN), zinc nitride (Zn_3N_2), and nickel nitride (Ni_3N).

3.2 Titanium nitride syntheses

A benzene-thermal reaction of $TiCl_4$ with NaN_3 at temperatures around 350-380 °C using an autoclave has been reported yielding 50 nm aggregated particles.[1] When $Ti(NMe_2)_4$ is treated with primary amines such as *n*-propylamine, *n*-octylamine or *tert*-butylamine, transamination occurs.[2–4] The primary amido group then self-condensates to form alkylim-

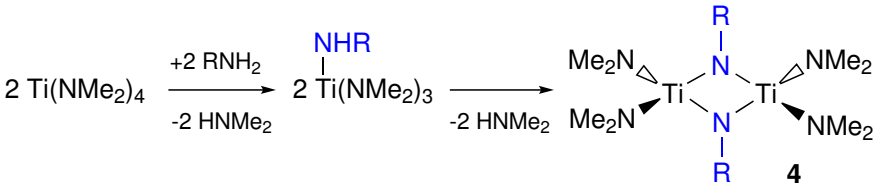

Figure 3.1 | Transamination followed by self-condensation of primary metal amide group.

ido bridges, see Figure 3.1. The rate of transamination and condensation is dependent on the steric hindrance between the alkyl groups of the amine, as it proceeds rapidly at room temperature for *n*-propylamine whereas *tert*-butylamine only forms the condensed product at 100 °C.[4] If an excess of primary amine is used, a polymeric, insoluble product is obtained.[3] However, sols can be formed in tetrahydrofuran (THF) by controlling the stoichiometry of amine to titanium. These sols have then been used to coat silica by dip-coating and Ti(C,N) and TiN have been obtained by pyrolysis at high temperatures (at least 800 °C) under nitrogen or ammonia atmosphere respectively.[5]

The addition of one equivalent of primary amine to $Ti(NMe_2)_4$, forms the dimer **4**, which can be rearranged to a monomeric imido species by coordination of a Lewis base. Addition of two equivalents of trimethylsilylchloride to the latter complex yields the dichloroimido complex.[4;6] The same product can be prepared by adding a primary amine to $Ti(NMe_2)_2Cl_2$.[7] Although most of the above titanium complexes have not yet been used so far to synthesize TiN NCs, they serve as valuable inspiration for future synthetic development and provide insight into the precursor chemistry of titanium and the rest of Group 4.

Recently, titanium chloride was reacted with potassium amide in pyridine at 300 °C.[8] While the transmission electron microscopy (TEM) image showed an isolated TiN NC of 5 nm, the x-ray powder diffraction (*p*XRD) pattern was too broad to be consistent with a large ensemble of 5 nm crystals. In fact, another TEM image clearly shows aggregated particles in an amorphous matrix.

Various approaches have been used to obtain metal nitrides. In this chapter, we will

comment on each approach based on the choice of nitrogen source. All our strategies are based on the formation of an amorphous Ti-N network which then crystallizes into TiN NCs at higher temperatures.

Molecular nitrogen precursors

Our very first approach was to use a primary amine as our nitrogen source for nitride formation, as such amines are known to be very good ligands for Ti(IV). Furthermore, based on our Cu_3N results, we learned that ammonia is an excellent nitrogen source for nitride formation.[9;10] Benzylamine was our first primary amine of choice as it is known to decompose into ammonia and toluene at a temperature of around 270 °C in the presence of titanium.[11] Starting with tetrakis(dimethylamido)titanium(IV) as the titanium source and benzylamine, we were able to obtain a ligand exchange at room temperature via the release of dimethylamine gas. This ligand exchange is visually observed by a slow color change from yellow to orange. The release of dimethylamine and the binding of benzylamine are confirmed by nuclear magnetic resonance (NMR) (Figure 3.2). This mixture is then transferred to a microwave and heated at different temperatures and times.

Nonetheless, the resulting products did not exhibit a crystalline structure and showed a flat diffractogram during *p*XRD analysis. Through NMR and gas chromatography–mass spectrometry (GC-MS) analysis, toluene and imine were identified in the crude mixture, indicating the decomposition of our primary amine, see Figure 3.3.

To address this issue, various modifications to the reaction conditions were explored, including adjusting the nitrogen source equivalents (ranging from 4 to 100 equivalents), temperature (ranging from 150 °C to 350 °C), and reaction time (ranging from 1 h to 24 h). In an attempt to modify the reaction kinetics and achieve a crystalline product, para-substituted methoxy, and chlorobenzylamine were utilized using the same procedure. Unfortunately, both substrates yielded the same amorphous product (Figure 3.4).

The inclusion of $TiCl_4$ as the titanium precursor resulted in the formation of crys-

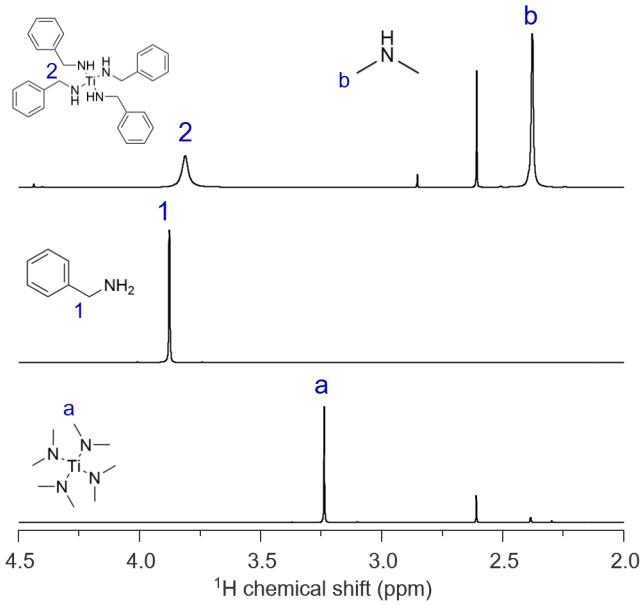

Figure 3.2 | ^{1}H-NMR of $Ti(NMe_2)_4$, benzylamine and $Ti(NMe_2)_4$ + benzylamine in chloroform-*d*.

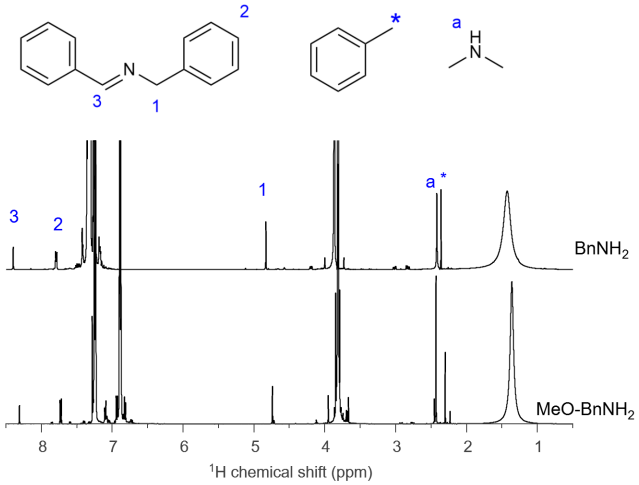

Figure 3.3 | ^{1}H-NMR of the crude from the reaction of $Ti(NMe_2)_4$ with benzylamine and *p*-MeO-$BnNH_2$ at 260 °C. The most intense peaks are assigned to $BnNH_2$. The resonances of *p*-MeO-$BnNH_2$ are all deshielded as compared to $BnNH_2$ due to the presence of the MeO.

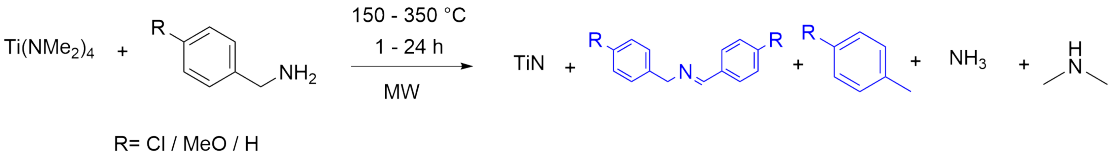

Figure 3.4 | Chemical equation of $Ti(NMe_2)_4$ reaction with benzylamine. In blue are the molecules identified via GC-MS and ^{1}H-NMR.

talline ammonium chloride, providing further evidence of primary amine decomposition to ammonia, see Figure 3.5. Based on these findings, it can be inferred that the transamination and self-condensation processes have successfully formed an amorphous Ti-N network. However, the main challenge encountered in this study was the inability to achieve crystallization of the desired product.

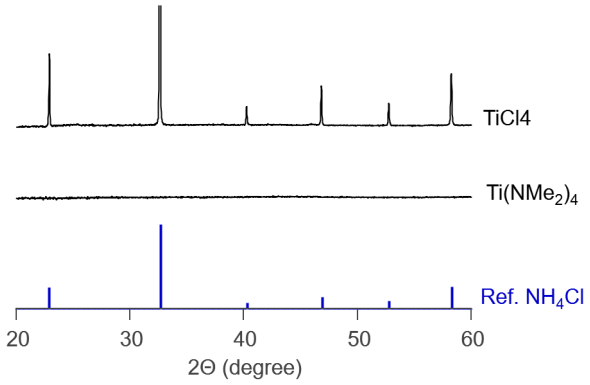

Figure 3.5 | *p*XRD of the product obtained after reaction with benzylamine at 260 °C. In blue is the reference of bulk NH_4Cl.

Oleylamine (OLAm) was selected as an alternative primary amine to react with $Ti(NMe_2)_4$. Upon addition of the amine, a color change was observed at room temperature, indicating successful transamination. However, despite reacting for 3 h at 350 °C, the resulting product remained amorphous. The presence of aldimine in the crude mixture further confirmed the formation of ammonia.[10] To facilitate pre-formed bonding between titanium and nitrogen, an experiment was conducted involving the in-situ formation of RHNLi using *tert*-BuLi and OLAm. This reaction yielded an unknown broad pattern in the *p*XRD, which, after calcination at 800 °C under N_2, resulted in

the formation of a TiO_2 rutile phase.

Subsequently, guanidines and imines were selected based on a similar mechanism as thioureas used in metal sulfide formation. Commencing with $Ti(NMe_2)_4$, ligand exchange was observed via NMR, leading to the release of free dimethylamine. An additional equivalent of guanidine was then required to facilitate the formation of TiN, see Figure 3.6. However, regardless of the variations in equivalents, temperatures, and reaction times attempted, all outcomes yielded an amorphous black powder that, upon calcination at 800 °C, transformed into TiO_2.

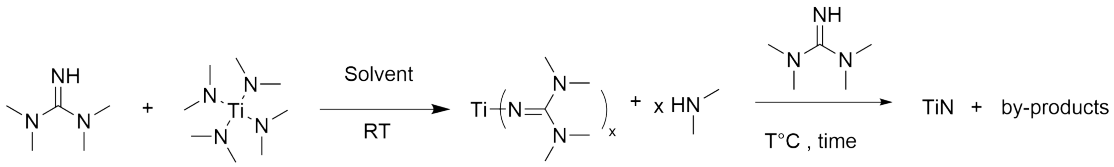

Figure 3.6 | Chemical equation of the reaction of $Ti(NMe_2)_4$ with guanidine.

Following that, tris(trimethylsilyl)amine (TMS amine), chosen as a nitrogen source similar to ammonia but with higher reactivity driven by Si-halogen bond formation, was employed. Various titanium halide precursors ($TiCl_4$ and TiF_4) were utilized. However, in all cases, the final products remained amorphous, although trimethylsilyl halide molecules were formed. These syntheses were inspired by the procedure described in the introduction chapter for the synthesis of Ta_3N_2.[12] All the results discussed so far have been summarised in Table 3.1.

An alternative approach we explored involved the formation of other metal nitrides using Cu_3N. In a previous chapter, it was discussed that Cu_3N decomposes into Cu(0) and ammonia at higher temperatures.[13] Initially, we attempted an in situ approach where Cu_3N was synthesized and the new metal precursor was directly injected into the solution and heated to 350 °C for 3 h. When $TiCl_4$ was used as the precursor, we obtained Cu(0) and ammonium chloride after purification, see Figure 3.7, confirming our hypothesis of ammonia formation. However, the use of $Ti(NMe_2)_4$ in the reaction led to the formation of Cu(0) and residual CuO, as indicated by *p*XRD analysis, possibly with the presence of an amorphous titanium phase. In another approach, we injected purified Cu_3N into a mixture of $TiCl_4$ in tri-*n*-octylphosphine (TOP) at 200 °C, but no precipitate was obtained after 2 h of reaction.

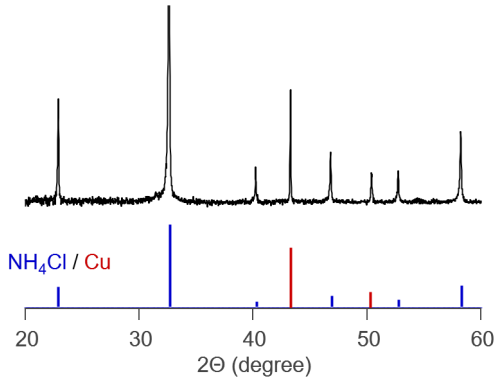

Figure 3.7 *p*XRD of the product obtained from addition of $TiCl_4$ in TOP to Cu_3N reaction mixture. The reaction was unsuccessful in TiN formation, and the decomposition products of Cu_3N are observed.

Table 3.1 | Summary of TiN synthesis attempt via primary amines.

Metal prec.	Nitrogen Source	eq.	Solvent	T °C	Time	Product
$Ti(NMe_2)_4$	$BnNH_2$	100 eq.	-	150 °C MW	1 h	amorphous
$Ti(NMe_2)_4$	$BnNH_2$	100 eq.	-	250 °C MW	19 h	amorphous
$Ti(NMe_2)_4$	$BnNH_2$	100 eq.	-	275 °C MW	19 h	amorphous
$Ti(NMe_2)_4$	*p-MeO*-$BnNH_2$	100 eq.	-	275 °C MW	19 h	amorphous
$Ti(NMe_2)_4$	$BnNH_2$	4 eq.	TOA	275 °C	3 h	amorphous
$Ti(NMe_2)_4$	$BnNH_2$	4 eq.	Squalane	350 °C	3 h	amorphous
$Ti(NMe_2)_4$	NaBnNH	4 eq.	Squalane	350 °C	3 h	amorphous
$TiCl_4$	$BnNH_2$	4 eq.	Squalane	350 °C	3 h	NH_4Cl
$TiCl_4$	$BnNH_2$	8 eq.	Squalane	350 °C	3 h	NH_4Cl
$Ti(NMe_2)_4$	OLAm	4 eq.	Squalane	350 °C	3 h	amorphous
$Ti(NMe_2)_4$	OLAm	8 eq.	Squalane	350 °C	3 h	amorphous
$Ti(NMe_2)_4$	LiOLAm	8 eq.	Squalane	350 °C	3 h	unknown phase
						TiO_2 after calc.
$Ti(NMe_2)_4$	TMG	10 eq.	TOA	350 °C	3 h	amorphous
$Ti(NMe_2)_4$	TMG + OLAm	10 + 2 eq.	TOA	350 °C	3 h	amorphous
$Ti(NMe_2)_4$	TMG + OLAm	5 + 5 eq.	TOA	350 °C	3 h	amorphous
$Ti(NMe_2)_4$	Bn-Imine + OLAm	5 + 5 eq.	TOA	350 °C	3 h	amorphous
$TiCl_4$	TMS-amine	1.5 eq.	Squalane	310 °C	3 h	TMS-Cl

* TOA= Trioctyslamine ; OLAm= Oleylamine ; TMG = Tetramethylguanidine ; Bn-Imine = Benzophenone Imine ; TMS = Tris (Trimethylsilyl)

3.3 Zinc nitride syntheses

A chemical approach was reported by Taylor *et al.* involving the reaction of diethylzinc under an ammonia flow in 1-octadecene (ODE), with OLAm as the capping ligand.

$$ZnEt_2 + NH_3 \xrightarrow[ODE,OLAm]{225\ ^\circ C} Zn_3N_2 \tag{3.1}$$

The size of the NCs is controlled by adding diethylzinc step by step. This resulted in NCs that emit light in the range of 500 to 1100 nm with a photoluminescence quantum yield greater than 50%. The authors also looked at how changing the amount of diethylzinc compared to ammonia affected the growth. When they used less ammonia or more diethylzinc, the particles grew bigger. Using more ammonia made the particles smaller. [14] To minimize the use of hazardous diethyl zinc, our focus has been on exploring alternative reaction strategies that can facilitate the formation of Zn_3N_2.

Exploring new approaches

An attempted strategy involved initiating a reaction through the formation of salts using $ZnCl_2$ as the starting material. To introduce nitrogen, sodium amide, sodium benzylamide, Li_3N_2, and Ca_3N_2 were utilized along with OLAm as a ligand. The solvent of choice was hexadecane, and the reaction was conducted at 260 °C for 1 h. In all cases, these reactions resulted in the complete reduction of Zn(II) to bulk Zn(0), accompanied by the formation of the corresponding chloride salts (Figure 3.8).

Another approach involved starting with a well-defined precursor that already contained the initial Zn-N bond. For this purpose, a $Zn((TMS)_2N)_2$ molecule was synthesized by reacting $ZnCl_2$ with TMS_2NLi at room temperature. When this precursor was used in the reaction without any additional nitrogen source, it led to the formation of bulk Zn(0) and small amounts of ZnO after 1 h reaction at 260 °C. However, when another nitrogen source was introduced along with this zinc precursor such as primary amines, guanidines, or imines, only Zn(0) was formed without any other byproducts in

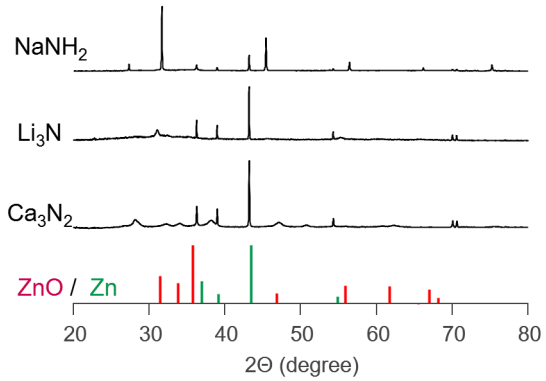

Figure 3.8 | *p*XRD of the salt driven reaction with $ZnCl_2$ at 260 °C for 1 h. The reaction with $NaNH_2$ leads to NaCl, Li_3N to lithium doped Zn(0) and Ca_3N_2 to $Ca(OH)_2$ and Ca(OH)Cl side product formation along with Zn(0).

the same reaction conditions (Figure 3.9).

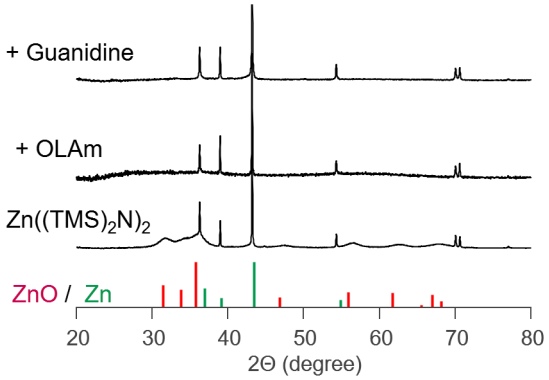

Figure 3.9 | *p*XRD of the product of the reaction of $Zn((TMS)_2N)_2$ with and without nitrogen sources at 260 °C for 1 h.

As a second option, $Zn(NH_3)_6Cl_2$ was selected as a candidate precursor. This precursor proved to be very robust and did not decompose at temperatures as high as 260 °C in the presence of TOP or OLAm as a ligand (Figure 3.10).

In a similar approach to the one employed for TiN, we attempted to synthesize Zn_3N_2 by using Cu_3N as a nitrogen precursor. Initially, purified Cu_3N was introduced into a solution containing $ZnCl_2$ in TOP at a temperature of 50 °C. Subsequently, the resulting

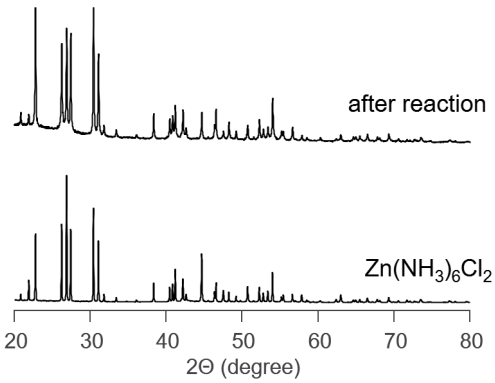

Figure 3.10 *p*XRD of the product of the reaction of $Zn(NH_3)_6Cl_2$ with TOP at 260 °C for 1 h after purification compared to the initial $Zn(NH_3)_6Cl_2$ precursor.

mixture was subjected to various temperatures ranging from 100 °C to 260 °C for 30 minutes. Surprisingly, all the reaction products obtained were identified as ZnO. Due to the known sensitivity of Zn_3N_2 to air and water, all reactions were meticulously purified under inert conditions. Our hypothesis is that the presence of surface-bound oleic acid (OA) on the Cu_3N NCs may have contributed to the introduction of oxygen, leading to the formation of ZnO instead of the desired Zn_3N_2 (Figure 3.11).

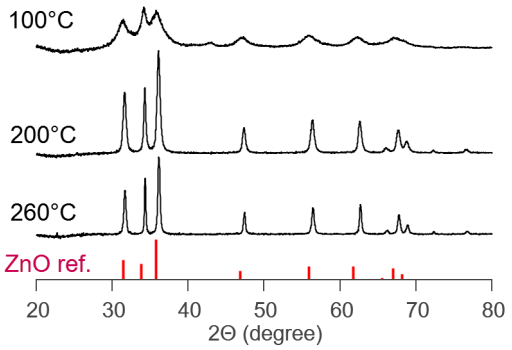

Figure 3.11 *p*XRD of the final products obtained via the reaction of at 100 °C, 200 °C and 260 °C after air-free purification. All products match ZnO.

3.4 Nickel nitride syntheses

A one-step synthesis of colloidally stable Ni_3N NCs has been reported by Shanker *et al.*[15] where nickel(II) acetate is used as the precursor and OLAm as the ligand, see Equation 3.2. The authors detect ammonia during the reaction and conclude that ammonia is the nitrogen source. However, it is unclear how ammonia is generated, as the most logical reaction would be the formation of oleylacetamide and NiO. Different NC sizes (5 to 80 nm) are obtained by varying time and temperature within a narrow window, see Figure 3.12. The NCs are reasonably monodisperse and colloidally stable.

$$Ni(CH_3CO_2)_2 + 2\ RNH_2 \xrightarrow[ODE]{210\text{-}230\ ^\circ C\ \ 5\text{-}10\ min} Ni_3N \tag{3.2}$$

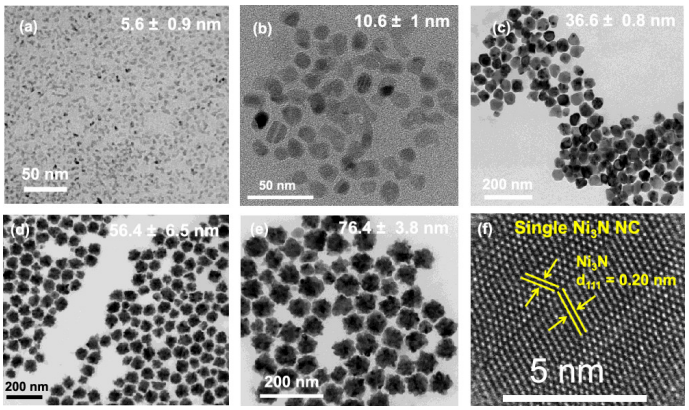

Figure 3.12 TEM images of the different Ni_3N NCs obtained.(a) 5.6 ± 0.9 nm, (b) 10.6 ± 1.0 nm, (c) 36.6 ± 0.8 nm, (d) 56.4 ± 6.5 nm, and (e) 76.4 ± 3.8 nm. (f) high-resolution transmission electron microscopy (HR-TEM) image of a Ni_3N NC with a size of 56.4 ± 6.5 nm. Reprinted with permission from reference[15]. Copyright 2021 American Chemical Society.

Novel approaches

Initially, we attempted to replicate the synthesis procedure described in the literature by starting with nickel(II) acetate and OLAm. The authors mentioned that adjusting the reaction times and temperatures would yield NCs of different sizes. However, in our experiments, although we observed the same color changes as reported, the reaction resulted in the formation of salts. After washing the salts with methanol, we obtained an amorphous phase. We also tried varying the amount of OLAm (nitrogen source), but it did not improve the crystallinity of the product. To improve the crystallization process, we introduced additional nitrogen sources like benzylamine or tetramethylguanidine, which resulted in the complete reduction of Ni(II) to Ni(0). The resulting cubic phase exhibited magnetic properties. Motivated by the salt-driven reaction, we employed nickel(II) chloride ($NiCl_2$) in conjunction with sodium amide ($NaNH_2$) as the nitrogen source, leading to the complete reduction of Ni(II) to Ni(0). Following a similar approach to the Cu_3N reaction, we utilized nickel(II) nitrate ($Ni(NO_3)_2$) as the precursor along with OLAm, resulting in the formation of NiO, see Figure 3.13.

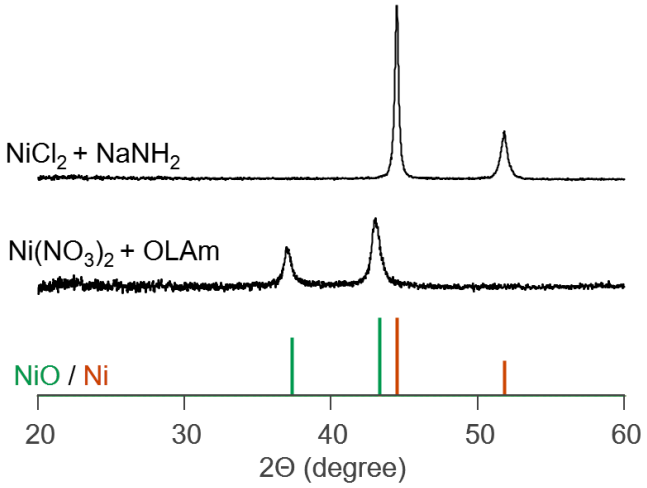

Figure 3.13 *p*XRD patterns of NiO synthesized via the reaction of $Ni(NO_3)_2$ with OLAm and Ni(0) synthesized through the reaction of $NiCl_2$ with $NaNH_2$ in the presence of OLAm as a ligand. The reactions were conducted at 260 °C for 10 minutes in hexadecane.

To produce Ni_3N, a solution containing purified Cu_3N was combined with $NiCl_2$ in either TOP or OLAm at a temperature of 50 °C. The resulting mixture was then subjected to a range of temperatures, varying from 100 °C to 260 °C, for 30 minutes. However, this process yielded only Ni(0), $Ni(NH_3)Cl_2$, and Cu/Ni alloys as the final products, see Figure 3.14. Table 3.2 summarizes all the attempts to produce Ni_3N.

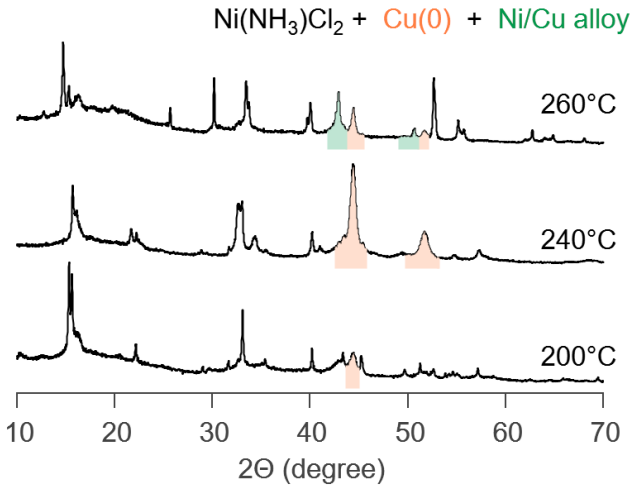

Figure 3.14 | *p*XRD patterns of the products obtained via reaction of $NiCl_2$ with Cu_3N at different temperatures.

Table 3.2 | Summary of Ni_3N synthesis attempt. The solvent for all these reactions was hexadecane with a reaction time of 10 minutes.

Metal prec.	Nitrogen Source	eq.	T °C	Product
$Ni(acetate)_2$	OLAm	2 eq.	210 °C	amorphous
$Ni(acetate)_2$	OLAm	31 eq.	210 °C	amorphous
$Ni(acetate)_2$	OLAm + $BnNH_2$	10 + 20 eq.	220 °C	Ni(0)
$Ni(acetate)_2$	OLAm + TMG	10 + 20 eq.	220 °C	Ni(0)
$Ni(acetate)_2$	$BnNH_2$	30 eq.	220 °C	no product
$NiCl_2$	OLAm + $NaNH_2$	10 + 20 eq.	240 °C	amorphous
$NiCl_2$	OLAm + $NaNH_2$	10 + 20 eq.	260 °C	Ni(0)
$Ni(NO_3)_2$	OLAm	31 eq.	240 °C	NiO
$Ni(NO_3)_2$	OLAm	31 eq.	260 °C	NiO
$Ni(NO_3)_2$	OLAm + $NaNH_2$	5 + 10 eq.	240 °C	NiO + Ni(0)
$Ni(NO_3)_2$	OLAm + $NaNH_2$	5 + 40 eq.	240 °C	Ni(0)

* OLAm= Oleylamine ; TMG = Tetramethylguanidine ; $BnNH_2$= Benzylamine

3.5 Conclusion

The previous section provided a brief overview of our unsuccessful attempts to obtain TiN, Zn_3N_2, and Ni_3N. In the case of TiN, the challenge lies primarily in the crystallization step, as the initial formation of Ti-N bonds seems to occur. To overcome this crystallization barrier, one possible approach is to increase the reaction temperature, which would necessitate the development of a new synthetic setup capable of handling higher temperatures. Regarding Zn_3N_2 and Ni_3N, most of the nitrogen sources we tested were found to be excessively reductive, resulting only in the formation of the corresponding metallic phases. Additionally, attempts to employ Cu_3N as a nitrogen source did not lead to the desired nitride formation and only resulted in the decomposition of Cu_3N. Thus far, our solution-based methods for synthesizing metal nitrides have been proven unsuccessful, suggesting that higher temperatures and/or elevated ammonia pressure may be necessary to achieve the desired outcomes.

References

[1] Hu, J.; Lu, Q.; Tang, K.; Yu, S.; Qian, Y.; Zhou, G.; Liu, X. Low-Temperature Synthesis of Nanocrystalline Titanium Nitride via a Benzene-Thermal Route. *Journal of the American Ceramic Society* **2004**, *83*, 430–432.

[2] Bradley, D. C.; Thomas, I. M. 765. Metallo-organic compounds containing metal–nitrogen bonds. Part I. Some dialkylamino-derivatives of titanium and zirconium. *Journal of the Chemical Society (Resumed)* **1960**, *0*, 3857–3861.

[3] Bradley, D. C.; Torrible, E. G. Metallo-Organic Compounds Containing Metal–Nitrogen Bonds: Part Iv. Some Bis-(Primary Amino)-Titanium Compounds. *Canadian Journal of Chemistry* **1963**, *41*, 134–138.

[4] Lorber, C.; Vendier, L. Novel aspects of the transamination reaction between $Ti(NMe_2)_4$ and primary amines. *Dalton Transactions* **2013**, *42*, 12203–12219.

[5] Jackson, A. W.; Hector, A. L. A nonoxidic sol–gel route to titanium nitride and carbonitride films by primary aminecondensation. *J. Mater. Chem.* **2007**, *17*, 1016–1022.

[6] Lorber, C.; Choukroun, R.; Vendier, L. A General and Facile One-Step Synthesis of Imido–Titanium(IV) Complexes: Application to the Synthesis of Compounds Containing Functionalized or Chiral Imido Ligands and Bimetallic Diimido Architectures. *European Journal of Inorganic Chemistry* **2006**, *2006*, 4503–4518.

[7] Adams, N.; Bigmore, H. R.; Blundell, T. L.; Boyd, C. L.; Dubberley, S. R.; Sealey, A. J.; Cowley, A. R.; Skinner, M. E. G.; Mountford, P. New Titanium

Imido Synthons: Syntheses and Supramolecular Structures. *Inorganic Chemistry* **2005**, *44*, 2882–2894.

[8] Egeberg, A.; Wenzel, O.; Popescu, R.; Gerthsen, D.; Feldmann, C. Pyridine-based Liquid-Phase Synthesis of Crystalline TiN and $ZnSiN_2$ Nanoparticles. *ChemistryOpen* **2020**, *10*, 334–339.

[9] Hiltunen, L.; Leskela, M.; Makela, M.; Niinisto, L.; Nykanen, E.; Soininen, P. Nitrides of titanium, niobium, tantalum and molybdenum grown as thin-films by the atomic layer epitaxy method. *Thin Solid Films* **1988**, *166*, 149–154.

[10] Parvizian, M.; Balsa, A. D.; Pokratath, R.; Kalha, C.; Lee, S.; den Eynden, D. V.; Ibáñez, M.; Regoutz, A.; Roo, J. D. The Chemistry of Cu_3N and Cu_3PdN Nanocrystals. *Angewandte Chemie International Edition* **2022**, *61*, e20220701–8.

[11] Garnweitner, G.; Goldenberg, L.; Sakhno, O.; Antonietti, M.; Niederberger, M.; Stumpe, J. Large-Scale Synthesis of Organophilic Zirconia Nanoparticles and their Application in Organic–Inorganic Nanocomposites for Efficient Volume Holography. *Small* **2007**, *3*, 1626–1632.

[12] Ho, C.-T.; Low, K.-B.; Klie, R. F.; Maeda, K.; Domen, K.; Meyer, R. J.; Snee, P. T. Synthesis and Characterization of Semiconductor Tantalum Nitride Nanoparticles. *Journal of Physical Chemistry C* **2010**, *115*, 647–652.

[13] Dunand, D. C.; Müllner, P. Size Effects on Magnetic Actuation in Ni-Mn-Ga Shape-Memory Alloys. *Advanced Materials* **2010**, *23*, 216–232.

[14] Taylor, P. N.; Schreuder, M. A.; Smeeton, T. M.; Grundy, A. J. D.; Dimmock, J. A. R.; Hooper, S. E.; Heffernan, J.; Kauer, M. Synthesis of widely tunable and highly luminescent zinc nitride nanocrystals. *J. Mater. Chem. C* **2014**, *2*, 4379–4382.

[15] Shanker, G. S.; Ogale, S. Faceted Colloidal Metallic Ni_3N Nanocrystals: Size-Controlled Solution-Phase Synthesis and Electrochemical Overall Water Splitting. *ACS Applied Energy Materials* **2021**, *4*, 2165–2173.

The joy of success is sweeter
when you've known the
bitterness of failure.

Anonymous

4 Molten Salt-Assisted Titanium Nitride Synthesis

4.1 State of the art

As mentioned in the introduction chapter, Giordano *et al.* presented the *urea glass route* as a pioneering pathway for the formation of nitrides through sol-gel techniques.[1] In this method, initially, $TiCl_4$ is dissolved in ethanol, forming titanium ethoxide and releasing HCl as side product. Then a varying amount of solid urea is added to the solution and stirred until complete dissolution and the solvent is allowed to evaporate. The metal center is mostly coordinated to urea via the carbonyl oxygen as shown by fourier-transform infrared spectroscopy (FT-IR) data. The gel was then heated under N_2 flow at 800 °C for 3 h at a very slow rate of 3 °C /min. A mechanism has been proposed based on thermogravimetric analysis (TGA) and x-ray powder diffraction (*p*XRD) analysis. First, a glassy intermediate with nanoscale anatase and rutile titania is formed at 400 °C. Second, at 600 °C, loss of oxygen and metal reduction/nitridation is observed. Higher temperatures (800 °C) are required to obtain complete recrystallization, see Figure 4.1.

‡**Adapted from**: Parvizian, M.; Pokratath, R.; Regoutz, A.; De Roo, J.; Efficient Synthesis of Group 4 Metal Nitrides at Low Temperatures with Molten Salts
Contributions: Parvizian, M. designed the syntheses setups, conducted them and characterized via XRD, DLS, UV-Vis, and analyzed the provided data. Pokratath, R. performed PDF analysis and Rietveld refinement. Regoutz, A. performed the XPS analysis.

A key parameter R has been defined as the ratio of urea and titanium. For R = 3, a mixture of TiN and TiO_2 is obtained. Pure TiN is retrieved for R = 4, while Ti(C,N) was formed for R = 10. The higher R, the higher the carbon contamination so the optimal ratio for TiN is four. The authors expanded the procedure to many other metal nitrides (VN, NbN, GaN, CrN, Mo_2N), but each metal has another optimal value for R.[1]

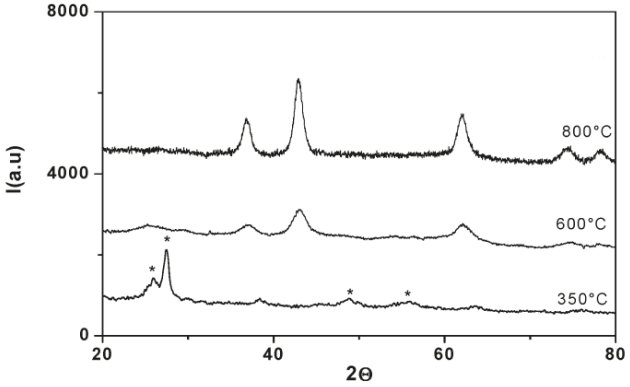

Figure 4.1 X-ray powder diffraction (*p*XRD) pattern of titanium-urea gels (R=10) treated at different temperatures. The * symbol refers to crystalline TiO_2. Reprinted with permission from.[1] Copyright 2009 American Chemical Society.

Later, the method was also applied to produce Sn_3N_4,[2] HfN,[3] and ZrN[4] as well as other nanocomposites such as graphene g−C_3N_4 doped with TiN.[5;6] The nitride nanocrystals (NCs) obtained via this process are typically aggregated powders. Finally, other nitrogen sources were explored such as guanidine carbonate and barbituric acid. However, both feature a particularly low solubility and it was not possible to achieve R > 1.[1]

An alternative method for nitride formation is through the solid-state route, which requires heating a mixture of solid materials at high temperatures to generate a new solid composition. These reactions typically require temperatures above 1000 °C and a significant amount of time for the reaction to occur. One of the main challenges of this process is achieving thorough mixing of the reactants. Manual mixing using an

agate mortar and pestle is suitable for small quantities (below 20 g), while ball milling is preferred for larger quantities.[7] The slow nature of solid state reactions is attributed to the limited interaction between the reactants at the atomic level.

Previous studies on TiN syntheses involved autoclave reactions using $TiCl_4$ with various nitrogen sources, including NaN_3,[8] $NaNH_2$[9;10] and NH_4Cl[11]. These reactions required temperatures ranging from 300 °C to 500 °C. The resulting products were all aggregated, some contained oxygen, and none exhibited plasmonic properties. Another study reported the autoclave synthesis of TiN at 550 °C using $NaNH_2$ as the nitrogen source and TiO_2 as the titanium source. Similarly, the final particles were aggregated and lacked plasmonic properties.[12]

In 2019, Dasog and coworkers synthesized plasmonic TiN, ZrN, and HfN NCs from their parent oxide using 3 equivalents of Mg_3N_2 as the nitrogen source.[13] Their strategy consists of a high temperature (1000 °C) solid-state metathesis reaction with commercial TiO_2 (17 nm), ZrO_2 (19 nm), and HfO_2 (43 nm). These reactions are thermodynamically favorable with ΔH_{rxn}=-286 kJ/mol due to MgO formation, see the balanced reaction equation 4.1.

$$6\ TiO_2 + 4\ Mg_3N_2 \xrightarrow[\text{Ar flow}]{1000\ ^\circ\text{C, 1 h}} 6\ TiN + 12\ MgO + N_2 \tag{4.1}$$

The final product is treated with 1M HCl to remove MgO and unreacted Mg_3N_2 and could be dispersed in water.[13] All compounds have the expected cubic crystal structure and the NC size is 12, 15, and 11 nm for TiN, ZrN, and HfN respectively. The NCs appear aggregated on transmission electron microscopy (TEM). Attempts to significantly increase the particle size by using larger oxide NCs were unsuccessful, suggesting new nucleation events of the nitride rather than simple anion exchange. The localized surface plasmon resonance of the NCs is blue-shifted and narrower in the series: TiN, ZrN and HfN (Figure 4.2b). Finally, all particles were slightly oxidized at the surface and this effect was worse for ZrN and HfN compared to TiN. This scalable strategy of Dasog *et al.* seems to produce high quality group 4 nitrides. The method has already been

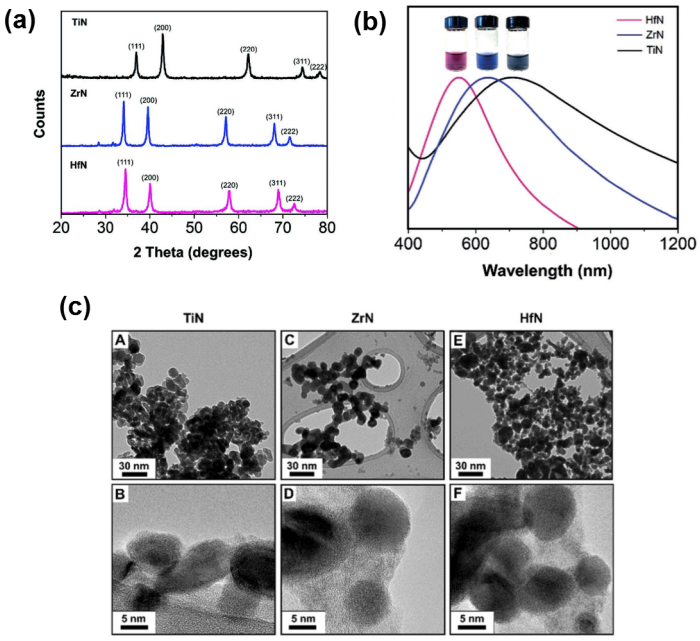

Figure 4.2 (a)*p*XRD patterns, (b) Absorption spectra of aqueous dispersions and (c) TEM images of TiN, ZrN and HfN particles obtained via metathesis as reported by Karaballi *et al.*. Reprinted from ref[13] with permission from John Wiley and Sons, Copyright 2019.

adopted by other groups to produce, for example, plasmonic HfN NCs.[14]

Molten salts are a material class that is solid at standard temperatures and pressure and becomes a liquid at elevated temperatures. These salts are the solvent of choice for solution based chemistry at high temperatures (above 300 °C). These solvents offer better solvation of inorganic materials due to a strong polarization force formed upon the melting of the salts at high temperatures. Molten salts provide a higher reactivity as compared to a standard solid state reaction due to convection diffusion and faster mass transport which results in lowering the overall reaction temperatures.[15;16] These salts are usually used as an eutectic mixture meaning a homogenous mixture that melts or solidifies at a single temperature that is lower than the melting point of any of the constituents. Some of the commonly used eutectic salts are the chloride salts (LiCl, KCl, NaCl, $MgCl_2$), nitrates salts ($LiNO_3$, $NaNO_3$, KNO_3), sulfate (Na_2SO_4, K_2SO_4)

and fluoride slats (NaF, KF, LiF). Molten salts provide colloidal stability for inorganic NCs when there is a chemical affinity between the surface of the NCs and the ions based on their Lewis acidity.

This colloidal stability follows a different stabilization mechanism than the electrostatic or steric approach. Colloidal stability in molten salts is mainly due to long-range charge density oscillations formed at the solute-solvent (molten salt) interface. This oscillation prevents the particles from aggregating and its strength is proportional to the strength of the chemical bond between the solute and the molten salts. The molten salts should therefore be carefully selected to have a high chemical affinity with the solute.[17;18] Numerous syntheses processes can be performed within molten salt environments, encompassing binary oxides like Al_2O_3,[19] ZrO_2[20] and Co_3O_4,[21] ternary and multinary oxides such as perovskites,[22–24] as well as boride,[25] nitride,[26] carbide[27] formations, and high-temperature ligand exchange reactions.[28;29]

Kan *et al.* explored molten salts (here: a eutectic mixture of $MgCl_2$ and NaCl) as a reaction medium for the synthesis of TiN from TiO_2 and Mg powder under N_2 atmosphere. The use of a higher Mg equivalent versus TiO_2 (up to 4 equivalents), higher heating temperature (up to 1100 °C), or longer reaction time (up to 7 h) leads to phase pure TiN with a better crystallinity as judged by the well-defined diffraction peaks obtained by *p*XRD. Remarkably, the formation of TiN could already be detected at a relatively low temperature of 600 °C, as evidenced by the diffraction patterns observed. The authors obtained 5–30 nm aggregated TiN NCs by using 2.5 equivalents of Mg heated at 1100 °C for 3 h. The authors described the mechanism as being a dissolution-precipitation type based on the increase of the surface area from the starting TiO_2 (9.83 m^2/g) to the obtained TiN (93.09 m^2/g), see Figure 4.3).[30]

The synthesis of three-dimensional porous metal nitrides like vanadium(III) nitride, molybdenum(III) nitride, tungsten(III) nitride, and titanium(III) nitride has been recently reported. This synthesis was achieved using a molten salts method that involved a mixture of anhydrous $ZnCl_2$ and $ZnCl_2.6H_2O$, along with the respective MCl_3 and Li_3N as the nitrogen source. The authors claim that using $ZnCl_2$ molten salt system reduces

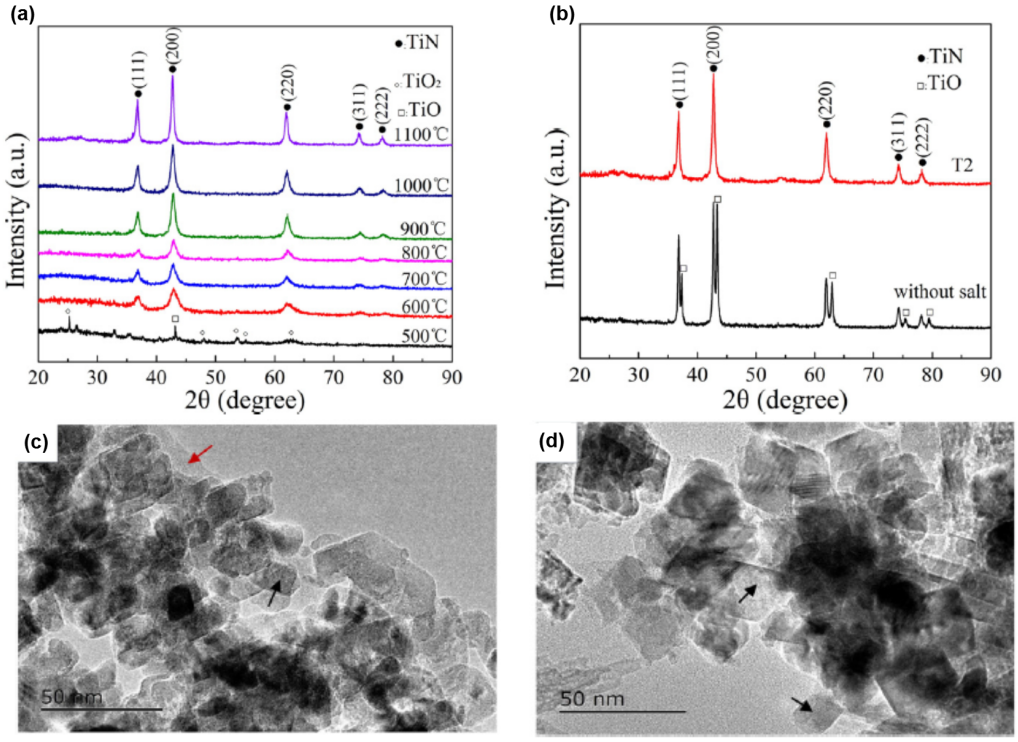

Figure 4.3 *p*XRD patterns of TiN synthesized at (a) 500–1100 °C for 3 h, (b) with and without molten salts at 1100 °C for 3 h, and TEM images of TiN obtained after 3 h reaction at (c) 1000 °C and (d) 1100 °C as reported by Kan *et al.*. Reprinted from ref[30] with permission from Elsevier, Copyright 2017.

the reaction temperature as compared to NaCl molten salts and that the presence of a controlled amount of crystalline water allows the formation of a ZnO 3D porous template which after acid treatment results in pure 3D porous metal nitride.[26]

In this study, our primary objective is to develop new synthetic procedures using molten salts with the aim of producing phase-pure TiN NCs at lower temperatures (below 800 °C), while preserving high crystallinity. It is important to highlight that our study builds upon the groundwork laid by Karaballi *et al.*, who previously uncovered intriguing plasmonic behavior in analogous systems. To achieve our objective, we systematically explore various parameters that can be adjusted, including the choice of molten salts, different ratios, the use of reducing agents, the nitrogen source, and pu-

rification methods with TiO_2 as our titanium source. Through an extensive screening process, we successfully managed to significantly reduce the reaction temperature to as low as 350 °C. Subsequently, we conducted a thorough investigation of the resulting particles using x-ray photoelectron spectroscopy (XPS) and Rietveld refinement.

4.2 Experimental section

Materials

The precursors employed in the synthesis included commercially available titanium(IV) oxide nanopowder (TiO_2, 21 nm , ≥99.5% trace metals basis, Sigma), magnesium(II) nitride cubic phase (M_3N_2,-325 mesh, ≥99.5%, Sigma), calcium(II) nitride (Ca_3N_2,-200 mesh, 99% , Sigma), magnesium powder (Mg, ≥99%, Sigma), anhydrous zinc(II) chloride ($ZnCl_2$, ≥97%, Sigma), and lithium chloride (LiCl,99%, Strem). In other reported reactions, sodium amide ($NaNH_2$, 98%, Sigma), lithium nitride (Li_3N,-80 mesh, ≥99.5%, Sigma), lithium bromide anhydrous (LiBr,99+%, Strem), and potassium bromide (KBr, 99%, Sigma) were utilized. All these precursors were stored within a nitrogen-filled glovebox to prevent exposure to moisture. Subsequently, for purification purposes, the following reagents were used: distilled water, absolute ethanol, acetone, chloroform, cyclohexane, acetic acid (CH_3CO_2H,>99%, Sigma), and oleic acid ($C_{18}H_{34}O_2$, 90%, Sigma).

Syntheses without molten salts

This synthesis procedure is adapted from a method previously outlined by Karaballi *et al.*.[13] In a nitrogen-filled glovebox, 100 mg of the commercially available TiO_2 nanopowder (1.25 mmol, 1 eq.) was combined with 3 eq. of a Mg_3N_2 powder (3.75 mmol, 378 mg) as the nitrogen source. This mixture was blended using an agate mortar and pestle for 10 minutes, yielding a fine homogeneous powder. The resulting blend was then transferred to an aluminum oxide combustion boat and swiftly positioned inside a quartz tube within a Nabertherm N7/H tube furnace filled with argon. The mixture

underwent heating at 1000 °C for 12 h (rate of 13 °C /minute) with an argon flow.

Following the reaction, once the oven had cooled, the particles were dispersed in 40 mL of water and agitated with 3 mL of acetic acid at 50 °C for 48 h. After this acid treatment, the particles required four rounds of washing and centrifugation with water to eliminate the acetate side products. In each round, the particles are dispersed in 30 mL of water and centrifuged at 5'000 rcf for 4 minutes. Visual differentiation between the nitride product and grey-colored acetate side products guided this step.

Subsequently, the particles were stabilized using an organic ligand, oleic acid (OA). The particles were once again dispersed in 40 mL of water, and mix with 2 mL of OA and 20 mL of cyclohexane, stirred vigorously for 2 h at 50 °C. Subsequently, the particles were collected from the cyclohexane phase. If the phase separation was not distinctly evident, the mixture of water and cyclohexane underwent centrifugation at 500 rcf for 4 minutes, facilitating a more pronounced phase separation. The NCs were then precipitated with 40 mL of acetone and centrifugated at 5'000 rcf for 4 minutes. The resulting precipitate was dispersed in 10 mL chloroform to which 200 μL of OA was added, followed by 15 minutes of sonication. The particles were precipitated using 30 mL of acetone and centrifuged at 5'000 rcf for 4 minutes. This process of stabilization involving 200 µL of OA in chloroform, followed by acetone purification, was repeated. The final outcome was a suspension of TiN capped with OA in 5 mL of chloroform. Each of these steps played a pivotal role in achieving a phase-pure and stable end product.

Syntheses with molten salts

In a nitrogen-filled glovebox, 100 mg of the commercially available TiO_2 nano-powder (1.25 mmol, 1 eq.) was combined with 3 eq. of a nitrogen source Mg_3N_2 (3.75 mmol, 378 mg) or Ca_3N_2 (3.75 mmol, 555 mg) with 2 eq. of magnesium powder (2.50 mmol, 60 mg) acting as a reducing agent. This mixture was blended with an eutectic combination of $ZnCl_2$ (500 mg, 78 mol%) and LiCl (44 mg, 22 mol%) using an agate mortar and pestle for 10 minutes, yielding a fine homogeneous powder. The resulting blend was then transferred to an aluminum oxide combustion boat and swiftly positioned inside

a quartz tube within a Nabertherm N7/H tube furnace filled with argon. The mixture underwent heating at different temperatures ranging from 350–600 °C for 12 h (rate of 13 °C /minute) with an argon flow. After the reaction, upon the cooling of the oven, the resulting powder was washed using water as a high dielectric constant polar solvent. Four rounds of centrifugation with 30 mL water at 5'000 rcf for 4 min were necessary to eliminate most of the salts. Subsequently, the particles were dispersed in 40 mL water and agitated with 3 mL of acetic acid at 50 °C for 48 h. The subsequent purification steps followed the aforementioned procedure.

Instrumentation

Dynamic light scattering (DLS) measurements were conducted on a Malvern Zetasizer Ultra in backscattering mode (173 °) in a glass cuvette. All measurements were performed at 25 °C after equilibrating the system for 240 seconds, sample concentration was tuned to achieve system attenuator values between 9–10. *p*XRD spectra were measured using a STOE StadiP powder diffractometer with a Dectris Mythen 1K detector and a micro-focused Cu-Kα-source (λ=1.542 Å). In the *p*XRD analysis, 4 mg of each purified product was weighed alongside 2 mg of silicon (33 m%), which served as an internal reference. The silicon's intensity was normalized, enabling a direct comparison of diffraction intensities among the products derived from various syntheses.

4.3 Results and discussion

Choice of molten salts

In light of the research conducted by Karaballi *et al.*, we opted to initiate our study using TiO_2 as our source of titanium and Mg_3N_2 as the nitrogen source with a reaction time of 12 h. Our objective was to maintain crystallinity while reducing the reaction temperature. To achieve this, we followed the approach proposed by Kan *et al.*, which involved the use of an external reducing agent, magnesium, together with molten salts. A reaction temperature of 600 °C was chosen because it is the lowest temperature at

which crystalline TiN has been reported so far, see Equation 4.2.

$$TiO_2 + 3\ Mg_3N_2 + 2\ Mg \xrightarrow[\text{molten salts}]{600\ ^\circ\text{C, 12 h}} TiN + MgO + \text{by}-\text{products} \tag{4.2}$$

While choosing our molten salts combination, first all combinations that would contain oxygen were eliminated to avoid any metal oxide formation. Among the remaining combinations the eutectic combinations that would have a decomposition temperature below our reaction temperatures such as aluminum ($AlCl_3$–NaCl–KCl) and thiocyanate (KSCN–NaSCN) were discarded. The alkali combinations (LiCl–LiBr–KBr) and zinc ($ZnCl_2$–LiCl) were chosen for the reaction. Table 4.1 presents a summary of the various eutectic combinations and their respective melting points. As depicted in Figure 4.4, the utilization of molten salts plays a pivotal role in significantly reducing the reaction temperature, lowering it from 1000 °C to 600 °C. In contrast, when the reaction is conducted at 600 °C without the presence of molten salts, an oxy-nitride phase forms. However, when molten salts are introduced, complete conversion of the oxide to nitride occurs, resulting in phase-pure TiN. When assessing various sets of molten salts, it became evident that the reaction involving zinc molten salts exhibited superior crystallinity and yielded a purer TiN phase when compared to the alkali-based sets after 12 h of reaction at 600 °C. This outcome may be attributed to the Lewis acidity of $ZnCl_2$, which enhances the solvation and activation of TiO_2, thereby promoting the formation of nitrides (Figure 4.4).

Table 4.1 The different sets of eutectic molten salts considered for our reaction with their corresponding melting temperatures.

Molten salts	**Melting point** (°C)	**mol.%**
LiCl/LiBr/KBr	320	25:37:38
NaSCN/KSCN	140	26.3:73.7
$AlCl_3$/NaCl/KCl	90	63.5:20:16.5
$ZnCl_2$/LiCl	280	78:22

The concentration of titanium in the molten salts was varied by changing the molar ratio of TiO_2 to $ZnCl_2$ from 1 to 12 equivalents. Utilizing a silicon internal standard in

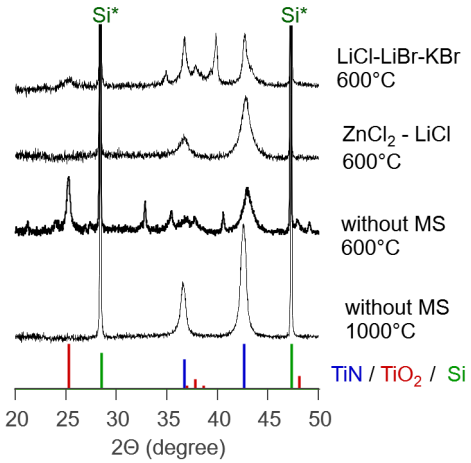

Figure 4.4 *p*XRD results of the purified product obtained from reactions of 1 eq. TiO_2 with 3 eq. Mg_3N_2 for 12 h with and without molten salts at 1000 °C or 600 °C. In the molten salt-assisted reaction, Mg was used as a precursor in the reaction, acting as a reducing agent. References of TiN, TiO_2, and silicon are indicated in blue, red, and green respectively. The diffractions were normalized to silicon internal reference.

the *p*XRD measurement, as detailed in the experimental section, revealed that a ratio of 1:1 (titanium molality of 6.8 mol/Kg) does not result in full TiN formation while 12 equivalents (titanium molality of 0.57 mol/Kg) results in a side phase impurity. A 1:3 molar ratio of TiO_2 versus $ZnCl_2$ (titanium molality of 2.3 mol/Kg) appears to give the best results, yielding pure TiN phase (Figure 4.5).

Choice of nitrogen source and reducing agent

Various nitrogen sources were explored for the molten salt reaction, including Li_3N, $NaNH_2$, Mg_3N_2, and Ca_3N_2. While phase-pure TiN was not obtained with Li_3N and $NaNH_2$ (Figure A.10), phase purity was achieved with the others after purification. Notably, the use of Ca_3N_2 produced TiN with crystallinity similar to literature reports but at a lower temperature (600 °C instead of 1000 °C). Simultaneously, employing Mg_3N_2 at 600 °C resulted in a broader and slightly shifted diffraction, indicating some oxygen content. For a comprehensive perspective, both an overview figure with silicon

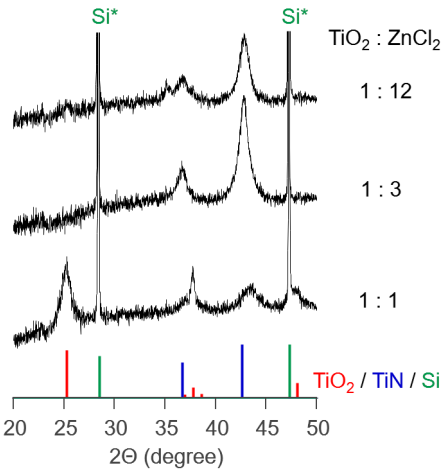

Figure 4.5 *p*XRD patterns of products obtained by varying the $ZnCl_2$ to TiO_2 molar ratio at 600 °C for 12 h. Mg_3N_2 served as the nitrogen source with Mg as the reducing agent. The eutectic molten salt mixture consisted of 78 mol% $ZnCl_2$ and 22 mol% LiCl. References of TiN, TiO_2, and silicon are indicated in blue, red, and green respectively. The diffractions were normalized to silicon internal reference.

normalization and a magnified version highlighting the region of interest are presented (Figure 4.6). Despite the broader diffraction observed for the Mg_3N_2 sample, both products obtained at 600 °C with Mg_3N_2 and Ca_3N_2 exhibit similar large hydrodynamic diameters and sizes, as determined by analysis using DLS and SEM, see Figures A.11 and A.12.

Remarkably, when TiO_2 was subjected to a 12 h reaction with Ca_3N_2 in the absence of any molten salts, the result was a phase-pure TiO_2 product without the formation of any nitrides. The initial TiO_2 used in this study was a commercially available material containing a mixture of anatase and rutile with very sharp diffraction patterns. However, the end product of this reaction exhibited broad diffraction patterns associated with anatase (Figure A.13).

Both nitrogen sources were evaluated across a temperature range of 350 to 600 °C. When employing Mg_3N_2 as the nitrogen source, the diffraction peak broadened considerably, making it challenging to attribute it solely to TiN, with the additional detection

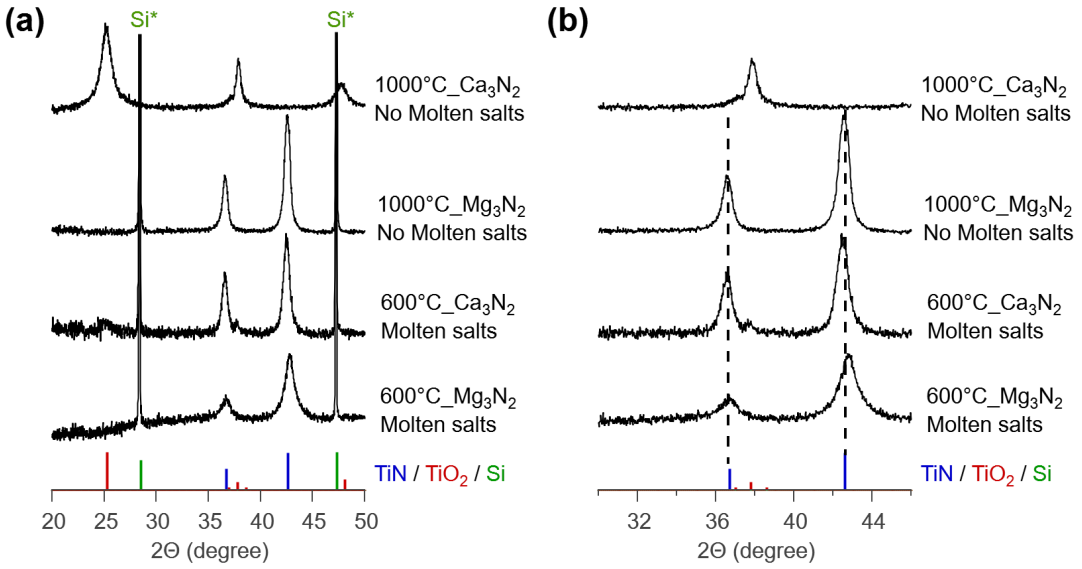

Figure 4.6 *p*XRD patterns for 12 h reactions of TiO_2 with Mg_3N_2 or Ca_3N_2 at 600 °C or 1000 °C , with or without molten salts. (a) Overview and (b) magnified view. Ca_3N_2-derived particles at 600 °C exhibit superior crystallinity compared to Mg_3N_2. The molten salt-assisted reaction used Mg as a reducing agent. References of TiN, TiO_2, and silicon are indicated in blue, red, and green respectively. The diffractions were normalized to silicon internal reference.

of impurities. On the other hand, when we used Ca_3N_2, the diffraction peaks remained sharp and consistent over the entire temperature range from 350 to 600 °C. Consequently, we selected Ca_3N_2 as the primary nitrogen source for further investigation. This choice led to a significant reduction in reaction temperature, all while maintaining crystallinity comparable to that reported by Karaballi *et al.* at 1000 °C, or as indicated by Giordano *et al.* at temperatures as high as 800 °C.[1;13] It is noteworthy that when using Ca_3N_2 as the nitrogen source, some TiO_2 impurities were detected, although these decreased with a reduction in reaction temperature, see Figure 4.7. Efforts were made to avoid TiO_2 impurities and attain a pure TiN product.

Initially, a combination of Mg_3N_2 and Ca_3N_2 was explored as nitrogen sources, but this approach led to the formation of additional TiO_2 side products, as demonstrated

in Figure A.14. Subsequently, an attempt was made to mitigate this issue by reducing the titanium concentration, with 5 equivalents of $ZnCl_2$ used instead of the original 3 equivalents. Unfortunately, this adjustment also resulted in the formation of unwanted side phases (Figure A.15). Moreover, increasing the equivalent amount of Ca_3N_2 to 5 eq. from 3 eq. in comparison to TiO_2 did not yield any significant alteration in the final phase purity (Figure A.16).

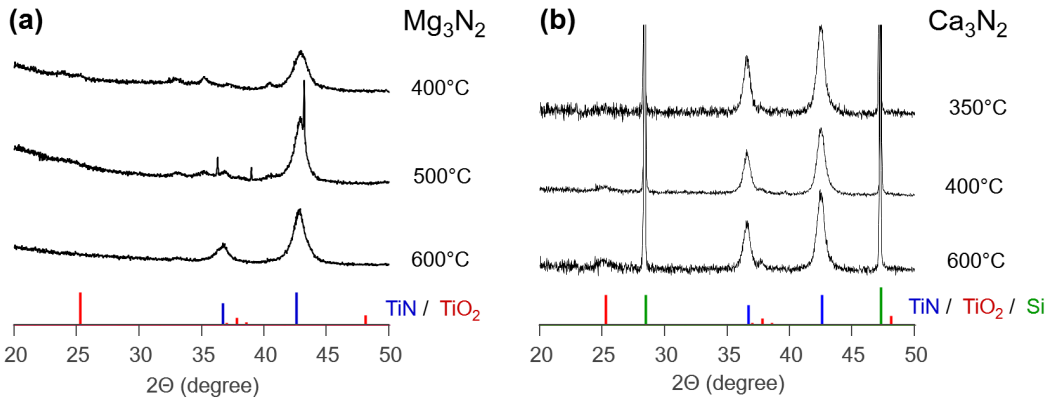

Figure 4.7 *p*XRD patterns of the final product obtained at various reaction temperatures using (a) Mg_3N_2 and (b) Ca_3N_2 as nitrogen sources. The syntheses were conducted for 12 h in a eutectic mixture of $ZnCl_2$-LiCl as the molten salt, with magnesium as the reducing agent and TiO_2 as the titanium precursor. References of TiN, TiO_2, and silicon are indicated in blue, red, and green respectively. The diffractions in spectra (b) were normalized to silicon internal reference.

Magnesium served as the reducing agent in all the experiments, aimed at improving the reduction of Ti(IV) and facilitating TiN formation. The inclusion of 2 equivalents of magnesium in conjunction with 3 equivalents of Ca_3N_2, as opposed to TiO_2, led to an increase in phase purity, as indicated by the reduced TiO_2 content after purification. This enhancement was particularly pronounced at lower temperatures (Figure A.17). However, substituting magnesium for more Ca_3N_2 resulted in the undesirable formation of side phase impurities (Figure 4.8).

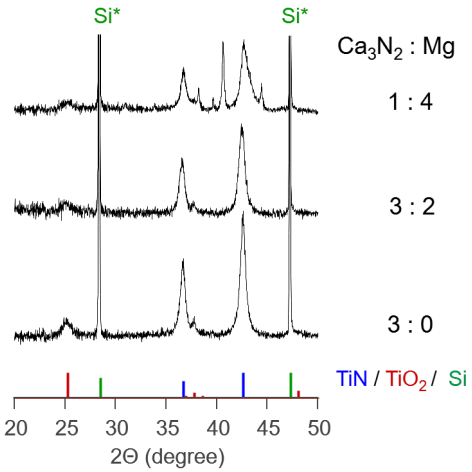

Figure 4.8 *p*XRD pattern of the product obtained with and without the use of magnesium as a reducing agent at 600 °C for 12 h. References of TiN, TiO_2, and silicon are indicated in blue, red, and green respectively. The diffractions in spectra (b) were normalized to silicon internal reference.

Purification

Following the reaction, the resulting powder undergoes multiple rounds of washing with water, followed by centrifugation to eliminate the salts. The particles are subjected to an acid treatment with acetic acid, followed by multiple water washes to remove any by-products. Next, the particles are stabilized using OA through dispersion in cyclohexane, followed by centrifugation and dispersion in chloroform with sonication. The final product is a suspension of TiN capped with OA, achieved through crucial sequential steps. Colloidal stability is highly dependent on particle size. In this type of solid state reaction, the final products are still aggregated and have an average solvodynamic diameter of over 100 nm, so long-term colloidal stability cannot be expected (Figure A.11). However, we believe that such treatment would produce a solution stable enough for successive drop casting onto different substrates.

4.4 Comprehensive structural analysis

Characterization of synthesized TiN NCs was conducted through *p*XRD, as illustrated in Figure 4.9. The (111), (200), and (220) reflections exhibited precise correspondence with TiN patterns. Nonetheless, a minor presence of TiO_2 impurities was discerned in the newly optimized molten salt assisted approach, with impurity peaks aligning with the simulated pattern of TiO_2-anatase. The acid treatment effectively eliminated other side products, notably MgO, generated during the reaction. Both TiN and MgO share a halite-like rock salt structure, crystallizing in the cubic Fm-3m space group. Due to their comparable lattice parameters, the *p*XRD patterns displayed notable similarities. To verify the absence of MgO impurities in the purified samples, a comparative assessment was performed by contrasting the simulated *p*XRD pattern of MgO with that of the actual samples, focusing on relative peak intensities. Given the complexities of the analysis, the approach of Rietveld refinement was chosen.

The Rietveld analysis revealed that the sample obtained through the previously documented method (1000 °C without molten salts) possesses a cubic (Fm-3m) structure with titanium vacancies. The refined titanium occupancy (0.7) closely aligns with the structure reported in the literature.[31] Similarly, samples obtained at 600 °C and 350 °C using Ca_3N_2 as the nitrogen source and molten salts as our solvent exhibited the same phase characterized by titanium vacancies, measuring 0.74 and 0.78, respectively. Notably, at 600 °C , an approximate 10% proportion of the TiO_2-anatase phase was detected in the sample. However, obtaining a good fit for the product of the 350 °C reaction has proven challenging, as we believe the content is low and results in overestimation in all fits that have been attempted. An estimation suggests a content below 5% of TiO_2-anatase, making it nearly undetectable using copper source x-ray. The refined parameters are presented in Figure A.18, while detailed results are provided in Table A.3.

X-ray photoelectron spectroscopy (XPS) was employed to investigate the surface chemistry of the specimens produced using various synthetic approaches. The overview spectra reveal the consistent presence of titanium, nitrogen, oxygen, and carbon across

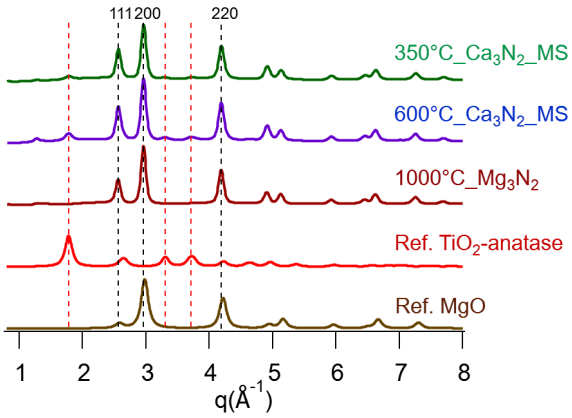

Figure 4.9 Experimental *p*XRD patterns of synthesized TiN NCs after a 12 h reaction at 350 °C and 600 °C with molten salts, and at 1000 °C without molten salts. Simulated patterns of TiO_2-anatase and MgO are provided for comparative analysis.

all samples. Magnesium was detected in all cases where it was utilized, either in the form of Mg_3N_2 or as an additional reducing agent. Zinc, however, was largely absent. Intriguingly, traces of fluoride elements were identified in nearly all samples, irrespective of the synthesis conditions, likely originating from the crucible (Figure A.19).

The Ti_{2P} core level spectra reveal a mixture of titanium oxidation states and chemical environments across all sample conditions, indicating partial oxidation. Specifically, samples obtained at 600 °C with Ca_3N_2 exhibit a characteristic Ti-N environment at lower binding energy (BE) (454 eV) along with $Ti^{4+}O_2$ at 459 eV, while the 1000 °C sample displays $Ti_2^{3+}O_3$ at 457 eV, corresponding to oxygen intercalation alongside Ti-N and $Ti^{4+}O_2$ signals. The 600 °C sample with Mg_3N_2 falls between these two scenarios. It is important to note that the Ti-N signal is more pronounced in the 1000 °C sample. However, given that XPS primarily analyzes surface properties, and our particles are larger than 100 nm, the signals likely originate from the surface layers. To validate this, we attempted to analyze the core's chemical environment using higher-energy X-rays. Indeed, this analysis revealed a rise in the Ti-N peak within the deeper layers. However, Ti-O signal was still detected in the samples obtained through molten salt, which could

potentially originate from the traces of TiO_2 side phase (Figure 4.10).

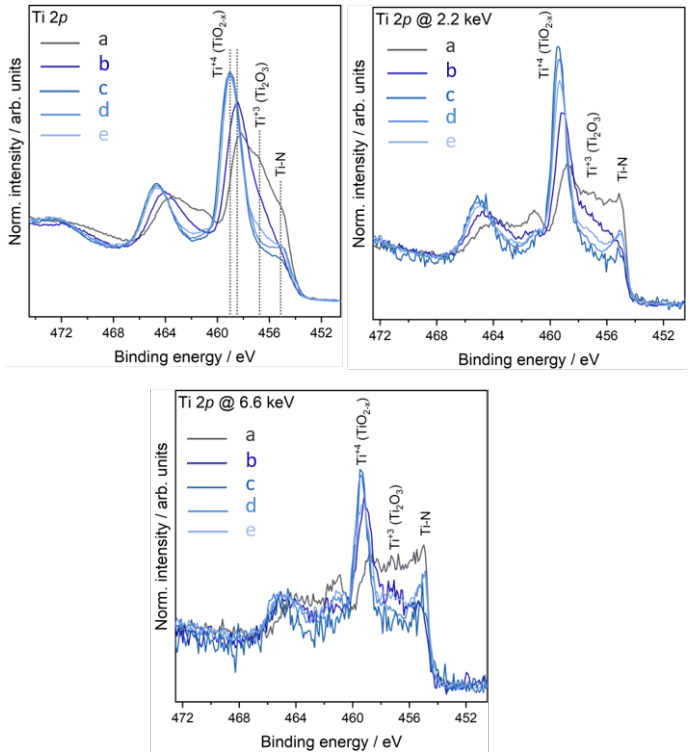

Figure 4.10 XPS core level spectra of Ti_{2P} at various x-ray energy from different samples: (a) 1000 °C without molten salts, (b) 600 °C with molten salts, using Mg_3N_2 as the nitrogen source and Mg as the reducing agent, (c) 600 °C with molten salts, using Ca_3N_2 as the nitrogen source and Mg as the reducing agent, (d) 600 °C with molten salts, using Ca_3N_2 as the nitrogen source without Mg, and (e) 350 °C with molten salts, using Ca_3N_2 as the nitrogen source and Mg as the reducing agent.

In all samples, the N_{1s} core level exhibits three distinct low BE features. One is associated with Ti-N at 397 eV, while a minor signal arises from NH_x at 399 eV. However, the origin of the feature at a lower BE of 396 eV remains uncertain. One hypothesis is that it may be related to whether the nitride configurations are directly connected to the biding carboxylate group, potentially causing a chemical shift (Figure 4.11). Interestingly, this signal, along with the NH_x feature, appears to diminish with higher X-ray energy usage, indicating it may be a surface-related characteristic (Figure A.20). Regarding the O_{1s}

core level, it demonstrates two different BE across all samples. The lower one at 530 eV corresponds to Ti-O, whereas the higher BE at 532 eV aligns with COO environments originating from oleic acid (OA) as the ligand (Figure 4.11).

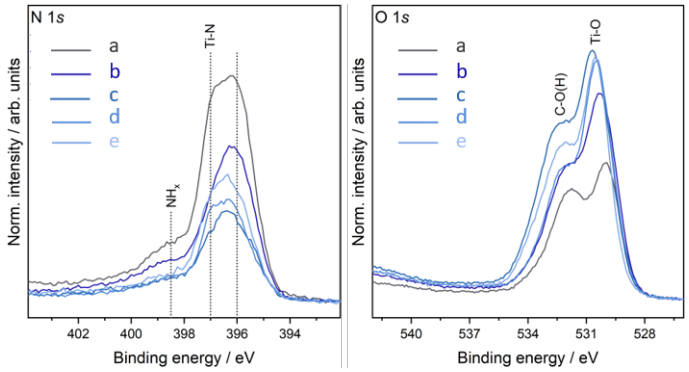

Figure 4.11 XPS core level spectra of N_{1s} and O_{1s} from the following samples: (a) 1000 °C without molten salts, (b) 600 °C with molten salts, using Mg_3N_2 as the nitrogen source and Mg as the reducing agent, (c) 600 °C with molten salts, using Ca_3N_2 as the nitrogen source and Mg as the reducing agent, (d) 600 °C with molten salts, using Ca_3N_2 as the nitrogen source without Mg, and (e) 350 °C with molten salts, using Ca_3N_2 as the nitrogen source and Mg as the reducing agent.

4.5 Conclusion

In conclusion, we successfully synthesized highly crystalline TiN particles at remarkably low temperatures, as low as 350 °C , employing a molten salt strategy. To the best of our knowledge, this marks the first instance of highly crystalline particles being reported at much reduced temperatures. Various parameters were meticulously adjusted, including the selection of molten salts, the nitrogen precursor, and the addition of magnesium as a reducing agent, all contributing to achieving these lower temperatures.

The most effective combination that enabled us to achieve this significant temperature reduction involved using a $ZnCl_2$-LiCl eutectic mixture as our molten salts, employing Ca_3N_2 as the nitrogen source, along with magnesium. When Ca_3N_2 was utilized as the nitrogen source, some TiO_2 side phases were detected. These side phases appeared to diminish notably as the temperature was lowered from 600 °C to 350 °C . Additionally, XPS analysis provided valuable insights into the surface chemistry of our particles. Surface oxidation, primarily in the form of TiO_2, was observed. Notably, this surface oxidation appeared to decrease substantially when exploring the core of our materials. We think this layer helps keep our particles stable in the open air, even when they encounter oxygen and water. These findings are paving the way for more research on making metal nitrides at lower temperatures.

References

[1] Giordano, C.; Erpen, C.; Yao, W. T.; Milke, B.; Antonietti, M. Metal Nitride and Metal Carbide Nanoparticles by a Soft Urea Pathway. *Chemistry of Materials* **2009**, *21*, 5136–5144.

[2] Qu, F. D.; Yuan, Y.; Yang, M. H. Programmed Synthesis of Sn3N4 Nanoparticles via a Soft Chemistry Approach with Urea: Application for Ethanol Vapor Sensing. *Chemistry of Materials* **2017**, *29*, 969–974.

[3] Defilippi, C.; Shinde, D. V.; Dang, Z.; Manna, L.; Hardacre, C.; Greer, A. J.; D'Agostino, C.; Giordano, C. HfN Nanoparticles: An Unexplored Catalyst for the Electrocatalytic Oxygen Evolution Reaction. *Angewandte Chemie International Edition* **2019**, *58*, 15464–15470.

[4] Yuan, Y.; Wang, J.; Adimi, S.; Shen, H.; Thomas, T.; Ma, R.; Attfield, J. P.; Yang, M. Zirconium nitride catalysts surpass platinum for oxygen reduction. *Nature Materials* **2019**, *19*, 282–286.

[5] Shanker, G. S.; Bhosale, R.; Ogale, S.; Nag, A. 2D Nanocomposite of g-C_3N_4 and TiN Embedded N-Doped Graphene for Photoelectrochemical Reduction of Water Using Sunlight. *Advanced Materials Interfaces* **2018**, *5*, 1801488.

[6] Shanker, G. S.; Markad, G. B.; Jagadeeswararao, M.; Bansode, U.; Nag, A. Colloidal Nanocomposite of TiN and N-Doped Few-Layer Graphene for Plasmonics and Electrocatalysis. *American Chemical Society Energy Letters* **2017**, *2*, 2251–2256.

[7] West, A. R. *Solid State Chemistry and its Applications*; Wiley, 2014.

[8] Yang, X.; Li, C.; Yang, B.; Wang, W.; Qian, Y. Optical properties of titanium oxynitride nanocrystals synthesized via a thermal liquid–solid metathesis reaction. *Chemical Physics Letters* **2004**, *383*, 502–506.

[9] Guo, Q.; Xie, Y.; Wang, X.; Lv, S.; Hou, T.; Bai, C. Synthesis of Uniform Titanium Nitride Nanocrystalline Powders via a Reduction-Hydrogenation-Dehydrogenation-Nitridation Route. *Journal of the American Ceramic Society* **2004**, *88*, 249–251.

[10] Feng, X.; Bai, Y.-J.; Lü, B.; Wang, C.-G.; Qi, Y.-X.; Liu, Y.-X.; Geng, G.-L.; Li, Low Temperature Induced Synthesis of TiN Nanocrystals. *Inorganic Chemistry* **2004**, *43*, 3558–3560.

[11] Yang, X.; Li, C.; Yang, L.; Yan, Y.; Qian, Y. Reduction-Nitridation Synthesis of Titanium Nitride Nanocrystals. *Journal of the American Ceramic Society* **2003**, *86*, 206–208.

[12] Huang, Y.; Gu, Y.; Zheng, M.; Xu, Z.; Zeng, W.; Liu, Y. Synthesis of nanocrystalline titanium nitride by reacting titanium dioxide with sodium amide. *Materials Letters* **2007**, *61*, 1056–1059.

[13] Karaballi, R. A.; Humagain, G.; Fleischman, B. R. A.; Dasog, M. Synthesis of Plasmonic Group-4 Nitride Nanocrystals by Solid-State Metathesis. *Angewandte Chemie International Edition* **2019**, *58*, 3147–3150.

[14] O'Neill, D. B.; Frehan, S. K.; Zhu, K.; Zoethout, E.; Mul, G.; Garnett, E. C.; Huijser, A.; Askes, S. H. C. Ultrafast Photoinduced Heat Generation by Plasmonic HfN Nanoparticles. *Advanced Optical Materials* **2021**, 2100510.

[15] Gupta, S. K.; Mao, Y. Recent Developments on Molten Salt Synthesis of Inorganic Nanomaterials: A Review. *Journal of Physical Chemistry C* **2021**, *125*, 6508–6533.

[16] Liu, X.; Fechler, N.; Antonietti, M. Salt melt synthesis of ceramics, semiconductors and carbon nanostructures. *Chemical Society Reviews* **2013**, *42*, 8237.

[17] Zhang, H.; Dasbiswas, K.; Ludwig, N. B.; Han, G.; Lee, B.; Vaikuntanathan, S.; Talapin, D. V. Stable colloids in molten inorganic salts. *Nature* **2017**, *542*, 328–331.

[18] Kamysbayev, V.; Srivastava, V.; Ludwig, N. B.; Borkiewicz, O. J.; Zhang, H.; Ilavsky, J.; Lee, B.; Chapman, K. W.; Vaikuntanathan, S.; Talapin, D. V. Nanocrystals in Molten Salts and Ionic Liquids: Experimental Observation of Ionic Correlations Extending beyond the Debye Length. *American Chemical Society Nano* **2019**, *13*, 5760–5770.

[19] hui Zhu, L.; ran Tu, R.; wei Huang, Q. Molten salt synthesis of Al_2O_3 platelets using $NaAlO_2$ as raw material. *Ceramics International* **2012**, *38*, 901–908.

[20] Grabis, J.; Jankovica, D.; Sokolova, E.; Steins, I. Characteristics of zirconia nanoparticles prepared by molten salts and microwave synthesis. *IOP Conference Series: Materials Science and Engineering* **2013**, *49*, 012003.

[21] Ke, X.; Cao, J.; Zheng, M.; Chen, Y.; Liu, J.; Ji, G. Molten salt synthesis of single-crystal Co_3O_4 nanorods. *Materials Letters* **2007**, *61*, 3901–3903.

[22] Xue, P.; Wu, H.; Lu, Y.; Zhu, X. Recent progress in molten salt synthesis of low-dimensional perovskite oxide nanostructures, structural characterization, properties, and functional applications: A review. *Journal of Materials Science & Technology* **2018**, *34*, 914–930.

[23] Mao, Y.; Parsons, J.; McCloy, J. S. Magnetic properties of double perovskite La_2BMnO_6 (B = Ni or Co) nanoparticles. *Nanoscale* **2013**, *5*, 4720.

[24] Mao, Y.; Park, T.-J.; Wong, S. S. Synthesis of classes of ternary metal oxide nanostructures. *Chemical Communications* **2005**, 5721.

[25] Gouget, G.; Debecker, D. P.; Kim, A.; Olivieri, G.; Gallet, J.-J.; Bournel, F.; Thomas, C.; Ersen, O.; Moldovan, S.; Sanchez, C.; Carenco, S.; Portehault, D. In Situ Solid–Gas Reactivity of Nanoscaled Metal Borides from Molten Salt Synthesis. *Inorganic Chemistry* **2017**, *56*, 9225–9234.

[26] Guan, H.; Li, W.; Han, J.; Yi, W.; Bai, H.; Kong, Q.; Xi, G. General molten-salt route to three-dimensional porous transition metal nitrides as sensitive and stable Raman substrates. *Nature Communications* **2021**, *12*, 1376–1387.

[27] Li, X.; Westwood, A.; Brown, A.; Brydson, R.; Rand, B. A convenient, general synthesis of carbide nanofibres via templated reactions on carbon nanotubes in molten salt media. *Carbon* **2009**, *47*, 201–208.

[28] Srivastava, V.; Kamysbayev, V.; Hong, L.; Dunietz, E.; Klie, R. F.; Talapin, D. V. Colloidal Chemistry in Molten Salts: Synthesis of Luminescent $In_{1-x}Ga_xP$ and $In_{1-x}Ga_xAs$ Quantum Dots. *Journal of the American Chemical Society* **2018**, *140*, 12144–12151.

[29] Hudson, M. H.; Gupta, A.; Srivastava, V.; Janke, E. M.; Talapin, D. V. Synthesis of $In_{1-x}Ga_xP$ Quantum Dots in Lewis Basic Molten Salts: The Effects of Surface Chemistry, Reaction Conditions, and Molten Salt Composition. *Journal of Physical Chemistry C* **2022**, *126*, 1564–1580.

[30] Kan, X.; Ding, J.; Zhu, H.; Deng, C.; Yu, C. Low temperature synthesis of nanoscale titanium nitride via molten-salt-mediated magnesiothermic reduction. *Powder Technology* **2017**, *315*, 81–86.

[31] Christensen, A. N.; Hämäläinen, R.; Turpeinen, U.; Andresen, A. F.; Smidsrød, O.; Pontchour, C.-O.; Phavanantha, P.; Pramatus, S.; Cyvin, B. N.; Cyvin, S. J. The Temperature Factor Parameters of Some Transition Metal Carbides and Nitrides by Single Crystal X-Ray and Neutron Diffraction. *Acta Chemica Scandinavica* **1978**, *32a*, 89–90.

5 Silanes

5.1 Introduction

Silanes are highly versatile materials that possess various functional groups in their molecular structure.[1;2] These silanes can be incorporated onto a surface either through post-synthesis grafting or during the synthesis process using suitable precursors.[3] The process of silanization relies on the presence of hydroxyl (-OH) groups on the surface of the target material, which facilitates the formation of a strong Si-O bond.[4;5] Silanes are particularly well-suited as ligands for materials that are not sensitive to water or acids since these byproducts are generated during the condensation reaction of silanes at the surface.[6] In some cases, a catalyst is necessary to promote the binding of the silane to the surface.[7;8]

When selecting silanes for surface modification, the choice of polar or apolar tails depends on the targeted medium. Polar tails often exhibit pH and concentration dependence in water, which contributes to the stability of the particles. Previous studies, conducted in 1997 using x-ray photoelectron spectroscopy (XPS) analysis and ^{29}Si Magic Angle Spinning Nuclear Magnetic Resonance (MAS-NMR), reported that silanes are grafted onto the surface of ZrO_2 particles through a Zr-O-Si bond, with interlinked silane molecules forming Si-O-Si bonds.[6;9;10] Consequently, the presence of multidentate silanes often results in a multilayer coverage on the surface.

In the case of post-synthesis ligand exchange from oleate or trioctylphosphine oxide (TOPO) to silanes, this method has been previously applied to materials such as ferrite or TiO_2 particles. In these instances, the removal of native oleate and the presence of silanes have been investigated using fourier-transform infrared spectroscopy (FT-IR). However, a comprehensive mechanistic investigation of this ligand exchange process has not been conducted thus far.[11–15]

Electronic reference to access in vivo concentrations

ERETIC (Electronic Reference for Accessing In Vivo Concentrations) is a method used to quantify and determine absolute concentrations without the need for an internal reference. In this method, the acquisition signal of the sample is compared with references of known concentration measured under the same tuning, matching and shimming of the probe, calibrated 90-degree pulse, and appropriate recovery delay conditions ($\geq$ 5 times T_1). Throughout this chapter, ERETIC measurements allowed us to accurately determine the concentration of bound oleic acid (OA) on the surface of our initial particles for quantitative ligand exchanges and NMR titration experiments.

5.2 Mechanistic investigation of ligand exchange with silane

In this study, we focused on ZrO_2 and HfO_2 particles that were initially capped with OA. The synthesis of these particles followed a standard procedure outlined in the literature.[16;17] The average particle size for the as synthesized ZrO_2 and HfO_2 nanocrystals (NCs) were 3–4 nm in size. Throughout the study, we employed a tridentate silane molecule called hexadecyltrimethoxysilane (HMS). Figure 5.1 provides visual representations of metal oxide NCs with capping by both OA and HMS. In this figure, various potential binding configurations for the HMS molecule are illustrated. Specifically, we emphasize different types of condensation reactions that may take place between the surface Si-MeO and -OH groups, forming covalent Si-OH bonds. It is notable that this

phenomenon extends beyond the surface -OH groups, surrounding neighboring silanol groups that have the tendency to form Si-O-Si covalent bonds, either fully covering the surface or polymerizing vertically to it. As a result, this process engenders a network of cross-linked silanes, characterized by numerous covalent bonds.[2]

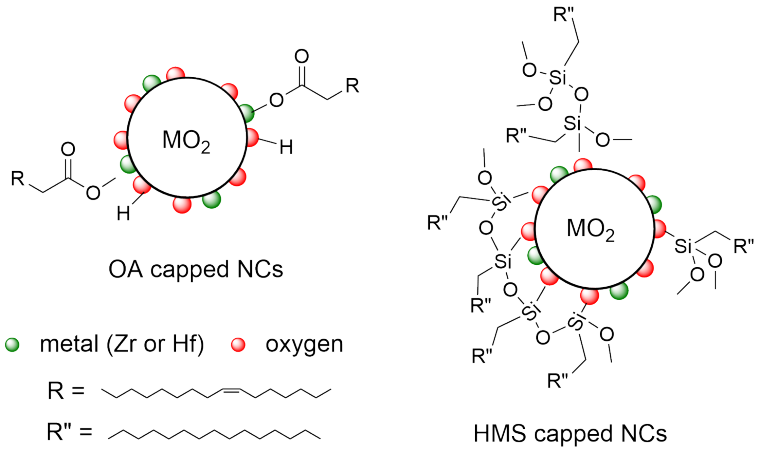

Figure 5.1 Visualization of metal oxide particles capped with OA and HMS. The metal atoms on the surface are shown in green, while the oxygen atoms are shown in red. Various binding scenarios for silane molecules are also represented.

The bonding state of our ligands was monitored using several characteristic resonances in ^{1}H NMR. Specifically, the alkene resonances (around 5 ppm, resonance 5) corresponded to the native oleate ligand, while the H_2C-Si resonance (around 0.8 ppm, resonance b) and the methoxy resonance (around 3.5 ppm, resonance a) originated from the silane moiety. These NMR signals were utilized to track the bonding status and transformations of our ligands during the experimental procedures (Figure 5.2).

5.2.1 Choice of catalyst

In the literature, different catalysts such as acetic acid, NaOH, and tetramethylammonium hydroxide (TMAH) have been used for replacing the native oleate from the NCs surface with HMS. In this work, the relative efficiency of these catalysts has been studied under similar concentrations (1 equivalent of catalyst and HMS versus bound OA) and heating conditions (80°C for 15 min). In the NMR analysis shown in Figure 5.3, the

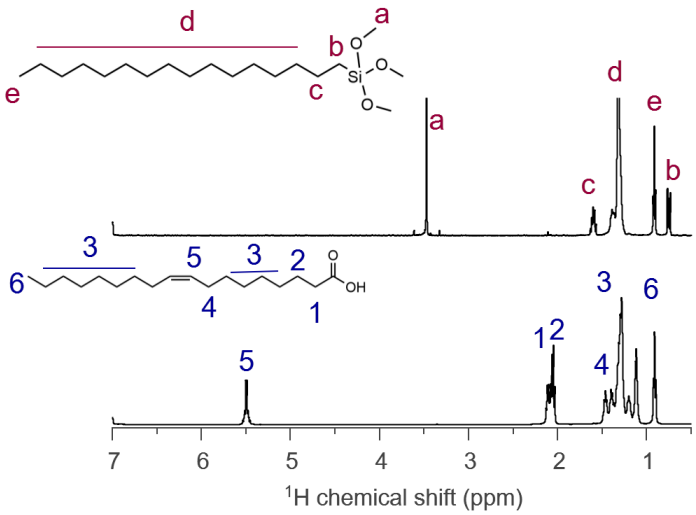

Figure 5.2 | ^{1}H NMR of OA and HMS shown as references in benzene-d_6.

resonances linked to the alkene of OA at 5.7 ppm, the methoxysilane of HMS at 3.45 ppm, and methanol formation at 3.25 ppm are examined. This analysis focuses on the condensation of silane at the surface, leading to the formation of an O-Si bond, and the concomitant release of methanol as a byproduct. The addition of only HMS to the ZrO_2 OA-capped particles does not result in HMS binding, releasing only a minimal amount of OA. It is therefore evident that a catalyst is essential for this exchange to occur. When acetic acid is introduced along with HMS, a distinct resonance attributed to free OA is detected. However, not all the OA is released, as a clear, broad resonance persists. A methanol resonance emerges, indicating the activation of methoxysilane toward surface binding. In the presence of NaOH, similar resonances of bound and free OA, as well as methanol, are observed. However, with NaOH, there is less free OA but a higher formation of methanol. When using TMAH, a clear resonance of free OA is detected along with methanol, with very little bound OA remaining. In all these cases, where 1 equivalent of catalyst and 1 equivalent of HMS are added compared to the bound OA, it is reasonable to assume that Si-O-Me is still present, given that each HMS molecule has three methoxysilane per molecule. Among the catalysts tested, TMAH has shown the highest efficiency in removing the native oleate ligand. NaOH, on the other hand, is more

effective at releasing methanol from the methoxy group, indicating efficient condensation of HMS, but it is less efficient at stripping the oleate from the surface. For a successful ligand exchange, it is crucial to have a catalyst that not only promotes the condensation of the silane at the surface but also efficiently removes the native ligand. If only one of these phenomena occurs, it could result in either the precipitation of naked particles or the formation of detached silane polymers. Based on the investigation, TMAH has been chosen as the catalyst for this study due to its ability to effectively strip the native oleate ligand without causing particle precipitation.

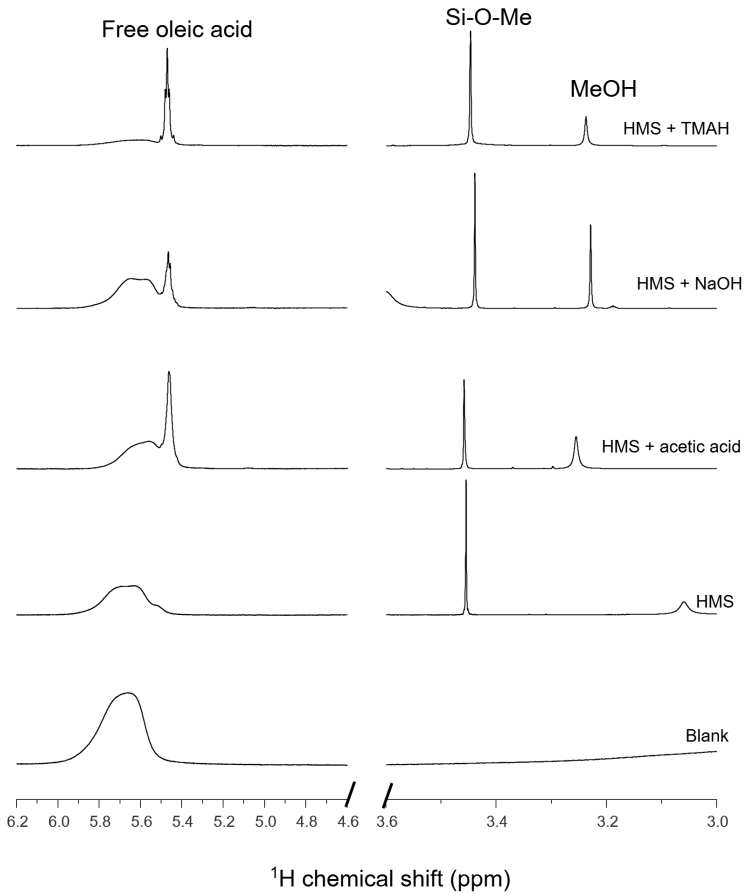

Figure 5.3 | ^{1}H NMR of ZrO_2 OA capped particles titrated with HMS, HMS + acetic acid, HMS + NaOH and HMS + TMAH heated at 80 °C for 15 minutes in benzene-d_6.

5.2.2 NMR titration with silane

To achieve a complete ligand exchange and remove the native ligand in favor of silane, a series of steps involving ligand addition and purification are essentially aimed at eliminating any remaining unreacted or residual components. In Figure 5.4, we observe a successful ligand exchange from OA-capped ZrO_2 particles to HMS-capped particles. To achieve this comprehensive exchange, the OA-capped particles were heated to 80 °C along with two equivalents of HMS and two equivalents of TMAH catalyst for 20 minutes. These equivalents were calculated based on the surface concentration of OA determined via ERETIC analysis. Subsequently, the particles were precipitated using acetone and centrifugation, followed by redispersion in deuterated benzene (benzene-d_6).

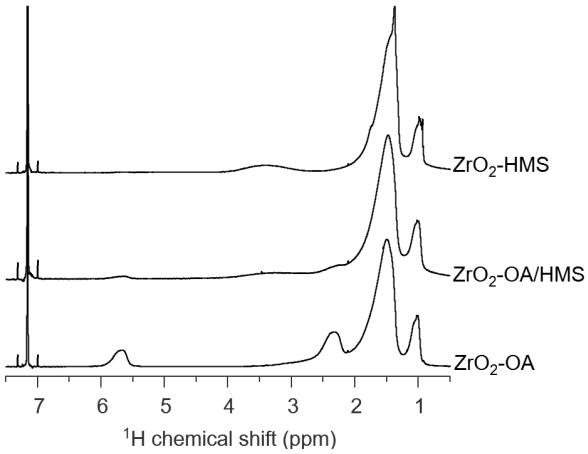

Figure 5.4 The ^{1}H NMR spectra of the ZrO_2 particles were recorded at each stage of the ligand exchange with HMS. Specifically, ZrO_2-OA corresponds to the initial NCs capped with OA, ZrO_2-HMS represents the NCs obtained after two rounds of HMS addition and purification, and ZrO_2-OA-HMS denotes the intermediate stage where the particles were capped with both ligands following only one HMS treatment. All spectra were recorded in benzene-d_6.

An intermediate stage was observed via NMR, wherein the particles were capped with both OA and HMS. To rectify this, 0.5 equivalent of HMS and 0.5 equivalent of TMAH catalyst were added to the particles and heated at 80 °C for 20 min. The parti-

cles were again precipitated through centrifugation using acetone and then redispersed in benzene-d_6. Subsequently, the NMR analysis confirmed that the particles were now exclusively capped with HMS, as evidenced by the distinct resonances of HMS. Nevertheless, further purification through precipitation and redispersion is necessary to eliminate the remaining free HMS observed as sharp resonances.Very similar data were obtained for HfO_2 NCs (FigureA.22).

Dynamic light scattering (DLS) analysis revealed an increase in the hydrodynamic size of the particles during the transition from OA to HMS as the capping ligand. This change may be attributed to the formation of multilayers or polymerization of HMS at the surface of the ZrO_2 particles (Figure 5.5) .

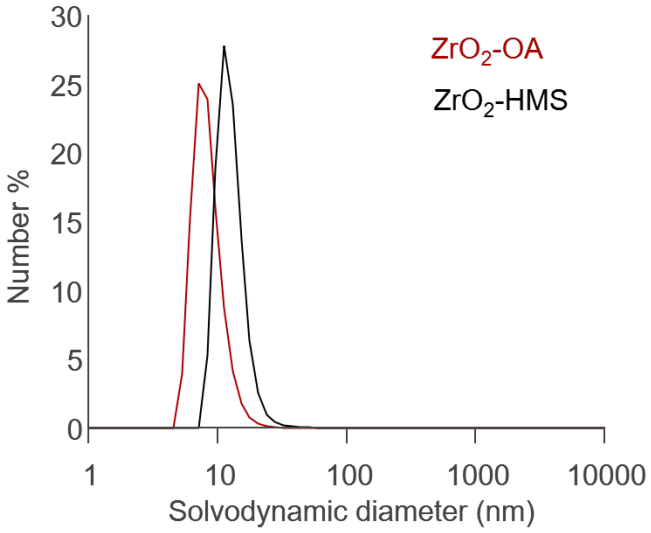

Figure 5.5 DLS analysis of the particles, which were capped with OA or HMS. This size augmentation observed after the HMS treatment could potentially result from the polymerization or the formation of multilayers of HMS around the particles.

5.2.3 What is at the surface?

Diffusion ordered spectroscopy (DOSY) analysis was conducted on HfO_2-HMS capped NCs following the exchange from OA. The results revealed the presence of two distinct

diffusion processes, both slower than free HMS diffusion, see Figures A.25 and 5.6. Our working hypothesis suggests that the slower-diffusing species corresponds to bound silane, while the faster-diffusing one represents polymerized silane. Based on the diffusion coefficients, we estimate sizes of 13.3 nm and 2.4 nm. The 13.3 nm size is likely attributed to silane binding to the NCs, aligning with our DLS data (Figure 5.6). Currently, it is challenging to determine whether single HMS molecules are bound to the NCs' surfaces or if polymerization has occurred.

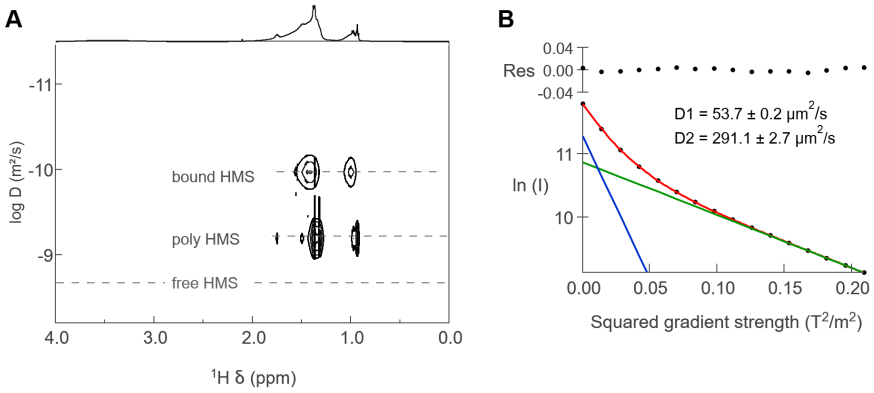

Figure 5.6 (A) DOSY NMR analysis of HfO_2 HMS capped particles achieved through ligand exchange from oleate, revealing two distinct diffusion processes in the sample. The slower diffusion is attributed to bound silane, while the faster diffusion is associated with polymerized silane. The diffusion of free silane is separately measured and provided for comparative purposes. The solvent used is benzene-d_6. (B) Decay curve fitting of the DOSY NMR data, yielding size estimates of 13.3 nm (D1) and 2.4 nm (D2) for the particles.

Furthermore, a broad resonance appearing between 3–3.5 ppm is identified in our 1D NMR. The broad resonance can be attributed to exchangeable protons, most likely associated with hydroxyl (OH) groups present on the surface. The interaction with the surface of the NCs is supported by the negative cross-peak signal observed in NOESY (Figure A.24). This resonance shift, as shown in Figure 5.7, when water is added, strongly suggests the presence of exchangeable protons, most probably OH groups located at the surface. Importantly, in the HSQC spectrum shown in Figure A.23, this

particular resonance does not show any correlation with any other carbon. This finding reinforces that hydroxyl groups are attached to the surface alongside the silanes.

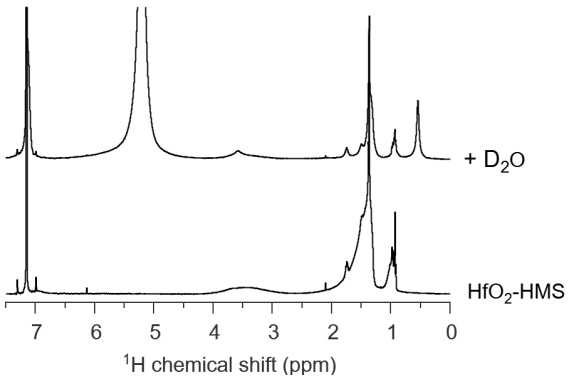

Figure 5.7 | ^{1}H NMR of HfO_2 HMS capped particles before and after water addition in benzene-d_6. The broad resonance at 3 ppm becomes sharp and shifts to higher ppm.

To prevent HMS polymerization at the surface, we employed mono-methoxy silane ligands to replace OA. These ligands underwent a similar treatment as HMS, involving stepwise addition with TMAH at 80 °C for 20 minutes. After each purification step, it became evident by looking at the supernatant by NMR that we were removing OA, leading to the destabilization of our ZrO_2 particles. However, it became apparent that the mono-methoxy silane ligand was only partially binding to the surface, and this limited binding was insufficient to confer colloidal stability to our particles. Figure 5.8 displays distinct ^{1}H-NMR spectra, illustrating different stages of the process. The blank spectrum represents the initial NCs, while the blue spectrum corresponds to purified NCs following one round of treatment with 1 equivalent of hexadecyilmono-methoxy silane (MS) and 1 equivalent of TMAH at 80 °C for 20 minutes. Additionally, the red spectrum represents purified NCs after a subsequent round of treatment with 1 equivalent of MS and 1 equivalent of TMAH, totaling 2 equivalents added, still at 80 °C for 20 minutes. Notably, new broad resonances emerge around 3.4 ppm. However, it is evident that the overall intensity is decreasing, indicating a reduction in concentration. Furthermore, a visible NCs precipitation is observed at the bottom of the NMR tube. Similar results

were obtained when starting from smaller HfO_2 NCs.

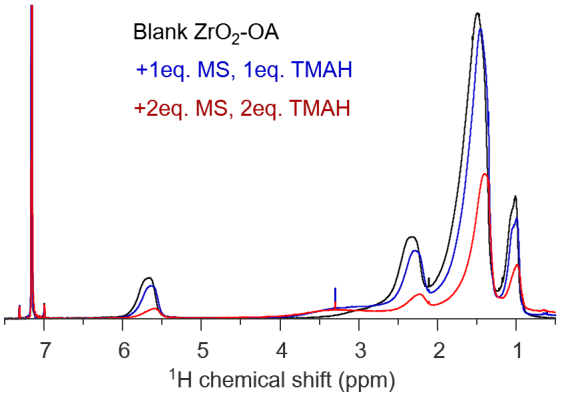

Figure 5.8 The ^1H-NMR spectra depict different stages of the process involving ZrO_2 particles capped with OA. The black curve represents the initial state of OA-capped particles, while the blue curve represents purified NCs after a single treatment with 1 equivalent of MS and 1 equivalent of TMAH at 80 °C for 20 minutes. The red curve corresponds to purified NCs after subsequent treatment with 1 equivalent of MS and 1 equivalent of TMAH under the same conditions, totaling two treatments with MS. Notably, broad resonances appearing around 3.4 ppm can be attributed to bound MS. Despite the treatments, it is evident that OA remains present at the particle surface, even after the two MS treatments. Moreover, a decrease in overall intensity indicates a reduction in the concentration of NCs in the NMR tube, which is further confirmed by the visual formation of precipitates.

5.2.4 What is being released?

Upon examination of the supernatant mixture, the presence of free oleate and HMS can be observed. Additionally, four resonances at 2.8 ppm, 2.6 ppm, 2.1 ppm, and 1.95 ppm are observed and remain unidentified (see Figure 5.9). By comparing these resonances with a reference sample of OA with TMAH, it is possible to assign the 2.1 ppm resonance to the CH_2 group next to the double bond of OA. The 1.8 ppm resonance is attributed to the H_3C-N methyl ammonium in tetramethylammonium. The remaining resonances at 2.6 ppm and 1.95 ppm exhibit the same integral and multiplicity as the α and β CH_2

resonances adjacent to the carboxylate group, respectively. However, these resonances appear to be unshielded. Interestingly, when the supernatant solution is spiked with OA/TMAH reference, the resonances at 2.6 ppm and 1.95 ppm become more shielded and shift to lower ppm values. Based on these observations, our hypothesis is that during the ligand exchange process, the native oleate leaves the surface as tetramethylammonium oleate. The difference in shielding observed for the resonances closer to the carboxylate in the supernatant compared to a 1:1 mixture of OA/TMAH reference could be attributed to the fact that in the supernatant solution the oleate is surrounded by more than one tetramethylammonium molecule, leading to altered chemical environments around these resonances, see Figure 5.9.

These findings provide insight into the transformation of the native ligand during the ligand exchange process and suggest the formation of tetramethylammonium oleate as a byproduct. This is further supported by the observed chemical shifts and changes in shielding upon the addition of the OA/TMAH reference to the supernatant solution.

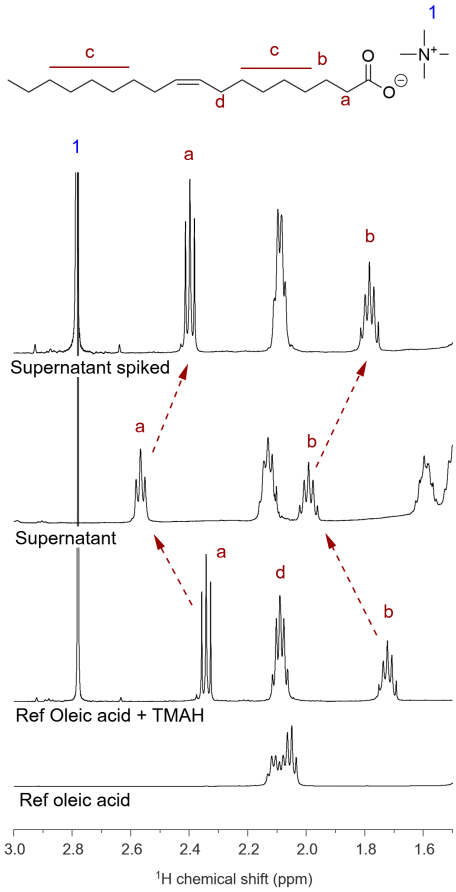

Figure 5.9 | ^{1}H NMR spectra were recorded for the following samples in benzene-d_6: OA as a reference; reference of a 1:1 mixture of OA and TMAH;the supernatant; the supernatant spiked with a 1:1 mixture of OA and TMAH.

5.3 Conclusion

Using silane as a capping ligand presents challenges due to the unknown exchange and binding mechanisms. Moreover, managing its surface polymerization also proves to be challenging. Our attempts to use monosubstituted silane to prevent polymerization were unsuccessful; we were unable to obtain silane-capped particles. Instead, we only managed to remove OA from the surface, destabilizing the NCs. However, utilizing trimethoxy silane successfully replaced OA, preventing precipitation. Yet, based on DLS and DOSY

analysis, the hydrodynamic diameter of our particles tended to increase, suggesting a polymeric ligand coverage. In our work, we could not characterize the number of silane layers formed.

It is worth noting that silane ligand exchange requires a catalyst and heat, unlike most ligand exchanges that occur at room temperature (e.g., with phosphonic acids, thiols, and amines). We discovered that TMAH serves as an effective catalyst, surpassing the performance of NaOH or acetic acid. The catalyst serves as an activator for silane binding, particularly methanol formation (in the case of methoxy silane) by providing OH, and aids in OA removal from the surface. We observed OA leaving the surface as a tetramethylammonium oleate salt.

For future research, a more promising approach could involve using silane bound to silica, which provides better control over silane binding and prevents polymerization. This strategy has been reported for effective capping and size tuning using core-shell silica hybrid spheres (silica core capped with silane).[8]

References

[1] Neouze, M.-A.; Schubert, U. Surface Modification and Functionalization of Metal and Metal Oxide Nanoparticles by Organic Ligands. *Monatshefte für Chemie - Chemical Monthly* **2008**, *139*, 183–195.

[2] Pujari, S. P.; Scheres, L.; Marcelis, A. T. M.; Zuilhof, H. Covalent Surface Modification of Oxide Surfaces. *Angewandte Chemie International Edition* **2014**, *53*, 6322–6356.

[3] Li, C.; Liu, X.; Shu, L.; Li, Y. AlN-based surface acoustic wave resonators for temperature sensing applications. *Materials Express* **2015**, *5*, 367–370.

[4] Fadeev, A. Y.; Kazakevich, Y. V. Covalently Attached Monolayers of Oligo(dimethylsiloxane)s on Silica: A Siloxane Chemistry Approach for Surface Modification. *Langmuir* **2002**, *18*, 2665–2672.

[5] Nishiyama, N.; Horie, K.; Asakura, T. Hydrolysis and condensation mechanisms of a silane coupling agent studied by ^{13}C and ^{29}Si NMR. *Journal of Applied Polymer Science* **1987**, *34*, 1619–1630.

[6] Turner, M. R.; Duguet, E.; Labrugre, C. Characterization of silane-modified ZrO_2 powder surfaces. *Surface and Interface Analysis* **1997**, *25*, 917–923.

[7] Rana, S.; Mallick, S.; Parida, K. M. Facile Method for Synthesis of Polyamine-Functionalized Mesoporous Zirconia and Its Catalytic Evaluation toward Henry Reaction. *Industrial & Engineering Chemistry Research* **2011**, *50*, 2055–2064.

[8] Lin, J.; Chen, H.; Ji, Y.; Zhang, Y. Functionally modified monodisperse core–shell silica nanoparticles: Silane coupling agent as capping and size tuning agent. *Colloids and Surfaces A: Physicochemical and Engineering Aspects* **2012**, *411*, 111–121.

[9] Luo, K.; Zhou, S.; Wu, L.; Gu, G. Dispersion and Functionalization of Nonaqueous Synthesized Zirconia Nanocrystals via Attachment of Silane Coupling Agents. *Langmuir* **2008**, *24*, 11497–11505.

[10] Isozaki, K.; Taguchi, T.; Ishibashi, K.; Shimoaka, T.; Kurashige, W.; Negishi, Y.; Hasegawa, T.; Nakamura, M.; Miki, K. Mechanistic Study of Silane Alcoholysis Reactions with Self-Assembled Monolayer-Functionalized Gold Nanoparticle Catalysts. *Catalysts* **2020**, *10*, 908.

[11] Owen, J. S.; Park, J.; Trudeau, P.-E.; Alivisatos, A. P. Reaction Chemistry and Ligand Exchange at Cadmium-Selenide Nanocrystal Surfaces. *Journal of the American Chemical Society* **2008**, *130*, 12279–12281.

[12] Palma, R. D.; Peeters, S.; Bael, M. J. V.; den Rul, H. V.; Bonroy, K.; Laureyn, W.; Mullens, J.; Borghs, G.; Maes, G. Silane Ligand Exchange to Make Hydrophobic Superparamagnetic Nanoparticles Water-Dispersible. *Chemistry of Materials* **2007**, *19*, 1821–1831.

[13] Watté, J.; Gompel, W. V.; Lommens, P.; Buysser, K. D.; Driessche, I. V. Titania Nanocrystal Surface Functionalization through Silane Chemistry for Low Temperature Deposition on Polymers. *ACS Applied Materials & Interfaces* **2016**, *8*, 29759–29769.

[14] Kunc, F.; Gallerneault, M.; Kodra, O.; Brinkmann, A.; Lopinski, G. P.; Johnston, L. J. Surface chemistry of metal oxide nanoparticles: NMR and TGA quantification. *Analytical and Bioanalytical Chemistry* **2022**, *414*, 4409–4425.

[15] Heinrich, C.; Niedner, L.; Oberhausen, B.; Kickelbick, G. Surface-Charged Zirconia Nanoparticles Prepared by Organophosphorus Surface Functionalization with Ammonium or Sulfonate Groups. *Langmuir* **2019**, *35*, 11369–11379.

[16] Garnweitner, G.; Goldenberg, L.; Sakhno, O.; Antonietti, M.; Niederberger, M.; Stumpe, J. Large-Scale Synthesis of Organophilic Zirconia Nanoparticles and their Application in Organic–Inorganic Nanocomposites for Efficient Volume Holography. *Small* **2007**, *3*, 1626–1632.

[17] Lauria, A.; Villa, I.; Fasoli, M.; Niederberger, M.; Vedda, A. Multifunctional Role of Rare Earth Doping in Optical Materials: Nonaqueous Sol–Gel Synthesis of Stabilized Cubic HfO_2 Luminescent Nanoparticles. *American Chemical Society Nano* **2013**, *7*, 7041–7052.

6 Conclusion

This thesis has strived to provide a comprehensive exploration of synthetic strategies, chemical complexities, and surface chemistry aspects associated with metal nitride NCs.

Chapter 2 explores the previously unexplored or debated territories of precursor conversion chemistry and surface chemistry in both Cu_3N and Cu_3PdN NCs. Our research successfully improved the synthesis of Cu_3N and Cu_3PdN NCs to produce phase pure and stable nanocubes by adjusting reaction conditions, especially during the purification process. Our experiments provided evidence supporting a precursor conversion pathway that relies on ammonia as the active nitrogen source. We proposed that the oxidation of oleylamine (OLAm) by both Cu(II) and nitrate leads to the formation of a primary aldimine. Subsequent nucleophilic addition and elimination reactions involving another OLAm molecule release ammonia, which then reacts with Cu(I) to create Cu_3N and Cu_3PdN. The nanocubes' surfaces are coated with a combination of OLAm and oleic acid (OA), with the latter forming in situ through further aldimine oxidation. Additionally, the introduction of palladium into Cu_3N leads to reductions in the optical band gap and the separation between the valence band maximum (VBM) and the Fermi energy (E_F).

Chapter 3 summarizes our efforts to produce various metal nitrides like TiN, Ni_3N, and Zn_3N_2 through solution-based methods by using a diverse variety of nitrogen sources. Our common approach was to first establish a bond between the metal and nitrogen and

then upon heating, crystallize into the desired NCs. Very early on, we noticed that even traces of oxygen could cause the formation of metal oxides. To address this, we conducted all the reaction preparation steps inside an inert atmosphere in a nitrogen glovebox, and the reactions themselves took place under argon at a Schlenk line. For TiN, we encountered a challenge during the crystallization step, as we consistently obtained amorphous products. While we could successfully create the intended Ti-N bond, crystallization did not occur under the temperatures and conditions we used. In contrast, when working with Zn_3N_2 and Ni_3N, our nitrogen sources turned out to be highly reactive and would completely reduce our metals, forming metallic NCs instead. Based on our results from solution-based methods, it became clear that the typical setup with three-neck flasks was not suitable for our materials. We needed to develop a new synthesis strategy that would enhance the crystallization process.

Chapter 4 explores a new approach called the molten salt assisted reaction, which has helped us achieve our goal of producing highly crystalline TiN NCs at a relatively low temperature of 350 °C. We conducted thorough investigations into various factors, including different combinations of molten salts, various sources of nitrogen, and the use of magnesium as a reducing agent, all of which contributed to the production of crystalline TiN. Among these, the combination of $ZnCl_2$-LiCl eutectic mixture and Ca_3N_2 turned out to be the best choice for both molten salt and nitrogen sources, resulting in crystalline products at lower temperatures. While using the molten salt-assisted synthesis, we observed some crystalline TiO_2 side phases, but these were much less prominent at lower temperatures. Analysis using XPS confirmed the presence of an oxide layer on the surface of our TiN particles. We believe that this layer provides stability to our particles in ambient air, allowing them to remain stable even when exposed to oxygen and water. These results, we consider, are laying the groundwork for further low-temperature synthesis of metal nitrides.

Chapter 5, the final chapter of this thesis, focuses on the surface chemistry of NCs using silane as ligands. This chapter summarizes preliminary data exploring how the ligand exchange happens, moving from an OA capped NC to silane. We demonstrate that

a catalyst is necessary for this exchange to occur, and among the catalysts we tested, tetramethylammonium hydroxide (TMAH) is the most effective in removing OA and binding the chosen silane, hexadecyltrimethoxysilane (HMS), to the surface. Furthermore, we discovered that the native ligand OA is released from the surface as a tetramethylammonium oleate salt. One challenge we encountered with silane is its tendency to form layers on the surface in an uncontrolled manner, as revealed by our DOSY results. These results indicate the presence of two distinct diffusing species: one attributed to bound silane, which diffuses slowly, and another associated with polymerized silane, which diffuses faster than the former but slower than free hexadecyltrimethoxysilane (HMS) molecules. These findings lay the groundwork for future investigations into the surface chemistry of silanes as ligands, as they are widely used in our community, yet much remains to be understood about their behavior.

Perspective

To advance our knowledge of metal nitrides, we must understand the mechanism of the colloidal syntheses that have so far resulted in crystalline products. While the process of precursor conversion has been explored in the cases of InN and now Cu_3N, there are many other systems in which this process remains a mystery. What is even more challenging is that the crystallization part of the process has not been investigated for any of the nitrides so far. Understanding this crystallization step is likely the most challenging aspect of the entire process, yet it remains the most critical for progress to be achieved in this field. After dedicating four years to this field, I have come to the conclusion that achieving metal nitrides, particularly TiN, through classical solvent-based chemistry is not the most promising approach. I firmly believe that our community should shift its focus toward molten salts as the solvent, as it has the potential to unlock the production of entirely new materials at significantly lower temperatures. The results presented in this study are preliminary, and there are still numerous other parameters to explore and generalize for the formation of various nitrides such as Ni_3N,

for instance. In our efforts to synthesize these materials, we encountered an issue where our Ni(II) would rapidly reduce to Ni(0). However, if we consider Ni_3N as an interstitial nitride, it necessitates the initial reduction of the metal followed by the intercalation of nitrogen. I believe that a molten salt setup would be an excellent synthesis method for the production of such materials. Nevertheless, it is essential to keep in mind that these materials also decompose at rather low temperatures, which means a different set of molten salts must be employed. Considering the widespread applications of early transition metal nitrides in fields like catalysis, photothermal therapy, superconductors, and electrochemical capacitors, synthetic efforts should focus on providing size tunability. Molten salts are recognized for their dual role as solvents and ligands, offering effective solvation for inorganic materials. By carefully selecting the appropriate concentration and type of molten salts, it may be feasible to fine-tune the size of the resulting NCs. Furthermore, with the use of molten salts enabling solid-state reactions at temperatures comparable to those employed in solution-based chemistry, it becomes conceivable to envision a novel setup akin to a conventional three-neck flask. In this setup, efficient stirring and uniform, continuous heating must be maintained over extended periods, accommodating prolonged reactions. The study of colloidal metal nitrides is a demanding and emerging area in science. However, introducing controllable synthesis of colloidal nitrides to the family of colloidal materials could create many exciting opportunities for the future of material science and nanotechnology.

A Supporting information

A.1 Supporting information for chapter 2

Table A.1 | Refined values after fitting the Cu_3N nanocrystals with the single-phase cubic ($Pm-3m$) model.

Parameter	$Cu_3N(Pm-3m)$
Scale	0.47
a(Å)	3.80
Uiso Cu (Å^2)	0.015
Uiso N (Å^2)	0.027
δ_2 (Å^2)	3.61
Psize (Å)	64.5

Table A.2 | Refined values after fitting the Cu_3PdN nanocrystals with single-phase Cu_3PdN ($Pm-3m$) model.

Parameter	$Cu_3PdN(Pm-3m)$
Scale	0.66
a(Å)	3.83
Uiso Cu (Å^2)	0.015
Uiso N (Å^2)	0.053
Uiso Pd (Å^2)	0.010
δ_2 (Å^2)	4.06
Psize (Å)	50.46

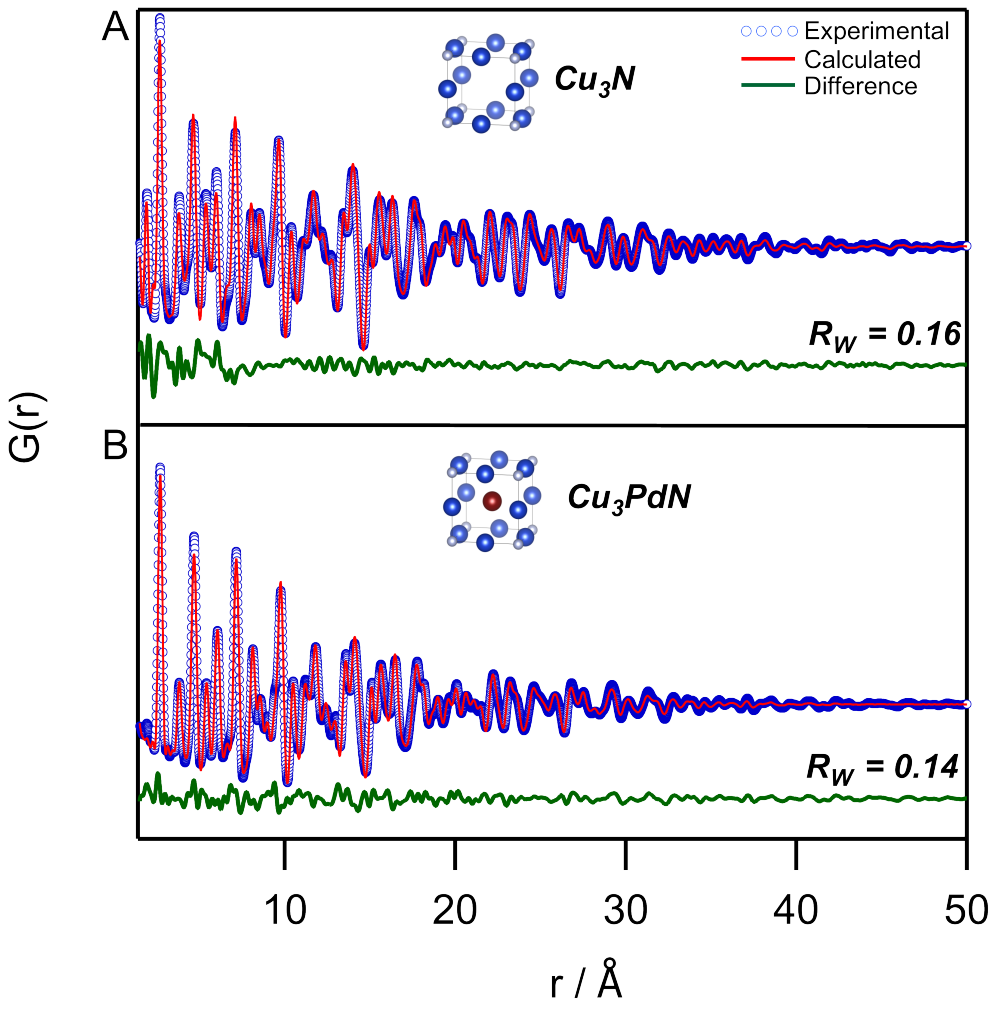

Figure A.1 PDF refinement for (A) Cu_3N nanocrystals with the cubic ($Pm-3m$) structure. The refined values are given in Table A.1. (B) Cu_3PdN nanocrystals with Cu_3PdN ($Pm-3m$). The refined values are given in Table A.2.

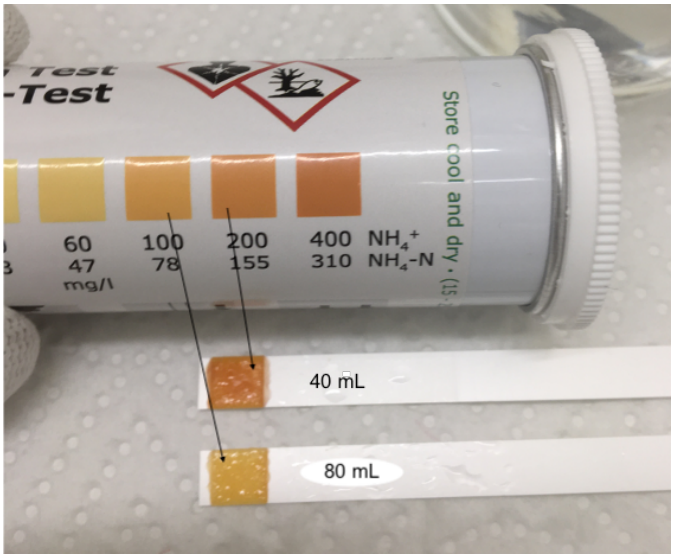

Figure A.2 The headspace of the reaction was bubbled into 5 mL of water and then diluted to 40 mL and 80 mL which would result in concentrations of 200 mg/L and 100 mg/L respectively. The color obtained via the test kit corresponds to the expected concentration.

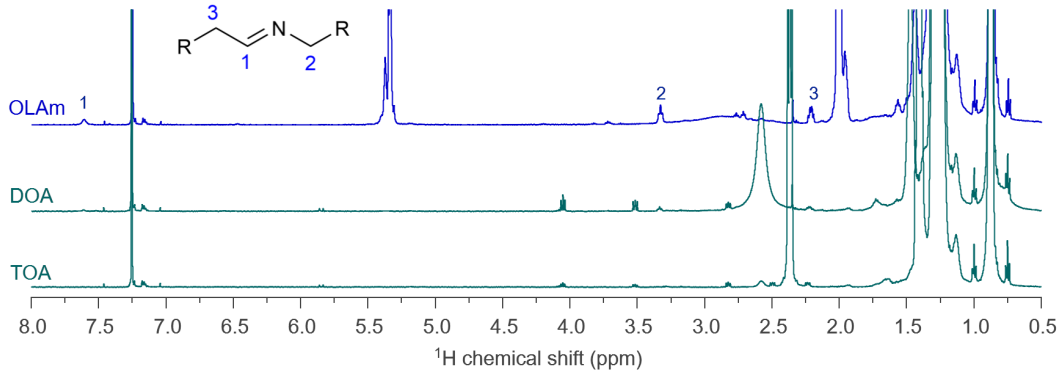

Figure A.3 ^{1}H NMR of the crude mixture obtained from the reaction with a primary, secondary, and tertiary amine. Aldimine is mainly detected during the reaction with a primary amine. A little amount of aldimine can be detected with dioctylamine which could be due to direct oxidation of dioctylamine.

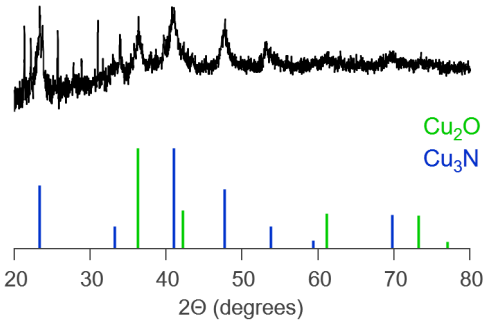

Figure A.4 | *p*XRD of the NCs obtained after ammonia bubbling into the reaction mixture with $Cu(NO_3)_2$ and dioctylamine. Both Cu_3N and Cu_2O are being formed.

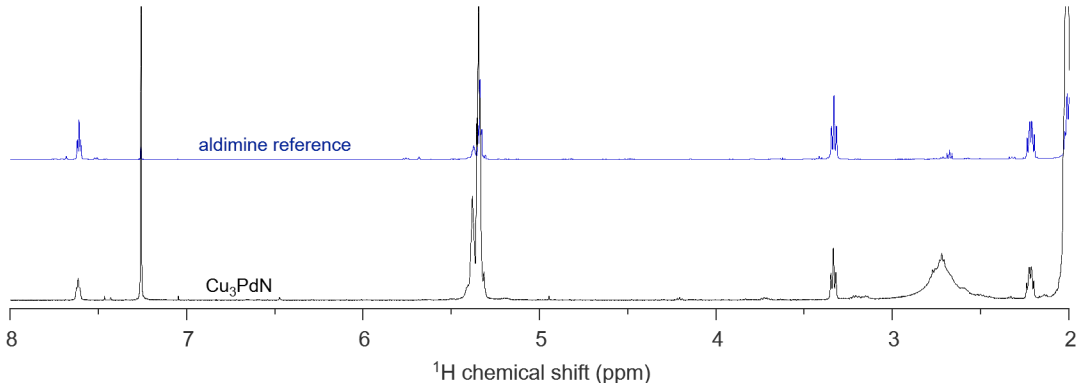

Figure A.5 | ^{1}H NMR of the crude mixture obtained from the Cu_3PdN reaction after 15 min at 240 °C. Aldimine is being formed in the reaction.

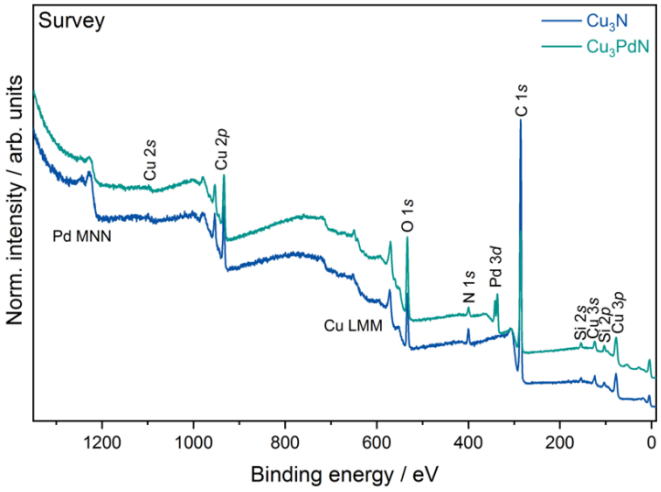

Figure A.6 | XPS spectra of the Cu_3N and Cu_3PdN samples. All major core and Auger lines are indicated.

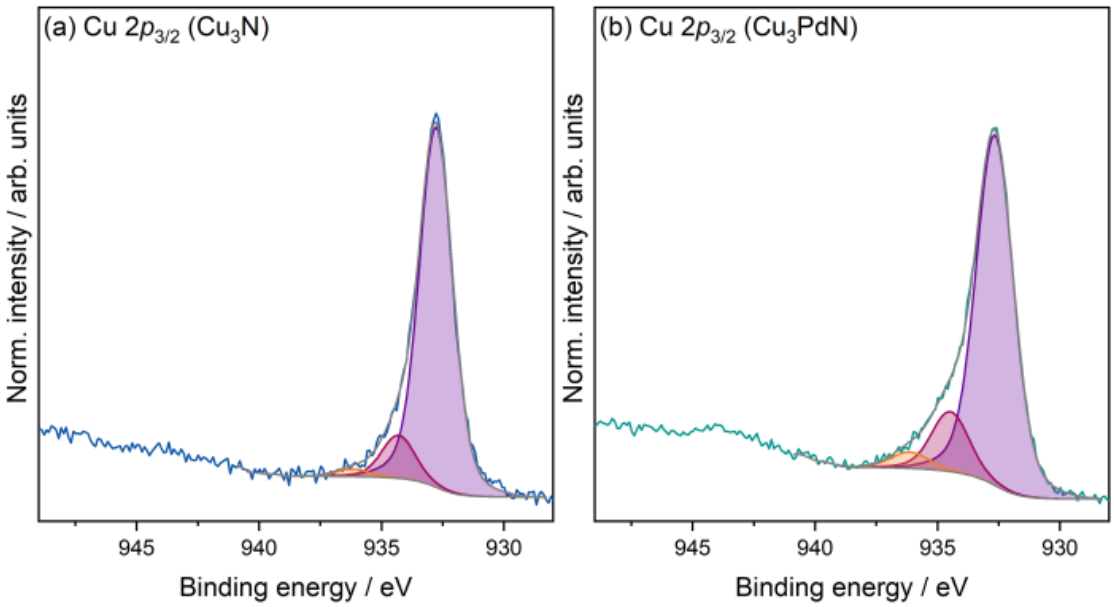

Figure A.7 | Cu $2p_{3/2}$ X-ray photoelectron core level spectra of (a) the Cu_3N and (b) the Cu_3PdN samples including peak fit analysis.

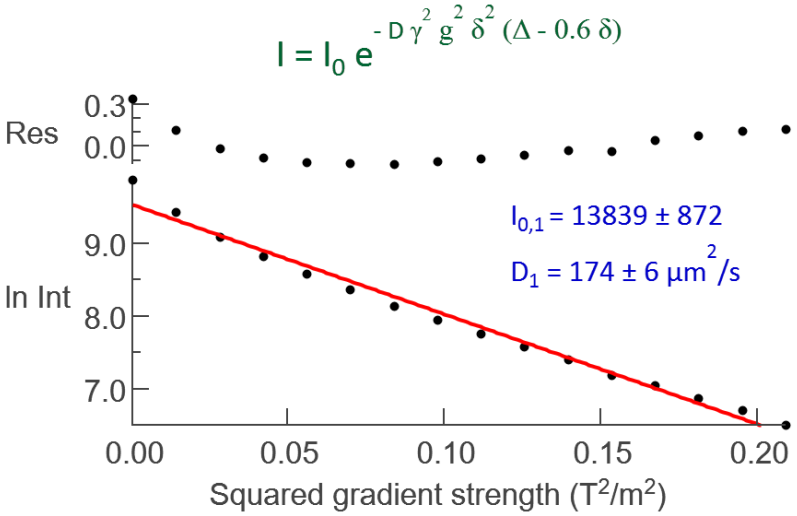

Figure A.8 Diffusion decay of the alkene region in the Cu_3N sample in Figure 2.17, fitted to the Stejskal-Tanner equation. The average diffusion coefficient corresponds to a solvodynamic size of 4.5 nm (calculated via the Stokes-Einstein equation), which is too small to represent a tightly bound ligand on a 13 nm nanocrystal.

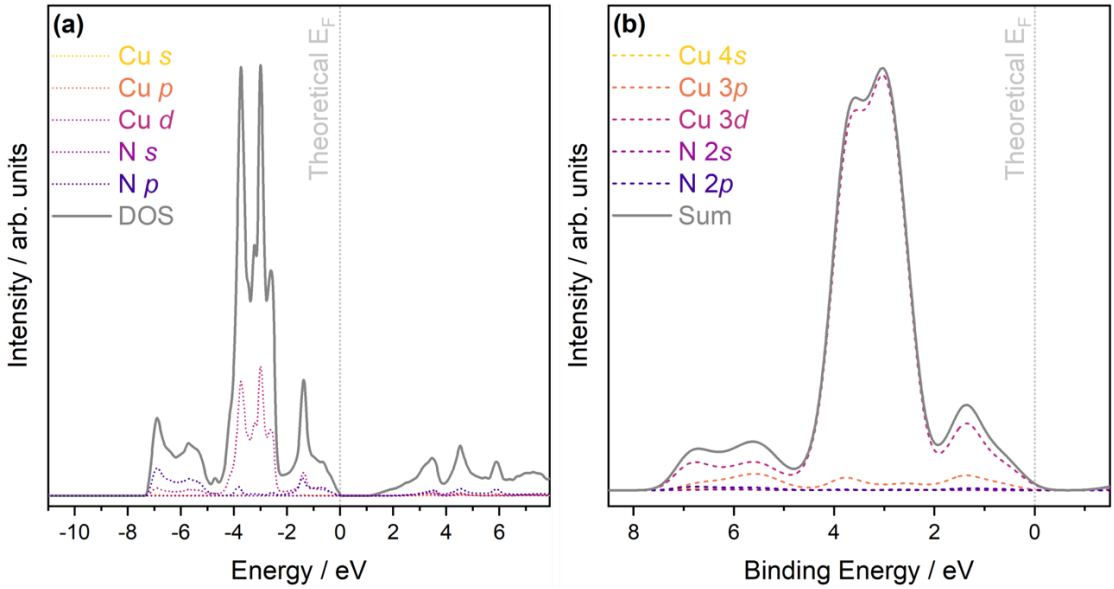

Figure A.9 Projected Density of States (PDOS) of Cu_3PdN from density functional theory calculations, including (a) unweighted PDOS with 50 meV Gaussian smearing showing both occupied and unoccupied states, and (b) weighted PDOS with 600 meV Gaussian smearing with the energy axis flipped and only showing the occupied states.

A.2 Supporting information for chapter 4

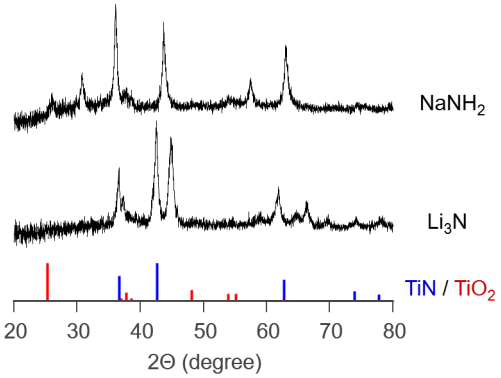

Figure A.10 | *p*XRD pattern of products obtained after reaction with $NaNH_2$ and Li_3N at 600 °C for 12h in molten salts. Both nitrogen sources did not yield phase pure TiN. References of TiN and TiO_2 are indicated in blue and red respectively.

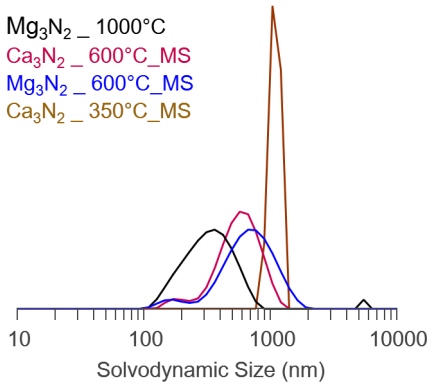

Figure A.11 | Solvodynamic diameters of TiN particles via different synthetic methods after 12h of reaction. All samples have a rather large size of above 100 nm.

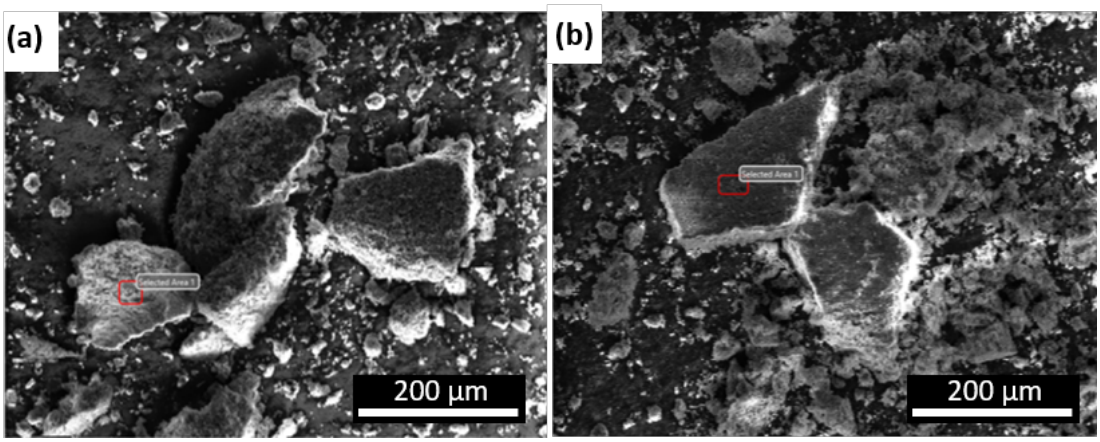

Figure A.12 | SEM images of TiN obtained from (a) Mg_3N_2 and (b) Ca_3N_2 at 600 °C for 12 h.

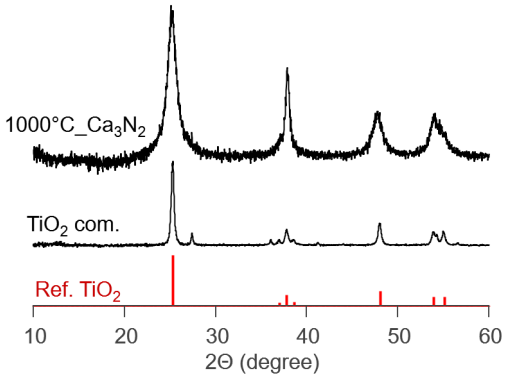

Figure A.13 | *p*XRD of TiO_2 commercially available vs TiO_2 after reaction at 1000 °C with Ca_3N_2 for 12 h. Reference of TiO_2 anatase is shown in red.

Table A.3 | Refined parameters obtained after Rietveld refinement.

	1000 °C	600 °C	350 °C
Bragg R-factor$_{TiN}$ /%	6.98	6.57	7.63
a$_{TiN}$ / Å	4.24	4.24	4.24
Occupancy Ti$_{TiN}$	0.70	0.74	0.78
Fraction$_{TiN}$/%	100	89.42	90.17
a$_{TiO_2-anatase}$ /Å	-	3.78	3.78
c$_{TiO_2-anatase}$	-	9.65	9.72
Fraction$_{TiO_2-anatase}$	0	10.58	9.83

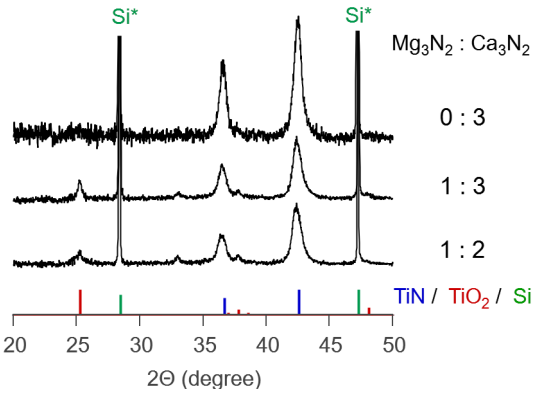

Figure A.14 *p*XRD patterns of the final product obtained by using a mixture of Ca_3N_2 and Mg_3N_2 as nitrogen sources. The synthesis was conducted in a eutectic mixture of $ZnCl_2$-LiCl as the molten salt, with magnesium as the reducing agent and TiO_2 as the titanium precursor in all synthesis reactions. The reaction time was maintained at 12 hours. References of TiN, TiO_2, and silicon are indicated in blue, red, and green respectively. The diffractions were normalized to silicon internal reference.

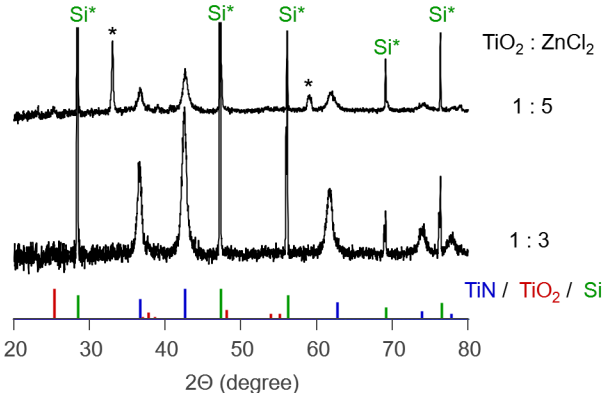

Figure A.15 *p*XRD patterns of the final product obtained upon reaction of 1 equivalent of TiO_2 with 3 or 5 equivalents of $ZnCl_2$ using Ca_3N_2 as the nitrogen source and magnesium as the reducing agent at 350 °C for 12h. References of TiN, TiO_2, and silicon are indicated in blue, red, and green respectively. The diffractions were normalized to silicon internal reference.

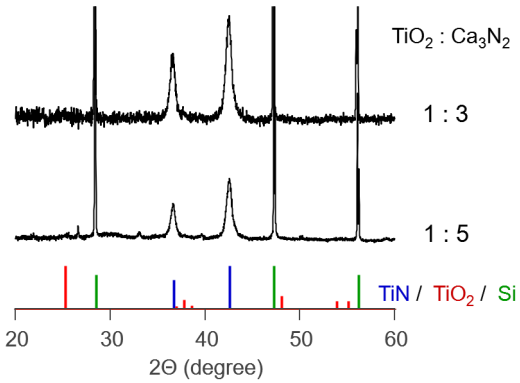

Figure A.16 | *p*XRD comparison of the product obtained from reactions using 5 eq. Ca_3N_2 in contrast to 3 eq. and 1 eq. TiO_2 at 350 °C for 12 h. References of TiN, TiO_2, and silicon are indicated in blue, red, and green respectively. The diffractions were normalized to silicon internal reference.

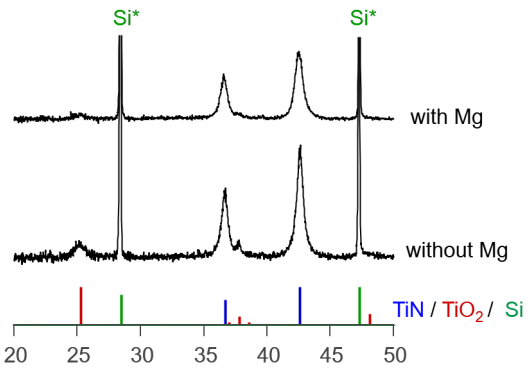

Figure A.17 | *p*XRD pattern of the product obtained with and without the use of magnesium as a reducing agent at 400 °C for 12h using Ca_3N_2 as the nitrogen source.References of TiN, TiO_2, and silicon are indicated in blue, red, and green respectively. The diffractions were normalized to silicon internal reference.

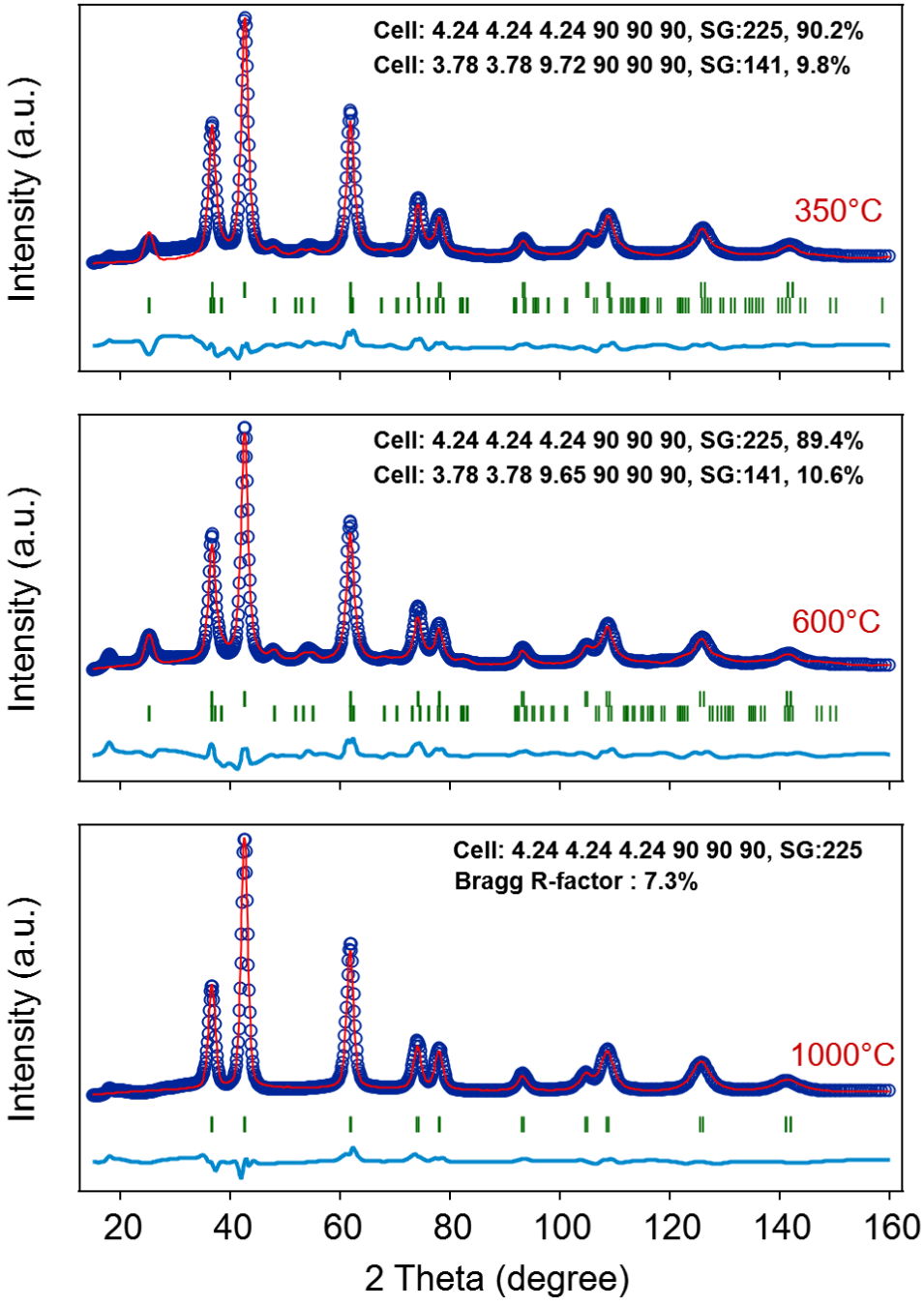

Figure A.18 Rietveld refinement results, including the fit, discrepancy, and pertinent Bragg peak details for the following samples after a 12 h reaction: (a) at 350 °C with molten salts, (b) at 600 °C with molten salts, and (c) at 1000 °C without molten salts. The refined attributes encompass the unit cell, space group, phase proportion, and Bragg R-factor.

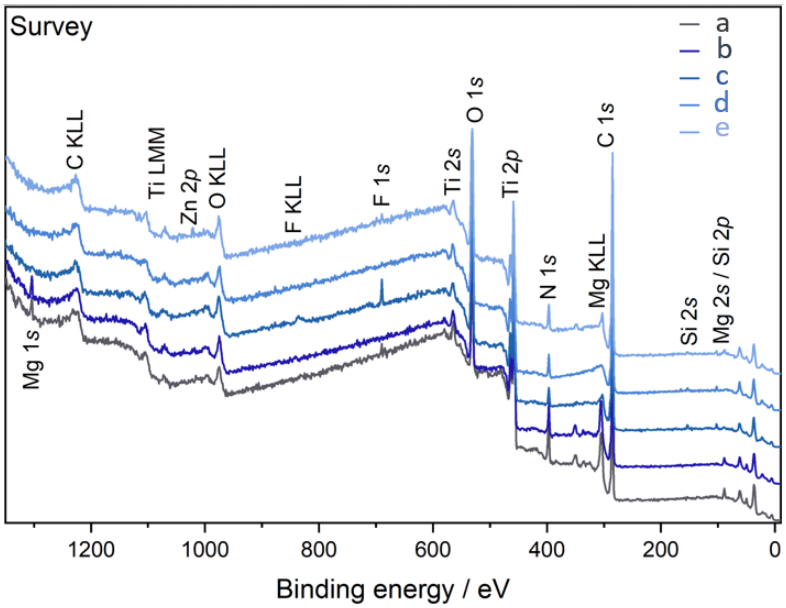

Figure A.19 XPS survey spectra of samples at different conditions: (a) 1000 °C , no molten salts, (b) 600 °C with molten salts using Mg_3N_2 and Mg, (c) 600 °C with molten salts using Ca_3N_2 and Mg, (d) 600 °C with molten salts using Ca_3N_2 without Mg, and (e) 350 °C with molten salts using Ca_3N_2 and Mg.

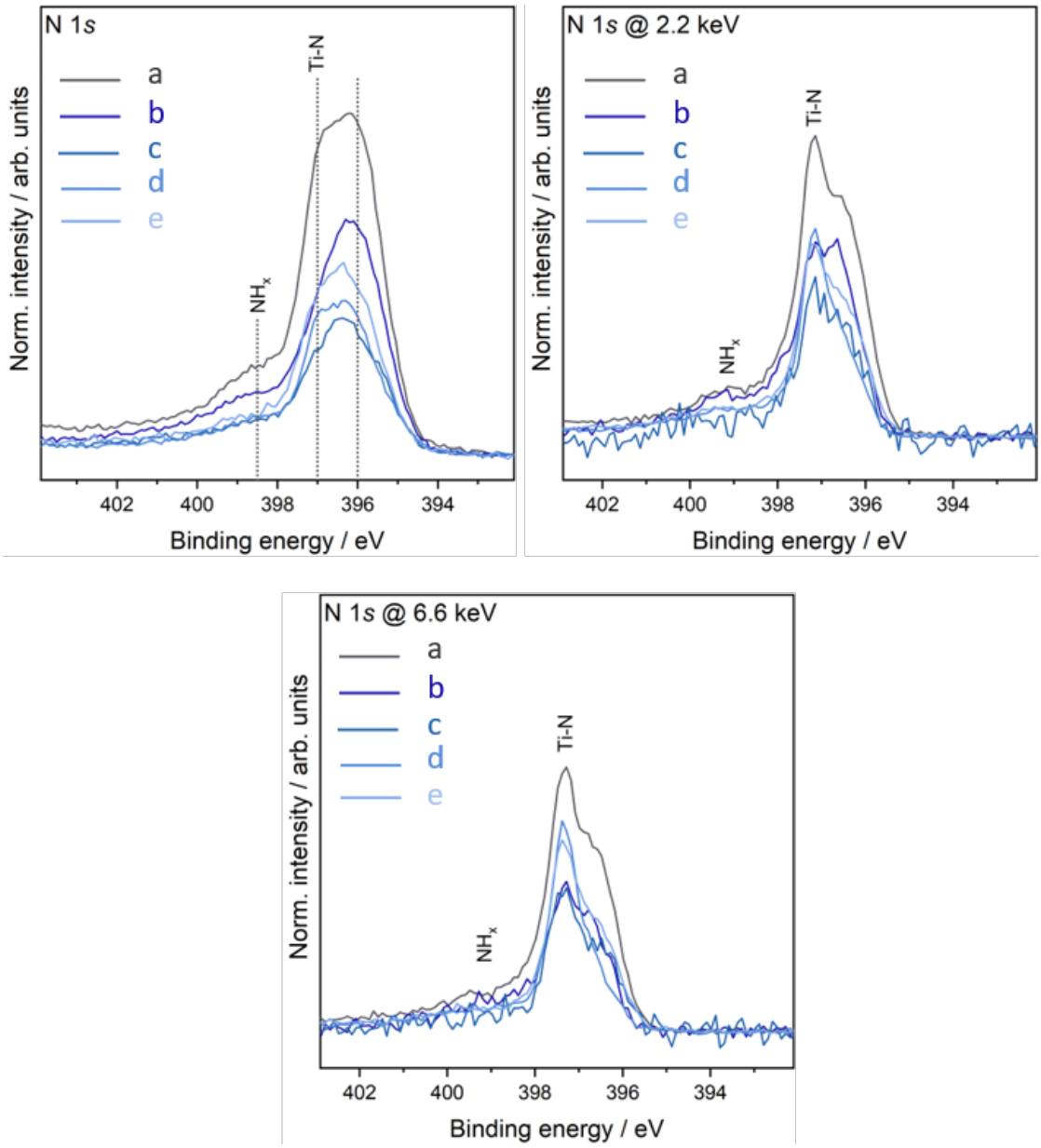

Figure A.20 XPS core level spectra of N_{1s} at various x-ray energy from different samples: (a) 1000 °C without molten salts, (b) 600 °C with molten salts, using Mg_3N_2 as the nitrogen source and Mg as the reducing agent, (c) 600 °C with molten salts, using Ca_3N_2 as the nitrogen source and Mg as the reducing agent, (d) 600 °C with molten salts, using Ca_3N_2 as the nitrogen source without Mg, and (e) 350 °C with molten salts, using Ca_3N_2 as the nitrogen source and Mg as the reducing agent.

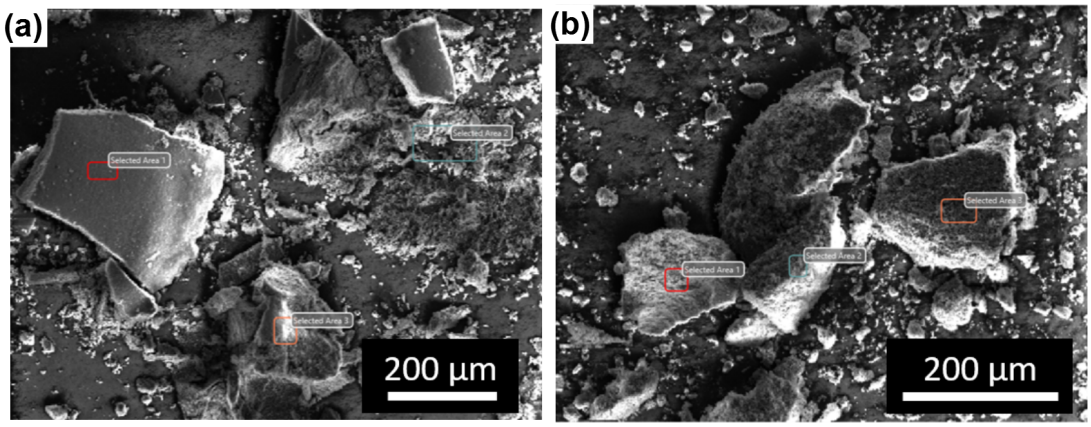

Figure A.21 SEM images of products obtained with a titanium molality of (a) 0.57 mol/Kg and (b) 2.3 mol/Kg. The particles obtained at 0.57 mol/Kg appear bigger in size.

A.3 Supporting information for chapter 5

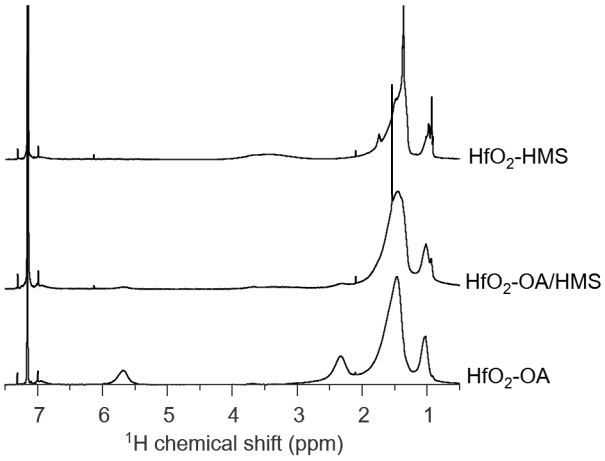

Figure A.22 ^{1}H NMR spectra of the HfO_2 particles were recorded at each stage of the ligand exchange with HMS. Specifically, HfO_2-OA corresponds to the initial nanoparticles capped with oleic acid, HfO_2-HMS represents the nanoparticles obtained after two rounds of HMS addition and purification, and HfO_2-OA-HMS denotes the intermediate stage where the particles were capped with both ligands following only one HMS treatment. Sharp resonances of HMS are discernible in the final graph, indicating the presence of free ligands. This suggests that additional purification steps are necessary to eliminate these unbound ligands.

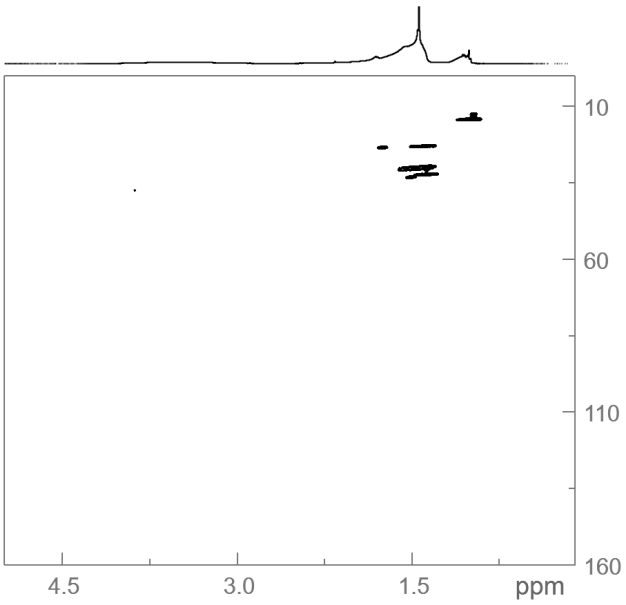

Figure A.23 HSQC spectrum of HfO_2 particles capped with HMS via ligand exchange from oleate. In this spectrum there is no observed correlation between the resonance at 3 ppm and any carbon signal. This observation further supports the notion that this particular resonance corresponds to an exchangeable proton resonance.

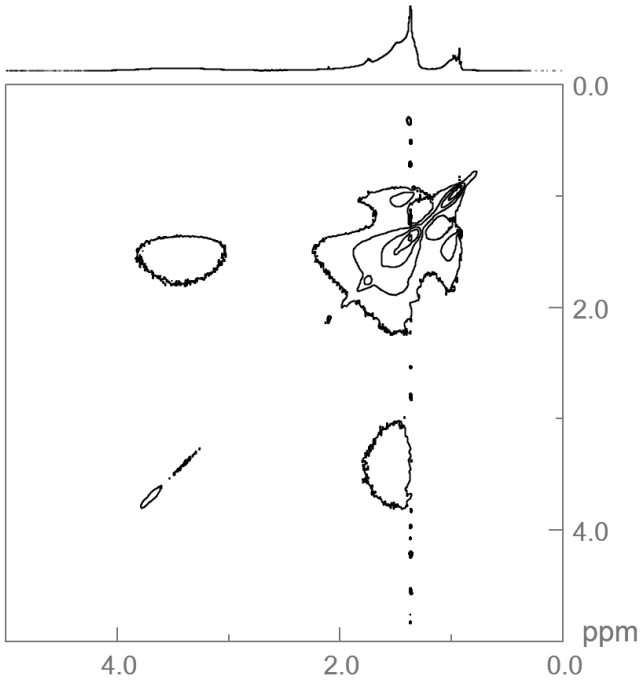

Figure A.24 | Noesy of HfO_2 HMS capped particles following ligand exchange from oleate reveals all resonances appearing as black signals (negative cross peaks), indicating their interaction with the surface.

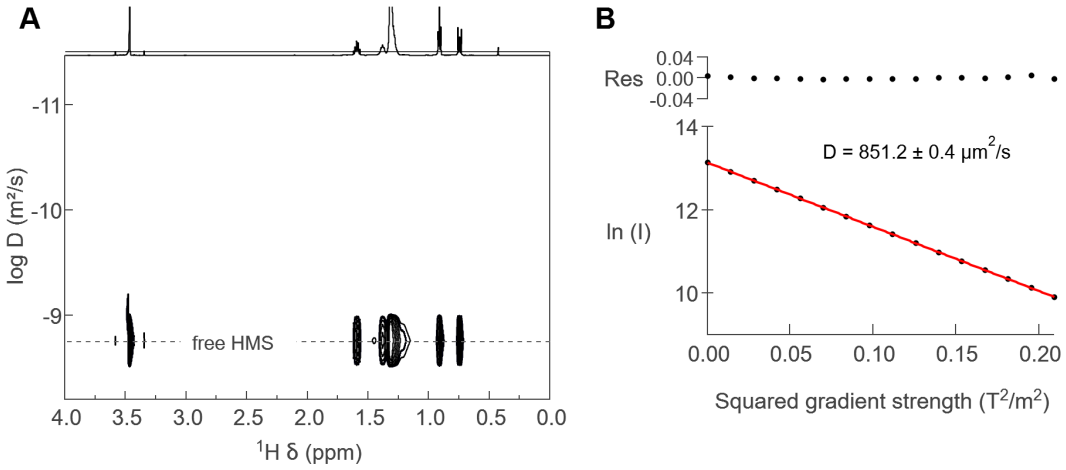

Figure A.25 | (A) DOSY NMR analysis of free HMS molecules in benzene-*d6*. (B) Decay curve fitting of the DOSY NMR data.

B
Scientific Output

Publications in Journals

ongoing **Parvizian, M.**; Pokratath, R.; Regoutz, A.; De Roo, J.; Efficient Synthesis of Group IV Metal Nitrides at Low Temperatures with Molten Salts;

2023 **Parvizian, M.**; Bechter, J.; Huber, J.; Chettata, N.; De Roo, J.; An Experimental Introduction to Colloidal Nanocrystals through InP and InP/ZnS Quantum Dots; *Journal of Chemical Education*, 100, 1613-1620

2022 **Parvizian, M.** ; Duran Balsa, A.; Pokratath, R.; Kalha, C.; Lee, S.; Van den Eynden, D.; Ibanez, M.; Regoutz, A. ; De Roo, J.; The Chemistry of Cu_3N and Cu_3PdN Nanocrystals; *Angew Chem Int Ed Engl*, 61, 1521-3773

2021 **Parvizian, M.** ; De Roo, J.; Precursor chemistry of metal nitride nanocrystals; *Nanoscale*, 13, 18865-18882

2021 Nemat, S.J., Van den Eynden D., Deblock L., Heilmann M., Köster J.M, **Parvizian, M.**, Tiefenbacher K., De Roo J.; Resorcin[4]arene-based multidentate phosphate ligands with superior binding affinity for nanocrystal surfaces; *Chemical Communications*, 57, 4694-4697

Conferences Contribution

Talk **Parvizian, M.** ; Duran Balsa, A.; Pokratath, R.; Kalha, C.; Lee, S.; Van den Eynden, D.; Ibanez, M.; Regoutz, A. ; De Roo, J.; The Chemistry of Cu_3N and Cu_3PdN Nanocrystals. Gordon Research Conference (GRC and GRS), Les Diablerets, Switzerland, July 2022

Poster **Parvizian, M.**; Duran Balsa, A.; Pokratath, R.; Kalha, C.; A. ; De Roo, J., Fall Meeting SCS, Zurich, September 2022

Poster **Parvizian, M.** ; Duran Balsa, A.; Pokratath, R.; Kalha, C.; A. ; De Roo, J., NanoGe, online, **Poster award** from ACS Energy & fuels, October 2021